

**Development of the Silicon Photonic Microring Resonator Platform with Applications for
the Detection of Nucleic Acids and Other Biopolymers**

by

Maria de la Cruz Cardenosa Rubio

A dissertation submitted in partial fulfillment
of the requirements for the degree of
Doctor of Philosophy
(Chemistry)
in The University of Michigan
2019

Doctoral Committee:

Professor Ryan C. Bailey, Chair
Professor Mark E. Meyerhoff
Professor James H. Morrissey
Professor Nils G. Walter

Maria de la Cruz Cardenosa Rubio

cardenom@umich.edu

ORCID iD: 0000-0001-8616-5030

© Maria de la Cruz Cardenosa Rubio 2019

DEDICATION

This dissertation is dedicated to those who help me in this stage and contribute to making me a better scientist. Especially to my parents, who have always been there to support me.

ACKNOWLEDGEMENTS

I would like to acknowledge my committee for their support and guidance during these projects. Thanks so much for your valuable pieces of advice and all the comments and feedback that have made this dissertation possible. I also would like to thank The Fundacion Bancaria La Caixa for funding my two first years in the program (tuition and monthly stipend) and my transition to the United States. Getting this fellowship was a challenge and a significant achievement for me. It taught me that sometimes we place our barriers and it is in our hands to believe we are capable of much more than we think. I also would like to thank the financial support from the National Cancer Institute of the National Institutes of Health through Grant CA177462 for the RNA projects and Rackham for the travel grants to attend conferences.

I would like to express my appreciation to my advisor Prof. Ryan Bailey. It was a hard decision to come here but after four years I do not regret it (even if I chose the cold and cornfields of Midwest instead of sunny and warm California). You have been a great advisor guiding me during these four years and contributing to my growth as an independent scientist.

I am also very grateful to Prof. James Morrissey and the Morrissey lab for all the contributions in the polyphosphate project. Thanks a lot for all the advice and the patience in dealing with me. This project was very new to me, but thanks to your advice and the great amount of assistance, it was finally possible. I would also like to acknowledge Prof. Robert Kennedy, for letting us use the capillary electrophoresis in his lab and the former graduate student Clarie Ouimet for instructing me in how to use the instrument.

Many thanks to all the Bailey lab members because I am sure in more than one occasion you have helped me with something. The completion of the RNA projects would not have been possible without the support and mentoring of Richard Graybill. I will always be very thankful for your patience and your calm even when the experiments did not work so well. Also, I am also very grateful to other former lab members. Heather Robinson, thanks for all the help establishing the polyphosphate project and being a great runner and friend. Sharing the windows desks with you

has been great. James Wade, you are a great scientist and person, it was always nice to talk to you, and I will be very grateful of all the guidance and knowledge, especially in the PDX project. Alex Stanton, I would always appreciate your invitation during my first Christmas alone in the United States, it was great meeting you and being your friend. Yi Xu, it was always nice to have you next to my desk and chatting about everything. You make hard days more bearable. Jamy Lee, you were my roomie in a very tiny apartment for two years, and we survive, so I will always appreciate you.

I also want to thank all the current lab members: Marina Sarcinella for her contribution in the polyphosphate projects and being a great student. Steve, for those great boardgame evenings and taking care of Edu, you are a great friend. Cole, a long list of thanks for many things: helping with experiments, giving me advice and feedback with research, making me feel bad because I used Origin, reviewing my grammar, being a great labmate... Gloria, our Spanglish conversations, being a good friend and all your support during the hard moments. John, trying to say a few words in Spanish, random visits to talk about science and developing the capillary electrophoresis system for the good of humanity. Sara, thanks for all your help with the trips to Marsh lab to get my results and taking care of the waste in the lab. Colleen, thanks for the culture of GBM cells and treatments, and also filling the chocolate drawer. Shannon, thanks for your knowledge and being kind to everybody and of course, also being a chocolate lover and filler of the drawer. Vishal, thanks for your advice in capillary electrophoresis and what to do with my future. Emily, you were excellent with the instrument repairs and taking care of group cleanup.

I would also extend my deepest gratitude to my parents who were supporting me every day in spite of the distance and time difference. I am very proud of you, and I would not be here without your support and education. I also want to thank all my friends in Ann Arbor and Champaign, to the dance community and RecSport. You make my days happier even in the difficult times. You will always be like my family.

Finally, to Edu. You made being here easier, although you also made it hard when you left. Thanks for your sacrifice staying here with me for a while, I wish things get easier for us now.

TABLE OF CONTENTS

DEDICATION	ii
ACKNOWLEDGEMENT	iii
LIST OF FIGURES	viii
LIST OF TABLES	xv
ABSTRACT	xvii
CHAPTER	
I. Biosensors and Whispering-gallery-mode biosensing applications	1
Introduction	2
Label-free optical biosensors	4
Environmental analysis using microring resonators	6
Microring resonators in clinical samples	8
Approaches in the study of RNA using microring resonators	10
Conclusions	14
Bibliography	24

II. Multiplexed microRNA expression profiling by combined asymmetric PCR and label-free detection using silicon photonic sensor arrays	34
Introduction	35
Experimental	37
Results and discussion	40
Conclusions	43
Bibliography	54
III. Combining asymmetric PCR-based enzymatic amplification with silicon photonic microring resonators for the detection of lncRNAs from low input human RNA samples	58
Introduction	59
Materials and methods	61
Results and discussion	64
Conclusions	67
Bibliography	80
IV. Dynamic profiling of miRNA and phosphoproteins in PDX derived cell lines under different treatments using silicon photonic microring resonators	84
Introduction	85
Methodology	87
Results and discussion	89
Conclusions	94
Bibliography	104
V. Quantification of PolyPhosphates using the microring resonators	110
Introduction	111

Methodology	113
Results and discussion	116
Conclusions	119
Bibliography	128
VI. Conclusions and future directions	131
Introduction	132
Multiplexed RNA detection with Microring Resonator Arrays	132
PolyPhosphate analysis with microrings	133
Size characterization of Polyphosphates using capillary electrophoresis	134
Bibliography	148

LIST OF FIGURES

FIGURE

- 1-1 Schematics of microring resonators as bioanalytical devices and working principle. A) Schematic representation of the elements constituting a microring biosensor device: analytes, biorecognition elements, transducer, and signal readout. B) Drop in the transmitted light intensity at the wavelengths that resonate in the microring cavity. C) Evanescent field sensing the boundaries of the microring and resonant shift when analytes bind. D) Main configurations of ring resonators: all-pass filters and add-drop filters. 16
- 1-2 Innovative configurations of ring resonators to incorporate other functionalities. A) Cross-section view of an Optofluidic Ring Resonator sensor. The WGM is excited by an optical fiber taper in contact with the OFRR. The evanescent field of the WGM penetrates the polymer layer, making it sensitive to absorbed molecules. Adapted from ³⁹ Copyright 2013 Elsevier Ltd. B) Selective electrografting of a pair of optical ring resonator sensors within the same microfluidic chamber. Microrings sensors are subjected to electrical fields for the selective functionalization via electrochemical reactions. Adapted from ¹⁸ Copyright 2016, Springer Nature. Innovative configurations of ring resonators to incorporate other functionalities. 17
- 1-3 Applications of microring resonators in environmental monitoring. 18
- 1-4 Applications of microring resonators in clinical analysis. 19
- 2-1 (A) Overview of the combined aPCR-microring assay. Isolated RNA is reverse transcribed and asymmetrically amplified to single strand products that are detected *via* hybridization onto the sensor array. (B) Schematic illustration of reverse transcription using stem loop probes and aPCR amplification. (C) Plot showing DNA amplification as a function of increasing cycle number. Double-stranded product is made until the limiting primer is consumed, after which

	further cycling yields single-stranded products. (D) Resonance wavelength shifts are only detected after the transition to single-stranded production, which allows amplicons to hybridize to capture sequences arrayed onto unique microring sensor elements.	44
2-2	(A) Resonance wavelength shifts for various concentrations of let-7f as a function of cycle number. Error bars are the standard deviation from $n \geq 8$ microrings. Each cycle-dependent trace is fit with a logistic function. (B) Concentration-dependent calibration curves for let-7f determined using both the 2nd derivative and linear thresholding methods.	45
2-3	Cross reactivity experiments showing target-specific responses as each single miRNA aPCR product is flowed across a sensor array.	46
2-4	Amplification Validation of miRNA Targets. In order to prove linear amplification of all miRNA targets, 200 nM, 20 nM, and 2 nM samples of each target were subjected to the aPCR-microring assay using a stem loop primer concentration of 200 μ M. The results validated the designed primer sets by displaying linear amplification profiles.	46
2-5	Resonance wavelength simultaneously measured by an array of microrings presenting capture probes for eight miRNAs after performing aPCR and hybridization analysis from a 10 ng input sample of (A) healthy brain total RNA, and (B) a representative primary glioma specimen (Subject A). (A and B) Results obtained when using a 10 ng input of a healthy control and glioma grade IV total RNA sample, respectively, and subjecting it to varying cycles of the aPCR-microring assay.	47
2-6	Heat map showing expression profiles from patient samples, relative to healthy control brain total RNA. Higher expression is indicated in red and lower in blue with numerical values plotted on a log ₂ scale.	47
2-7	Plots used to calculate C(t) values for each sample of interest.	48
3-1	Schematic outline of the overall assay for lncRNA detection including (A) reverse transcription, (B) asymmetric PCR, and (C) label-free, hybridization-based detection with microring resonator arrays.	69
3-2	Secondary structures of amplified regions obtained using the DinaMelt Web Server. The region that binds to the capture probe is highlighted with a red square. (A) β -actin amplified	

- region will not bind to complimentary capture probes due to excessive secondary structure. (B) β -actin amplified region after primer redesign that enables surface binding. (C) KIAA0495 amplified region with minimal secondary structure. (D) MALAT1 amplified region with minimal secondary structure. 70
- 3-3 Comparison of β -actin PCR product binding with and without optimized primer design. The red trace shows improved binding when using the optimized primer sets (predicted structure shown in in Figure 3.2b). The black trace shows data obtained using the PCR amplicon with a high degree of secondary structure (Figure 3.2A). At $t = 5$ minutes, the solution was changed from hybridization buffer to the amplicon-containing solution, then returned to hybridization buffer at $t = 20$ minutes. The larger positive resonance shift confirmed improved amplification with new primer design. 71
- 3-4 Agarose gel electrophoresis (2% agarose; SYBR Gold Stain) used to prove specific PCR amplification of lncRNAs and β -actin in (A) commercial brain and lung RNA samples; and (B) RNA isolated from GBM6 cells. 72
- 3-5 Verification of capture probe specificity. Each target was amplified individually in a separate volume of sample and then flowed across a sensor array containing capture probes for all targets. Large, specific hybridization responses were observed at appropriately-functionalized microring sensors for (A) KIAA0495, (B) MALAT1, and (C) β -actin. Buffer was initially flowed across the sensor array before the amplicon solutions were introduced at $t=5$ minutes. The solution was changed back to buffer after hybridization ($t=22$ minutes). Resonance shifts localized only to buffer/sample changes were due to differences in bulk solution refractive index. 73
- 3-6 (A) Detection of the KIAA0495 aPCR product from healthy brain total RNA at different cycle numbers. The amplicon solutions from each cycle number were sequentially flowed across the sensor array separated by brief returns to hybridization buffer. Real-time resonance wavelength shifts are shown for microrings functionalized with target-specific (red) probes. Increasing hybridization responses are clearly observed with increasing cycle numbers. Error bars represent \pm s.d. from $n=16$ replicate sensors. (B) Normalized hybridization response for KIAA0495 from healthy brain reference RNA as a function of

- cycle number. A C(t) value was assigned as the cycle number corresponding to 40% of the maximum hybridization response. 74
- 3-7 Microring traces used to calculate amplification plots in Figure 4. The trace signal represents the average of at least 8 replicate microrings simultaneously measure on the same chip minus the off control signal from non-specific functionalized rings. Error bars represent \pm s.d. for n=8-16 replicate measurements on the same microring sensor array. 75
- 3-8 Amplification curves for the lncRNAs and internal control target measured (A) Healthy brain total RNA, (B) Healthy Lung total RNA, and (C) total RNA extracted from GBM6 cells, a glioblastoma patient-derived xenograft sample. Error bars represent \pm s.d. from n=8-16 replicate measurements on the same chip. 76
- 3-9 Comparison of RNA target fold changes using the combined aPCR-microring resonator approach relative to conventional, single-plex RT-qPCR. Fold changes were calculated by normalizing to a β -actin internal control. (A) Comparison of lncRNA expression in GBM6 using healthy brain tissue as reference. KIAA showed slightly increased expression in the GBM6 sample, relative to healthy brain, but MALAT1 showed reduced expression in the xenograft cell line. (B) Comparison of KIAA and MALAT1 expression in healthy lung using brain tissue as reference Both KIAA and MALAT1 have slightly lower expression in lung tissue, relative to brain. 77
- 4-1 (A) Schematic of PDX cell culture. (B) EGFR/Akt/mTOR pathway with the treatments. 95
- 4-2 (A) Cell treatments and RNA extraction (B) Reverse transcription using stem-loop primers. (C) Asymmetric PCR (D) Sample collection and ring hybridization. 96
- 4-3 (A) Microring traces lines for the detection of 4 miRNAs from the serum control sample at time 0h. (B) Average net shifts as a function of cycle number for the detection of 4 miRNAs in the serum control sample at 0h. (Measurements were done simultaneously on eight miRNA and an off-target control, but for clarity, we have only plotted four). The average represents the signal of four microrings. 97

4-4	(A) Comparison serum over time for GBM6 (B) Comparison serum over time for GBM10 (C) Comparison DMSO over time for GBM6 (D) Comparison DMSO over time for GBM10.	98
4-5	(A) Comparison of Dacomitinib treatment over time for GBM6. (B) Comparison of Dacomitinib treatment over time for GBM10.	98
4-6	(A) Comparison of buparlisib treatment over time for GBM6. (B) Comparison of buparlisib treatment over time for GBM10.	99
4-7	(A) Comparison of dactolisib treatment over time for GBM6. (B) Comparison of dactolisib treatment over time for GBM10.	99
4-8	(A) Comparison of all the treatments for GBM6 (B) Comparison for all the treatments for GBM10.	100
4-9	(A) PCA biplot for all the treatments for GBM6 (B) PCA biplot for all the treatments for GBM10.	100
4-10	PCA biplot for all the treatments for GBM6 and GBM10.	101
5-1	Sensorgram of the binding events for the HRP-enhanced polyP detection: 1. PEI <i>online</i> functionalization. 2. PolyP binding in high salt concentration (500 mM LiCl). (Optional Urea rinse). 3. Biot-PPXbd binding. 4. SA-HRP binding. 5. 4CN enzymatic turnover.	120
5-2	Detection of 1 μ M polyP under different surface functionalization conditions: A) Comparison <i>offline</i> overnight surface functionalization and online functionalization with 5.4 ug/ml PEI in coating buffer in both cases B) Comparison <i>online</i> surface functionalization with 5.4 ug/ml PEI in coating buffer and without PEI.	121
5-3	(A) Standard concentration measurements checked by malachite green assay after PolyP digestion by ScPpx. (B) PAGE of different modes of PolyP: lane 1 (mode 76), lane 2 (mode 353), lane 3 (mode 708), lane 4 (mode 1100), lane 5 (mode 100), lane 6 (mode 700).	122
5-4	Standard curves of PolyP mode 76 and 1100 in buffer. The standard deviation of the measurements was calculated in based to the n>30 technical rings replicates.	123

5-5	Comparison of PolyP measurement in serum A) with 1M urea rinse and B) without urea rinse.	124
5-6	Calibration curves of PolyP mode 100 and 700 in serum. (Standard deviation was calculated from the n>30 technical ring replicates).	125
5-7	Calibration curve of PolyP mode 76 in platelet releasate matrix after PolyP digestion by ScPpx.	126
6-1	CE strategies to resolve polyP size. (A) Approach using a sieving matrix and indirect UV detection to resolve polyP. (B) Approach in free solution using a PPXbd as a probe with and without EOF as migration force.	143
6-2	(A) ϕ X174 DNA-HaeIII Digest visualized by ethidium bromide staining. 1.7% agarose gel (B) Electropherogram of 100 bp DNA ladder (C) Relationship between DNA length and migration time on 10% dextran 12% sorbitol Tris 25 mM pH 8.4 CGE.	144
6-3	Size-fractionated PolyP preparations resolved on 5% polyacrylamide gels. Lane 2: 61-104 Pi; Lane 3: 217-459 Pi; Lane 4: 570-852 Pi and Lane 5: 970-1370 Pi.	144
6-4	Electropherograms for polyP fragments (mode 76, mode 353, mode 708 and mode 1100). (A) 100 μ M polyP fragment mixture separated using a 10% dextran matrix. (B) 250 μ M polyP fragments separated in 15% dextran matrix.	145
6-5	Electropherograms for polyP fragments (mode 76, mode 353, mode 708 and mode 1100). (A) Blanks and 500 μ M polyP fragment mixture separated using a 10% w/v dextran in 25 mM Tris 5 mM PMA. (B) 250 μ M polyP fragments separated in 15-20% dextran matrix in Tris 50-75 mM Tris and 5 mM PMA.	145
6-6	Electropherograms for 250 μ M polyP fragments (mode 76, mode 353, mode 708 and mode 1100) using a 20% w/v dextran matrix and 5 mM PMA in 50 mM Tris buffer.	146
6-7	PAGE analysis of lane 1: 1 μ g/ml PPXbd; lane 2: 1 μ g/ml PPXbd conjugated with 100 μ M PolyP mode 76; lane 3: 1 μ g/ml PPXbd conjugated with 100 μ M PolyP mode 353; lane 4: 1 μ g/ml PPXbd conjugated with 100 μ M PolyP mode 708; lane 5: 1 μ g/ml PPXbd conjugated with 100 μ M PolyP mode 1100.	146

6-8 Free solution electropherograms for 20 $\mu\text{g/ml}$ purified PPXbd, 100 μM polyP fragments + 20 $\mu\text{g/ml}$ PPXbd (mode 76 and mode 1100) using 50 mM Tris –glycine as running buffer with addition of 30 mg/ml PEG. 147

LIST OF TABLES

TABLE

1-1	Recent advances in microring resonators for environmental analysis.	20
1-2	Recent advances in microring resonators for clinical analysis.	21
1-3	Conventional techniques for the analysis of RNA molecules.	22
1-4	Previous RNA detection protocols developed in the Bailey lab using microring resonators.	23
2-1	Summary of nucleic acid sequences.	52
2-2	Details on fluid flow conditions.	52
2-3	Patient information	53
2-4	Fold changes presented in heat map (\log_2).	53
3-1	Primers (RP, reverse primer; FP, forward primer) and capture probes (CP) used in the experiments for reverse transcription (RT), asymmetric PCR, and RT-qPCR. Melting temperatures for primers were calculated using the Primer-Blast platform.	78
3-2	Fluidic handling protocol for the ring hybridization steps.	78
3-3	Calculated qRT-PCR and microring C(t) values from healthy brain, healthy lung, and GBM6 RNA samples. The RNA input for qRT-PCR experiments was 40 ng, and the qRT-PCR experiments were completed in triplicate.	79
4-1	Summary of nucleic acid sequences.	102
4-2	Inhibitors for the treatment of xenograft cell cultures.	102

4-3	miRNA panel used in the study.	103
5-1	Buffer recipes.	127
5-2	Analysis of spiked polyP mode 76 and 1100 in buffer using the microring resonators.	127
5-3	PolyP content from platelet releasates.	127

ABSTRACT

Progress in the development of biosensors has dramatically improved analytical techniques. Biosensors have advantages over more conventional analytical techniques arising from attributes such as straightforward analyses, higher throughput, miniaturization, smaller sample input, and lower cost. Specifically, silicon-based biosensors including microring resonators have led to major advances in diverse applications because they produce sensors that can be arrayed in planar substrates for multiplexed detection and can be produced at large scales. This dissertation presents how microring resonators have been used for the detection of ribonucleic acids, RNA, and other inorganic biopolymers.

The first chapter describes the basics of biosensors and the factors that affect their operation. This chapter is also dedicated to the sensing mechanism of whispering gallery mode biosensors, in the form of microring resonators. In addition, it summarizes the most recent applications of microrings in environmental and clinical analysis, highlighting the research in RNA detection.

The next two chapters describes an approach for RNA detection utilizing the microring resonators. This methodology is based on the coupling of a nucleic acid amplification technique, asymmetric Polymer Chain Reaction, aPCR, with the microring resonator platform. Promising results are shown in the detection and quantification of RNA, where our approach offers the sensitivity and selectivity required for the use of transcripts in clinical analysis. Compared to other biosensing strategies, we are able to perform a higher multiplexity of the measurements, use nanogram sample input, and adapt the protocol to the detection of short (microRNAs) and long transcripts (long non-coding RNAs).

The fourth chapter presents how the aPCR-microring combination can be applied to the profiling of a miRNA biomarker panel. The investigation consists of an analysis of the dynamic miRNA signatures of two glioblastoma cell lines upon various treatments. Furthermore, I utilized

the normalized expression of the miRNAs to construct heatmaps and performed multivariate statistical analysis. The results indicated that this technology makes it possible to carry out functional screening of targets for diagnostic and therapeutic evaluation.

The fifth chapter features an innovative application of microrings in the quantitative analysis of polyphosphate, also known as polyP. PolyP is a ubiquitous molecule, interest in which has increased over the last decade because of the discovery of its important biological roles in mammals and microorganisms. However, methodologies for its analysis still fall short in identifying ways to quantifying polyP directly in complex matrices. To detect polyP in complex matrices, molecules are captured in the surface via high-affinity binding to cationic polymers. Then, we integrated a selective recognition of the molecules via a polyphosphate binding protein domain. This strategy enabled the detection of nanomolar concentrations and the measurement of the molecule directly in the matrix with no purification and thus, it opens up a variety of potential applications.

The final chapter summarizes all the research carried out during my thesis. The possibilities that microring resonators have to offer as biosensors, and the diverse approaches that can be combined to enhance the characterization of molecules. In the field of RNA, future directions will include the combination of RNA expression panels with the profiling of other biomarkers to understand better the signatures of patient samples under therapeutic treatments. In the field of polyP, future directions in the analysis of polyP are the size characterization of these polymers using other separation instruments such as capillary electrophoresis (CE).

Keywords: biosensor, microrings, asymmetric PCR, noncoding RNAs, polyphosphates, capillary electrophoresis

CHAPTER I

Biosensors: Whispering-gallery-mode biosensing in analytical chemistry

Acknowledgments:

I would like to acknowledge the contribution of Heather Robinson helping with the review and proofreading of sections 2.1, 3 and 4 from this chapter.*

Abstract

The progress in clinical analysis and environmental monitoring have increased in the past decades because of the advancement in biosensors, device miniaturization and microfluidic integration for sample automation. Whispering Gallery Mode sensors and microring resonators have emerged in the area of optical sensors as an exceptional choice due to their sensitivity, ease of fabrication and label-free detection. The first section describes the working principle of microring resonators and outlines the most recent and relevant applications in clinical investigation and environmental surveillance. The final section of the chapter highlights the importance of RNAs as biomarkers and previous approaches in the Bailey lab to detect these molecules.

* This sections will form part of an invited submission in *Current Opinion in Environmental Science and Health*, April 2019.

1. Introduction

More than half a century since the elucidation of the glucose biosensor by Clark ¹, biosensors have revolutionized the field of chemical and biological analysis. Offering excellent sensitivity and selectivity, biosensors can provide a complex measurement in an easy-to-use format ². Biosensors are analytical devices that convert a biological interaction or recognition into a measurable electronic signal. They are generally made in a solid phase support that include three parts (**Figure 1-1A**): a recognition element, a transducer, and an electronic readout. The recognition element is usually a biomolecule such as an enzyme, an antibody, or a nucleic acid; although, other polymers and selective compounds may be used. The biosensor is classified by the signal transducer which are described as electrochemical, optical, or acoustic.

1.1. Relevant parameters in solid surface sensors

There are multiple factors to consider when optimizing or developing a new biosensor platform. The next section describes some of the most critical parameters for solid surface sensors.

Surface chemistry

One of the fundamental parts of the functioning of biosensors is to couple the receptor molecules to the surface. The biomolecular recognition is typically driven by many weak interactions working in concert. Therefore, the receptors must be attached to the surface while maintaining the structural conformation and binding affinity to the analytes.³

The main strategies for immobilization rely on: physical adsorption of the receptors onto the solid support, the encapsulation or grafting of the receptors into polymeric networks, the chemical grafting of the receptors by covalent binding onto reactive groups or the conjugation to modified biomolecules. The physisorption and encapsulation technique are the simplest, but also the least stable, as the functionalization strongly depends on pH, solvent, and temperature. The chemical immobilization which includes covalent binding and crosslinking is more stable and allows one to immobilize molecules more controllably. However, it is more complex and requires chemical modification of the biomolecules that could affect their conformation. This technique usually takes advantage of the functional groups of the biomolecules such as primary amines, thiols, carboxyl groups or carbonyls.⁴

When choosing the immobilization method, the main factors to consider will be the orientation of the receptor, the local environment of the surface and the stability of the linkage between the surface and the receptor.⁵ Also, it is essential to make the uncovered parts by the receptor inert to non-specific interactions that will cause the background noise of the sensor.

Mass transport

Mass transport from the bulk fluid to the substrate is another critical parameter because most of the biosensors require molecules to reach a receptor bound on a solid surface. Mass transport limitation can decrease sensor performance and is predominant under two conditions. The first case when the analyte is large, and the second case when the binding kinetic is higher than its diffusion. In order to limit mass transfer effects, different ways have been devised. One of the methods is increasing the rate of diffusion by increasing the flow rate, and thus the faster delivery of the analyte to the surface⁶. However, this method have the trade-off when the flow rate is too high, the analyte has less time to interact with the surface. The second method consists of lowering the levels of receptors immobilized on the surface. When less amounts of receptors are immobilized, less analyte will need to diffuse for the interaction to happen. However, there is also a trade-off with the signal noise ratio in this case as the saturation signal will be lower.⁶

Blank controls

Another factor to consider in these sensors is the introduction of negative surface controls. These controls are subtracted from the target signal to correct some artifacts such as signal drift, non-specific binding, and other bulk effects.⁵

Multiplexed detection systems

As the name indicates, multiplex detections are concerned with the simultaneous detection of different analytes from a single sample. Technologies able to produce this kind of screening have gained much attention due to the impact of these methodologies for the improvement of clinical diagnostics. When talking about disease diagnostics, it is very critical to have an early and accurate diagnosis of a specific disease to give adequate treatment. However, clinical evidence based on a single biomarker is not always appropriate for disease diagnosis and treatment monitoring⁷. Therefore, the ability to detect several biomarkers and create patterns of expression or quantitation

that correlate to the diagnosis, the prognosis or therapeutic efficiency has become crucial in the last decades when developing new testing devices.

2. Label-free optical biosensors

Most of the biosensing platforms usually require some labeling to display the interaction between the analyte and the receptor. The flaws in these reporting systems are the cost and the possibility of modification of the analyte giving some false meaning to the assay. The majority of the labels depends on fluorescence, radioactivity or enzymes that can amplify the signal. However, in the last years, other technologies that can report the binding of the analyte without the presence of labels have been appearing in the research literature and the market. Such is the case of optical biosensors, acoustic biosensors, and micro-calorimetry⁵.

Label-free optical sensors constitute one of the most conventional types of biosensors because they can provide direct, real-time measurement of molecules. These transducers work by assessing the interaction of an optical field with a recognition element without the need for secondary target labels (e.g., Fluorophores, enzyme tags). This group includes platforms such as surface plasmon resonance (SPR)⁸, interferometers⁹, and whispering gallery mode sensors¹⁰. These sensors similarly are able to confine light at an interface with the surrounding (sample-containing) medium. At this boundary an evanescent field extends into the surrounding region such that the local optical properties are sensitive to binding interactions at or near the surface (**Figure 1-1C**).¹¹

2.1. Microring resonators

Whispering gallery mode (WGM) biosensors confine photons in a path circumscribing the circular cavity. These photons can recirculate many times around the cavity allowing for small changes in the recirculating path to be detected with high sensitivity. Facilitating these analyses are a tightly held resonance condition that is established based upon a constructive interference condition at the junction between the coupling waveguide and circular path of the cavity. This resonance condition is defined mathematically by the following formula (**Figure 1-1B**):

$$m\lambda = 2\pi r n_{eff}$$

where m is a non-zero integer, λ is the wavelength traveling in the waveguide, r is the radius of the cavity and n_{eff} is the effective refractive index sampled by the optical mode traversing the cavity. Thus, changes in the local refractive index (a component of n_{eff}) will lead to a shift in the resonance wavelengths supported by the cavity (**Figure 1-1C**). Most WGM sensors operate by measuring the shift in wavelength due to binding-induced changes in the local refractive index, though sensors based upon measurement of the broadening¹² and splitting¹³ of resonances have also been successfully demonstrated.

WGM sensors have been produced in several different geometries, including include microspheres, toroids, disks, and rings¹⁰. Microrings have been the most common geometry for biosensing. The ring geometry, usually attached to planar underlying substrates, provides many advantages in the ease of construction using CMOS- (Complementary metal–oxide–semiconductor) compatible semiconductor fabrication approaches. The planar substrate geometry is also amenable to the creation of multiplexed sensor arrays. Microring resonators can be easily fabricated from semiconductor materials that have refractive indices such that the resulting waveguides feature good light confinement. Common materials systems include silicon (typically silicon-on-insulator), silicon carbide and silicon nitride¹⁴; however, other materials including polymers have been demonstrated as potential lower cost alternatives that offer unique chemical properties¹⁵.

Ring resonators can be configured as all-pass filters or add-drop filters (**Figure 1-1D**)¹⁶. In the all-pass filter configuration, which only requires a single linear waveguide, shifts in optical properties are simply recorded as changes in the transmission spectra measured past the resonator. In contrast, the add-drop filter configuration utilizes two waveguides positioned on either side of the resonator. Light is coupled into the resonator via the input waveguide and the signal measured (or “dropped”) into the output waveguide are monitored to as a read out of binding to the resonator surface.

Although planar substrate microring arrays have been most commonly reported, optofluidic microring resonators have been impressively developed¹⁷. Optofluidic microring resonator devices often consist of a thin wall capillary, wherein the cross section acts as a whispering gallery mode sensor (**Figure 1-2A**). Analytes flow inside the capillary interacting with the evanescent field from

the inner surface. The ease and relatively low cost of integrating the microfluidics with this sensing modality are particularly advantageous¹⁷.

Among other newer hybrid configurations are electrochemical silicon photonic resonators, which are optimally n-doped to support the resonant mode simultaneously with electrochemical events at the sensing surface (**Figure 1-2B**). The electrochemical activity of this interface can also enable site-selective immobilization of biomolecules to create sensor arrays¹⁸.

While the next sections focus almost exclusively on progress from academic laboratories that are driving new applications and advances in this field, it is worth noting that microring resonators have already been commercialized by Genalyte, Inc.¹⁹. Genalyte has demonstrated the ability to detect autoantibodies that are diagnostic signatures for a range of connective tissue disorders^{20,21}, and their commercial products have found early adoption in clinical laboratories. The two following sections review the most recent applications of ring resonators for environmental and clinically-relevant sensing. Key figures of merit compared include type of analyte, detection strategy, limits of detection, and demonstrated ability of operation within complex sample matrices. .

3. Environmental analysis using microring resonators

In the environmental analysis, microring resonators have been utilized to detect diverse chemical species including gases, heavy metals, pesticides, explosives, biological toxins, and whole microorganisms. Selected examples are described in the following text, and also summarized in **Table 1-1** and **Figure 1-3**.

For the detection of gases, a demonstrated strategy combined microrings with materials that are chemically responsive to the gas (**Figure 1-3A**). One example utilized microrings modified with a hyperbranched carbosilane polymer that changed the microring absorption spectrum upon exposure to trace levels of phosphonate ester nerve agents²³. Another example introduced a Palladium microdisk within the microring architecture that expanded upon hydrogen exposure, leading to a resonance shift upon hydrogen incorporation into the structure. Using this strategy, the reported sensitivity was as high as 11.038nm expansion/% hydrogen, resulting in a ~23% enhancement compared to other hydrogen WGM sensors²⁴. Yet another example of

environmentally-relevant target analysis involved the detection of dimethyl methylphosphonate (DMMP), a precursor of sarin nerve gas that is often used as a model analyte. In this case, the microring surface was functionalized with bovine odorant-binding proteins (b-OBP) mutated to have a high affinity for DMMP. This approach yielded a limit of detection (LOD) of 6.8 ppb without the need for sample pre-concentration ²⁵.

Microring modification approaches have also been shown to be effective in detecting environmentally-relevant targets in aqueous environments (**Figure 1-3B**). Microrings have been modified with a mesoporous silicate to extract heavy metals from aqueous solutions. The uptake of the mercury and lead into the mesoporous silica matrix led to changes in the refractive index of the microrings, resulting in a measurable change in the sensor signal down to 1 ppm in concentration ²⁶. Microring resonators have also been modified with polymer brushes using atom transfer radical polymerization. Different polymer brushes can impart chemical selectivity via partitioning, as was demonstrated for several small molecule organic analytes, including organophosphorus simulant. Furthermore, the magnitude of the resonance shift was found to be directly related to target concentration, providing an approach for quantitative monitoring of water contaminants ²⁷.

Microrings have also served as a useful technology for detecting biological toxins in environmental water and food samples (**Figure 1-3C.1**). One target has been aflatoxin M1, a mycotoxin from *Aspergillus* that can be found in milk products. Microrings were functionalized with aptamers or antigen-binding Fab' fragments to selectively detect the toxin in milk with limits of detection of 5 nM ²⁸. Another naturally occurring and potent toxin, the lectin ricin, which can be isolated from castor beans has also been detected using a microring-based approach. Sensors functionalized with single-domain antibodies were found to be selective for ricin over other similar toxin compounds with a limit of detection of 300 pM in just a 15 minute assay ²⁹. Silicon nitride microring resonators have also been employed for the multiplexed detection of of *Aleuria Aurantia* Lectin (AAL) and *Sambucus Nigra* Lectin (SNA) with glycan-functionalized sensors giving limits of detection of 7 pM and 86 pM, respectively ³⁰.

Microrings have also been explored for the detection of whole organisms in environmental samples (**Figure 1-3C.2**). In one example, *Bean pod mottle virus*, one of the most common viral

soybean pathogens that can limit crop yields when fields are infected, was detected using microrings functionalized with an antibody that recognized an outer capsid glycoprotein on the virus. Using this strategy, a limit of detection of 10 ng/ml was achieved for whole, intact virus particles, and, importantly, this assay was shown to be able to detect the virus directly from ground soybean leaf samples in less than 45 min³¹.

4. Microring resonators in clinical samples

Applications in multiplexed clinical diagnostics have fueled much of the development of microring resonators as a biosensing platform, and not surprisingly they have been broadly applied to many classes of clinically-relevant biomolecular targets. By attaching different types of target-specific capture agents to localize antigens to the sensor surface, microrings have been demonstrated for the quantitative detection of different types of nucleic acids, proteins, smaller biomolecules, and whole microorganisms, in the context of human health applications. Selected examples are described in the following text, and also summarized in **Table 1-2** and **Figure 1-4**.

The detection of nucleic acids commonly relies on the functionalization of the sensor surface with oligonucleotide probes that are complementary to the sequence of interest (**Figure 1-4A**). Although direct detection of nucleic acids has been reported³²⁻³⁵, recent improvements in the LOD and required sample input have led to the integration of DNA replication by Polymerase Chain Reaction (PCR) or isothermal amplification and other PCR-free signal amplification schemes. For example, microring resonators were combined with recombinase polymerase amplification to detect the insertion DNA sequences from *Mycobacterium tuberculosis* in sputum samples³⁶. This amplification strategy allowed for the multiplex detection of two tuberculosis biomarker sequences down to 3.2 or 12 copy numbers per the 10 μ L reaction volume. Similarly, the combination of DNA amplification and microring array-based detection demonstrated successful multiplexed miRNA detection³⁷. In this work, miRNAs sequences were amplified via asymmetric PCR, a variant of PCR that produces single-stranded DNA products. By functionalizing arrays of microrings with complementary hybridization capture probes, multiplex expression of a nine miRNA panel from glioma patients were compared to a healthy control using a total RNA sample input of 10 ng. Importantly, the combination of asymmetric PCR and microring resonators have also been utilized in the analysis of long-non coding RNAs, lncRNAs, showing a good agreement

with conventional qPCR³⁸. On the other hand, low limits of detection have also been possible without the need of gene replication by adding other signal amplification strategies. For example, nM levels were reported for the multiplex detection of miRNA by adding complementary biotinylated primers and horseradish peroxidase amplification signal³⁹.

Protein-detecting immunoassays have been realized on microring resonators often using antibodies for the recognition of the target epitopes (**Figure 1-4B**). Although microrings possess exquisite sensitivity, this class of assays have also benefited from the use of secondary amplification (similar to Enzyme-Linked Immunosorbed Assays, ELISA) for enhanced selectivity and improved LOD. Early reports using antibody functionalized microrings demonstrated the label-free detection of carcinoembryonic cancer (CEA), a glycoprotein secreted in blood and has been established as a biomarker for many human cancers⁴⁰, as well as the creation of relatively simple label-free, multiplexed detecting arrays⁴¹. To increase the selectivity of protein biomarker assays—particularly those targeting complex human sample matrices—tracer antibodies have been employed in sandwich immunoassay formats⁴². Beyond the added selectivity, these assays also present strategies for improving attributes such as assay dynamic range and limit of detection⁴⁰. Candidate signal enhancement strategies include layer-by-layer biorecognition, which was applied to the analysis of cancer biomarkers in serum⁴³, and an enzymatic enhancement method that generated a spatially-localized precipitate on microrings that yielded subpicogram per milliliter limits of detection for inflammatory protein targets⁴⁴. This enzymatic enhancement strategy has been demonstrated as robust for multiplexed protein detection from within clinical matrices, including the analysis of phosphoprotein levels from brain cancer samples¹⁴ and identification of cytokine signatures in secreted cell supernatants that have promise for the diagnosis of latent tuberculosis infection⁴⁵. Another signal enhancement strategy applied to microring resonator-based detection of viral glycoproteins in saliva and blood involved streptavidin-coated beads⁴⁶. And in addition to antibody capture agents, microrings presenting immobilized aptamers have also been utilized for detection, including the detection of thrombin and IgE with limits of detection of 50 ng/ml⁴⁷.

Microring resonators have also been used in the detection of clinically relevant small molecules such as hormones or glucose (**Figure 1-4C**). A layer of molecularly imprinted polymer (MIP) was used to analyze for testosterone in aqueous samples down to 48.7 pg/ml⁴⁸. The MIP layer is interesting for analytical applications due to their potential for improved stability compared

biological-based capture agents, such as antibodies. Optofluidic ring resonators have also been utilized to quantitate glucose with a LOD of 35 μM , which is one order of magnitude lower than nominal clinical ranges⁴⁹.

Microring resonators have also been applied to the detection of whole pathogenic organisms and mammalian cells of clinical relevance (**Fig. 1-4D**). An early example included the detection of *E. coli* using microrings functionalized with monoclonal antibodies against the bacteria, demonstrating a LOD of 105 CFU/ml⁵⁰. CD4+ and CD8+ lymphocytes were also detected at 200 cells/ μL concentration with an optofluidic microring resonator that was, again, facilitated by immobilization of target-specific antibodies on the resonator surface⁵¹.

5. Approaches in the study of RNA using microring resonators

5.1. Importance of RNA as biomarkers

The overall objective of the first stage of my dissertation was to establish a multiplexed assay for the detection of two types of non-coding RNA molecules using a microring resonator detection platform. Observing the central dogma in biology, RNA is crucial in the information translation from the genome to the cellular functioning. Therefore, it is inferred that any change in the cells would be reflected in the expression of those transcripts. Their identification and quantification have been used for disease diagnostics, prognosis and therapeutic efficacy of treatments.

The first well studied RNA biomarkers were messenger RNAs, mRNAs. These RNAs are the ones that codify for proteins, and their differential expression can be directly correlated with disease pathology⁵². With the advent of high throughput technologies, many investigations have compared the transcriptome of disease states versus healthy conditions and defined transcripts involved in disease diagnostic and progression⁵³. For example, Sparano et al. identified a panel 21 mRNAs to help identify the risk of recurrence and treatment efficacy in breast cancer patients⁵⁴.

However, 90% of the genome is transcribed, and only 4% of these corresponds to mRNA, meaning that many transcripts do not code for proteins. Some of the noncoding RNAs whose functions have been well characterized include ribosomal RNA (rRNA), transference RNA (tRNA), small nuclear (snRNA) and small nucleolar RNA (snoRNA). In addition, the advances in

sequencing techniques have made possible the discovery of other abundant noncoding regulatory sequences⁵⁵. Some of the most studied sequences are microRNA (miRNAs) and small interference RNAs (siRNAs). MiRNAs are short sequences of RNA molecules of about 22 nucleotides that can modulate the expression of genes by binding complementary to mRNAs. In the maturation process, these transcripts get associated with the RNA-silencing complex (RISC). Then, this complex targets the specific transcripts producing the translational repression or mRNA degradation⁵⁶. Experts have discovered numerous roles of miRNAs involved in cell differentiation, proliferation, apoptosis and signal transduction. Because of their role in critical cell function, they show abnormal expression patterns in disease states, and demonstrate potential as biomarkers and therapeutic targets⁵⁷. MiRNAs have been extensively studied as biomarkers for different types of cancer as well as other pathologies such as neurological disorders⁵⁸, cardiovascular diseases⁵⁹, and viral infections⁶⁰. Some of the advantages of miRNAs biomarkers are their presence and stability in biofluids; therefore, being good candidates for non-invasive diagnostic approaches⁵⁷.

Besides the discovery of miRNAs, RNA sequencing has also led to the discovery of other longer noncoding transcripts (>200 nucleotides). These transcripts are called long noncoding RNAs, lncRNAs, and show widespread functionalities. Some lncRNA roles include chromatin modification (e.g., HOTAIR silences transcription by inducing a repressive chromatin state through the chromatin remodeling complex, PRC2⁶¹; Xist mediates the inactivation of the X chromosome also by recruiting PRC2⁶²) and transcriptional activation/repression (e.g., Air, the natural antisense transcript of IGf2r, can induce its epigenetic silencing and neighboring stream genes⁶³). There has also been much evidence of how their regulatory roles make them good candidates for biomarkers in cancer^{53,64}, infectious diseases⁶⁵, and other cardiovascular⁶⁶ and neurological⁶⁷ disorders.

5.2. Conventional and innovative methods in the study of RNA

The conventional methods for the study of RNA expression are divided in low-to-mid plex such as northern blot, in-situ hybridization, reverse transcription quantitative PCR (RT-qPCR) and higher-plex technologies such as DNA microarrays and RNA sequencing, RNAseq (**Table 1-3**). Northern blot is the oldest technology. Similarly to other blotting techniques, it is based on the separation of RNA molecules by gel electrophoresis followed by the transferal of the molecules to

a membrane where the RNA is incubated with tagged probes. This technique is relatively easy to perform, but it is not very quantitative and not scalable to many genes. In-situ hybridization is a technique used for the identification of gene expression directly in tissue sections or cells, but it is not practical for quantification or study of several genes. RT-qPCR has been defined as the “gold standard,” and it is the method of preference when validating results⁶⁸. Although considered the gold standard, multiplexing is complicated, and the sequence of the genes must be known in advance. Microarrays and RNAseq have made possible the study of the whole genome, studying the relative expression of analytes, and RNAseq being able to discover new transcripts⁶⁹. Microarrays examine transcripts that hybridize to probes that have been previously spotted on a chip and can study the relative gene expression by fluorescent methods⁷⁰. Some of the limitations of this technology are cross-hybridization of similar sequences, the limited dynamic range of detection because of background and saturation, and the need of normalization methods for comparing expression levels.

The most advances have been conducted in the development of next generation RNAseq, technologies. These methods have revolutionized our biological knowledge incorporating new transcripts that could be used as biomarkers and therapeutically targets⁷¹. Next generation sequencing techniques are currently more affordable, and there have been initiatives to include them in the clinic. Compared to other methods, RNAseq is more advantageous because of they can measure rare transcripts, splice variants, and non-coding RNA species. However, there are still some challenges such as the sample and library preparation, the biased results due to different protocols and the complicated downstream computational analysis⁷². These challenges have promoted international collaborations to establish data repositories such as RNAcentral⁷³ or NONCODE⁷⁴, among others, that can be used as references for the recognition of markers and expression patterns in the diagnosis of pathologic conditions.

The knowledge and potential of RNA molecules have motivated the emergence of innovative analysis techniques. In order to be used in clinics, these techniques had to be sensitive and quantitative while reducing the cost and sample processing requirement. Many emerging techniques have employed optical sensors, electrochemical sensors, and other nanomaterials⁷⁵.

In the optical sensor field, some of the platforms that have been optimized to detect RNA molecules are SPR, surface enhanced Raman spectroscopy (SERS), whispering gallery mode sensors and Forster Resonance Energy transfer (FRET). One example of SPR sensing corresponds to the studies of Huertas et al⁶⁵. In this work, researchers designed an SPR sensor for quantifying cancer specific variants of Fas mRNA⁷⁶. SERS is a sensitive vibrational spectroscopy technique which has been used extensively in biodetection. Su et al. demonstrated how uniform silver nanostructures with stable SERS signal could be used in the detection of miRNAs⁷⁷. In the field of fluorescence, many groups have also developed technologies for the detection of RNAs, most of them based on the FRET phenomenon. For instance, Qiu and Hildebrandt used quantum dots (QD) to develop a time-gate FRET (TG-FRET) sensor. This multiplexed sensor consisted of the energy transfer between a luminescent terbium complex to different emission QD dependent on the signal. With this sensor, they detected three miRNA with LOD 1 nM in samples that contain up to 10% serum⁷⁸.

There has also been much work done in the development of electrochemical sensors for RNA detection. These methods usually involve the hybridization of the targeted sequences to oligonucleotide probes bound to the surface of an electrode. Their detection is then read via voltammetry, amperometry or impedimetric approaches depending on the label that causes the signal. For example, one typical strategy in this type of methodology is a solid electrode with single-stranded oligonucleotide probes that contain electroactive reporters. The hybridization of complementary RNA changes the conformation of the probe that approaches or moves away from the reporter producing the electrochemical signal⁷⁹.

5.3. Previous attempts for the detection of RNA using microring resonators

Over the past eight years, there have been several attempts on the detection of RNA using the same measurement technology in our lab. These attempts are summarized in **Table 1-5**. The targets of most of them have been miRNA^{32,39,80}, due to their impact as biomarkers, but there has also been other work dedicated to other RNA targets, tmRNA⁸¹ and mRNA⁸².

Some of the previous work in the miRNA analysis has been using direct detection, only measuring the shift caused by the RNA molecules hybridizing to complementary probes in the surface, such as the first work in miRNAs and the work in tmRNA. However, as it can be observed,

by adding a secondary signal amplification step, the limit of detection and especially the input amount could be significantly improved.

The first work carried out in our group by Qavi involved the direct detection of miRNAs and the quantification of the transcripts by the steepness of the slope of binding isotherms. This work proved the utility of the microring as a detection platform for the quantitation of the platform and the possibility to do multiplex assays³². The next work also carried out by Qavi later in that year, showed that adding a secondary amplification such as antibodies able to recognize DNA: RNA hybrids could improve the LOD from the nM to the pM level in addition to the decrease of the input sample⁸⁰. The next work in the detection of miRNA was produced by Graybill et al. in 2016. In this case, a secondary amplification was also utilized to decrease the LOD. The secondary amplification consisted of the use of a biotinylated primer that complementary bound to the cDNA of the different miRNA sequences. The sample input was also reduced compared to the initial attempts, and the cost was reduced by using biotinylated sequences instead of antibodies³⁹.

In the detection of longer transcripts, the Bailey lab has worked on the detection of two different molecules previous to this dissertation: mRNA⁸² and tmRNA⁸¹. The primary challenge with longer molecules is the formation of secondary structure that constrains the binding of the transcripts to the capture probes surface. For the detection of tmRNA, three strategies were used: thermal denaturation, chaperones, and fragmentation. From the three methods, fragmentation showed the best kinetics for the binding and overall signal enhancement. However, in the detection of mRNA, the use of chaperones sequences was used to help reduce the secondary structure of the sequences. tmRNA analysis did not include secondary amplification because the amount of tmRNA molecules is very high in bacteria. In the case of mRNA, the inclusion of streptavidin beads for secondary amplification helped to reduce the LOD as well as the input sample.

The objective of the first stage of this thesis was to optimize the detection of two noncoding RNA molecules, miRNAs and lncRNAs. In order to reduce both the LOD and input sample, we introduced PCR to amplify the signal. For the detection of these transcripts, we first performed a reverse transcription of the RNA followed by asymmetric amplification. Asymmetric PCR is a type of amplification that uses a different ration of primers so that after a certain cycle, there is no longer double stranded DNA production but single stranded DNA⁸³. This is crucial in our

technology as we need ssDNA to hybridize in the surface probes. In addition, lncRNAs are longer transcripts that contain much secondary structure, and so by using aPCR we could limit the size of recognition and facilitate the binding to the surface. The strategy and results are described in the next two chapters.

6. Conclusions

Over the past 10-15 years, microring optical resonators have emerged as one of the most promising and multiplexable platform for clinical and environmental analysis. Attributes such as amenability to mass production (for silicon photonic resonators, in particular) and microfluidic integration (for optofluidic resonators) give these technologies inherent advantages for analyses that need to be performed in high numbers and from small sample volumes. These sensors can act in label-free assay formats; however, for many applications requiring high selectivity and low limits of detection, more complex assays requiring labels have been successfully employed. The myriad of analytical targets that have been demonstrated to be analyzed using microrings is vast—largely on account of the fact that any target that can be physically localized to the surface via a capture agent that provides selectivity is theoretically detectable. This chapter has tried to balance a historical context for technology development with a focus on recent advances that demonstrate new capabilities as well as important applications of real-world relevance. The microring transduction technologies themselves have become quite mature; however, there are remaining challenges for the field that increasingly include improved methods of sample delivery and integration with complementary technologies in such a way to facilitate hyphenated analyses that also include, for example sample pre-treatment via chromatographic methods⁸⁴.

FIGURES

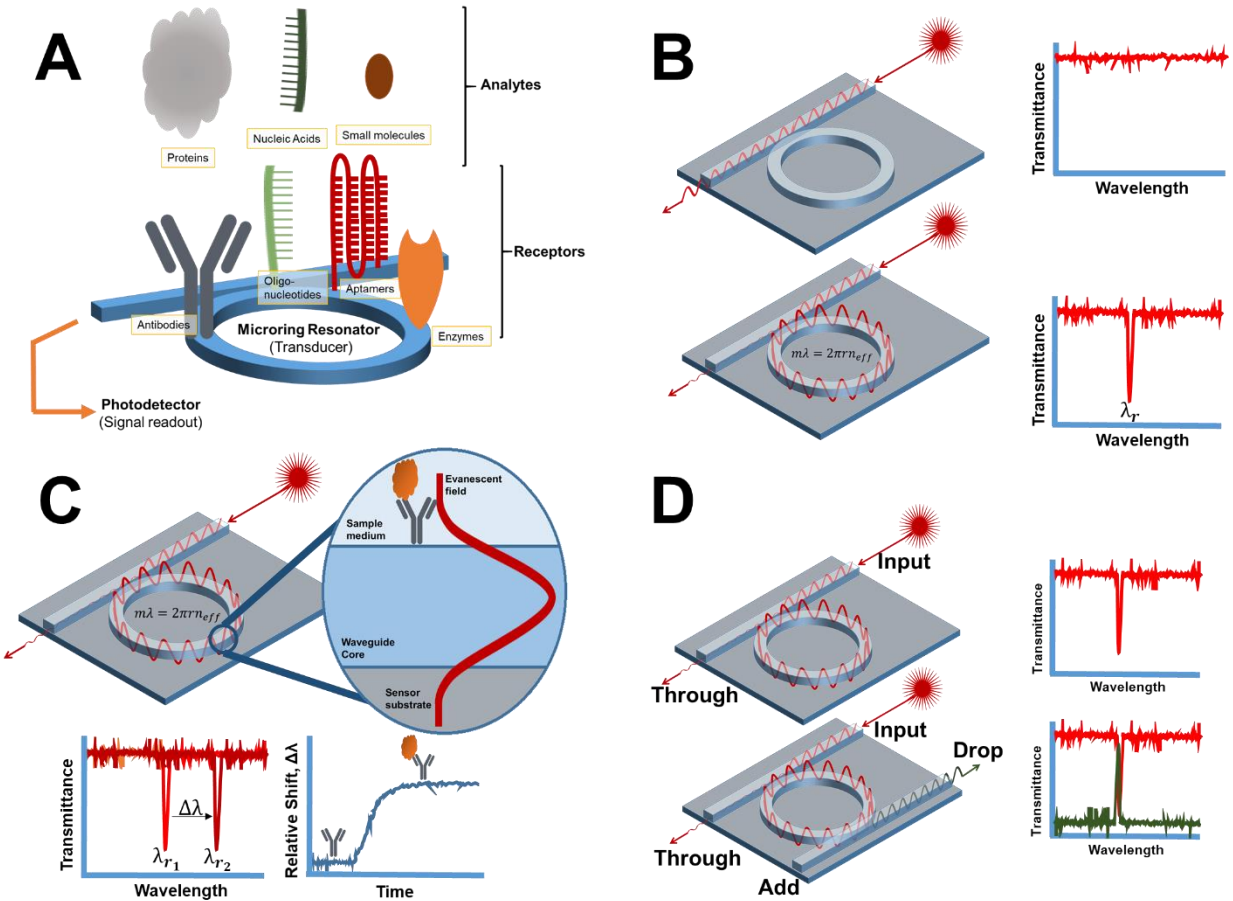


Figure 1-1. Schematics of microring resonators as bioanalytical devices and working principle. A) Schematic representation of the elements constituting a microring biosensor device: analytes, biorecognition elements, transducer, and signal readout. B) Drop in the transmitted light intensity at the wavelengths that resonate in the microring cavity. C) Evanescent field sensing the boundaries of the microring and resonant shift when analytes bind. D) Main configurations of ring resonators: all-pass filters and add-drop filters.

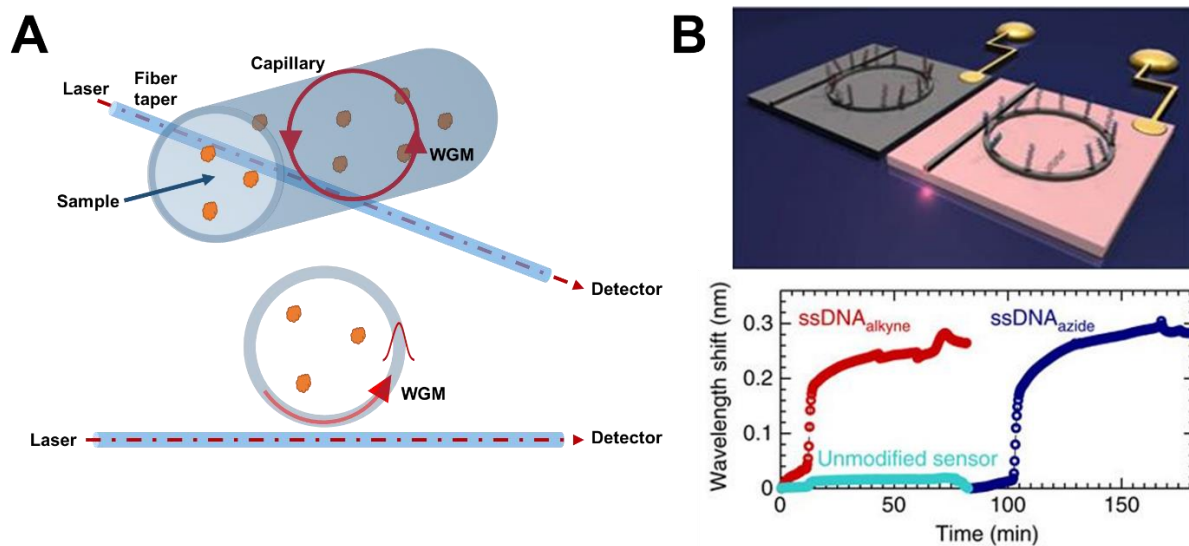


Figure 1-2. Innovative configurations of ring resonators to incorporate other functionalities. A) Cross-section view of an Optofluidic Ring Resonator sensor. The WGM is excited by an optical fiber taper in contact with the OFRR. The evanescent field of the WGM penetrates the polymer layer, making it sensitive to absorbed molecules. Adapted from ⁴⁹ Copyright 2013 Elsevier Ltd. B) Selective electrografting of a pair of optical ring resonator sensors within the same microfluidic chamber. Microrings sensors are subjected to electrical fields for the selective functionalization via electrochemical reactions. Adapted from ¹⁸ Copyright 2016, Springer Nature.

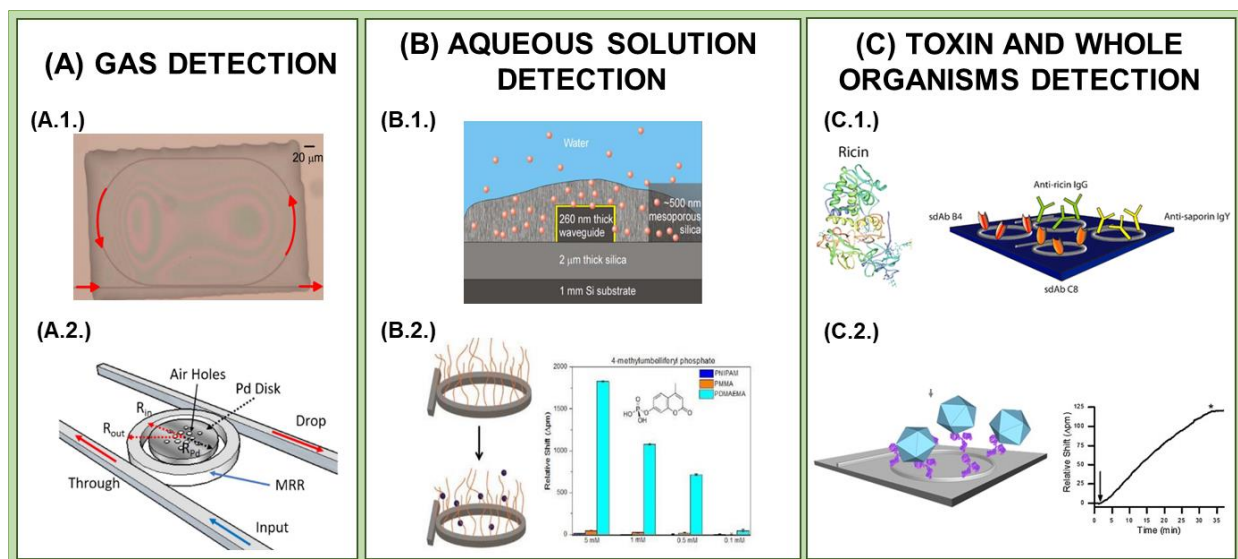


Figure 1-3: Applications of microring resonators in environmental monitoring. Examples in:

Gas detection: A.1. Coated SiN microring resonator with polymeric film for the detection of organophosphorus simulants²³. Reprinted from ²³ Copyright 2014 Optical Society of America.

A.2. Schematic architecture of the hydrogen sensing device with inner Pd disk ²⁴. Reprinted from ²⁴ Copyright 2017 Optical Society of America.

Aqueous molecule detection: B.1. Tetrasulfide-functionalized mesoporous silica film over SOI microring for heavy metal ions²⁶. Reprinted from ²⁶ Copyright 2015 Optical Society of America.

B.2. Selective partitioning of organic molecules in polymer brush leading to gearselective enhance recognition ²⁷. Reprinted from ²⁷ Copyright 2017 WILEY-VCH Verlag GmbH & Co.

Biological toxins and whole microorganisms: C.1. Microrings functionalized with single domain antibodies for the label-free recognition of ricin in buffer samples ²⁹. Adapted with permission from ²⁹ Copyright 2013 American Chemical Society. **C.2.** Microrings functionalized with antibodies for the label free recognition of Bean pod mottle virus in buffer and leaf extract samples ³¹. Adapted with permission from ³¹ Copyright 2012 Elsevier B.V.

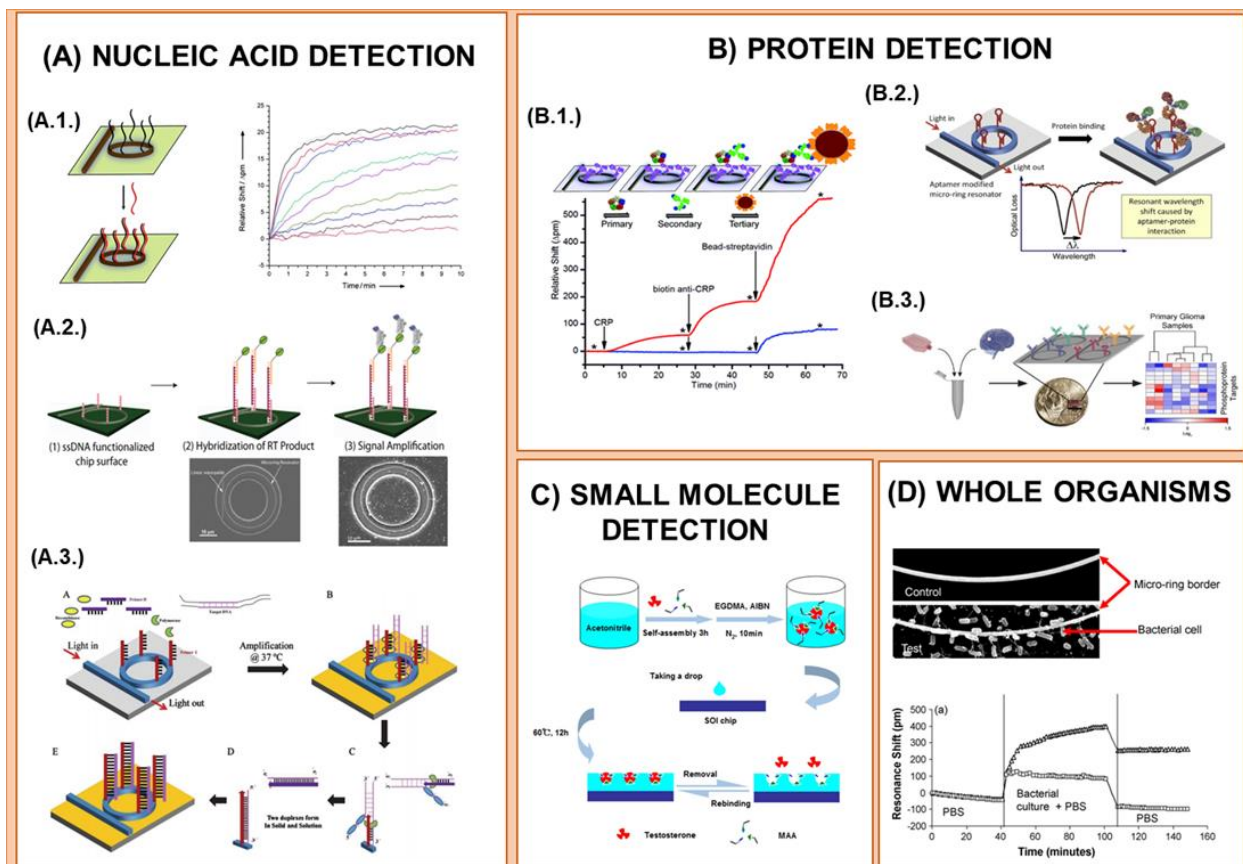


Figure 1-4. Applications of microring resonators in clinical analysis. Examples in:

Nucleic acid detection: **A.1.** Direct detection of miRNA without labeling. Quantification based on the slope of the binding curve³². Adapted with permission from ³² Copyright 2010 John Wiley and Sons. **A.2.** Detection of miRNA using a secondary signal amplification with biotin-streptavidin³⁹. Adapted with permission from ³⁹ Copyright 2016 American Chemical Society. **A.3.** Schematic representation of the principle of Isothermal Amplification/Detection⁸⁵. Reprinted with permission from ⁸⁵ Copyright 2014 Elsevier B.V.

Protein detection: **B.1.:** Detection of protein biomarkers using a secondary signal amplification with streptavidin beads⁴⁰. Adapted from ⁴⁰ with permission of The Royal Society of Chemistry. **B.2.** Label-free detection of IgE using microrings functionalized with aptamers⁴⁷. Reprinted with permission from ⁴⁷ Copyright 2012 Elsevier B.V. **B.3.** Direct multiplex detection of phosphoproteins using from cell and glioma tissue lysates¹⁴. Adapted with permission from ¹⁴ Copyright 2015 American Chemical Society.

C. Small biomolecules: Schematic for preparation molecularly imprinted polymers on the surface of chip⁴⁸. Reprinted with permission from ⁴⁸.

D. Whole microorganisms: Test and control micro-rings on a resonator chip, showing specific bacterial binding⁵⁰. Adapted with permission from ⁵⁰ Copyright 2007 Elsevier B.V.

TABLES

Table 1-1. Recent advances in microring resonators for environmental analysis.

Analyte	Detection strategy	Matrix	LOD	Ref
DMMP, organophosphorous simulant	A chemoselective coating that changes absorption spectra of MRR	Air	2 ppb	23
Hydrogen	Palladium disk inserted inside of microring cavity	Air	11.038 nm/% H ₂	24
Mercury; lead	Mesoporous silicate matrix	Water	1 ppm	26
DMMP	Selective recognition of the targeted DMMP molecule by specifically modified proteins immobilized on photonic structures	Air	6.8 ppb	25
4-methylumbelli-feryl phosphate, a simulant for highly toxic organophosphates	Selective partitioning of organophosphorus compounds in polymer brush grown on microrings	Buffer	0.1 mM	27
Aflatoxin M1	Aptamer and Fab recognition	Buffer	5 nM 1.58 nM	28
Ricin	Single Domain antibodies	PBST- BSA buffer	200 pM	29
Aurelia Aurantia Lectin and Sambucus Nigra Lectin	Surface functionalization with glycan receptors	Buffer	7 pM and 86 pM	30
<i>Bean pod mottle virus</i> Virus	Antibodies against the virus	Leaf extract dilutions	10 ng/ml	31

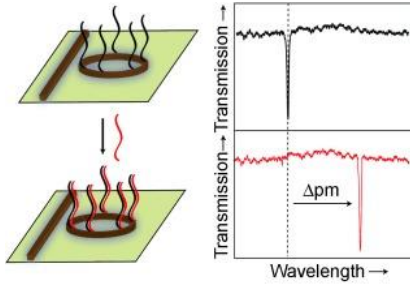
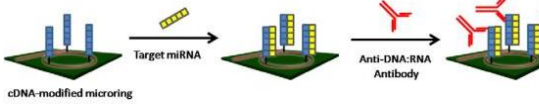
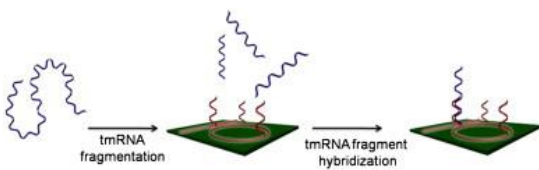
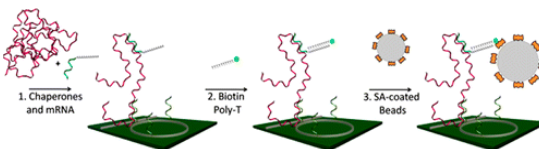
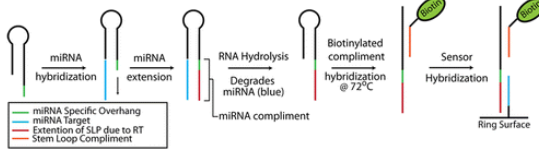
Table 1-2. Recent advances in microring resonators for clinical analysis.

Analyte	Detection strategy	Matrix	LOD	Ref
Insertion sequences of Mycobacterium tuberculosis H37Rv	Recombinase Polymerase Isothermal amplification and ring complementary hybridization	Extracted DNA from sputum samples	1 fg, 10 fg genomic DNA	36
9-plex miRNA panel	Asymmetric PCR and ring complementary hybridization	Extracted RNA from cells and tissue biopsies	2 pM	37
12-plex (Phospho)proteins panel	Antibody capture probe and signal amplification with an enzymatic turnover of precipitate on the surface	Brain tissue and cell lysates	0.6 pM IgG	14
7-plex cytokine panel	Antibody capture probe and signal amplification with an enzymatic turnover of precipitate on the surface	Mononuclear cell secretion	0.5-65 pg/ml	45
Viral glycoproteins (Ebola, Marburg virus, dengue)	Antibody capture probe and signal amplification with streptavidin beads	Blood and Saliva	1.6-39 ng/ml	46
Thrombin	An aptamer that binds thrombin without further amplification	Buffer	50 ng/ml	47
Testosterone	A layer of molecularly imprinted polymers for the recognition of testosterone	Water	48.7 pg/ml	48
Glucose	Capillary-based microring resonator	Buffer	0.035 mM	49
Escherichia coli	Microrings functionalized with monoclonal antibodies against the bacteria	Buffer	10 ⁵ CFU/ml	50
CD4+ and CD8+ lymphocytes	Antibodies immobilized in the inner surface of the capillary microring sensor	Buffer	200 cells/ μl	51

Table 1-3. Conventional techniques for the analysis of RNA molecules.

Technique	Working principle	Input	Advantages	Limitations	Ref
RT-qPCR	Reverse transcription into cDNA and amplification of DNA by PCR with fluorescent detection of the products.	ng	Sensitive, specific, gold standard for quantification	No multiplexable, only for known transcripts	86,87
Microarray	RNA binds to complementary probes that are spotted in surface, the detection is by fluorescence measurements.	μg	High throughput, relatively inexpensive	Cross reactivity between similar sequences, no absolute quantification	69
RNA sequencing	Reverse transcription into cDNA and massively parallel sequence. New generation technologies directly from RNA.	μg	Discovery of new transcripts, high throughput	Complicated bioinformatic processing, relative quantification	88

Table 1-4. Previous RNA detection protocols developed in the Bailey lab using microring resonators.

RNA type	Strategy	LOD Input	Mult	Figure of merit	Ref
miRNA	Steepness of the slope depending on the concentration. Binding to complementary oligonucleotide DNA probes on the surface	2 nM 75 μ l (150 fmol)	4		87
miRNA	Secondary amplification with antibody that recognizes DNA:RNA hybrids.	10 pM 35 μ l (350 amol)	4		80
tmRNA	Fragmentation of tmRNA molecules and steepness of the slope for quantitation. Binding to complementary probe.	524 pM 100 μ l (53 fmol) (320 ng tmRNA)	2		81
mRNA	Used of biotinylated chaperones and streptavidin coated beads to increase the signal and avoid secondary structure.	2.5 pM 200 μ l (512 amol) (20 μ g RNA)	2		89
miRNA	Secondary amplification with biotinylated sequences that bind the miRNAs that are bound to the capture probes.	1 nM 300 μ l (0.6 fmol)	7		39

Reprinted with permission from (ordered by row): (45) Copyright 2010 John Wiley and Sons, (41) Copyright 2011 American Chemical Society, (43) Copyright 2012 Elsevier B.V., (46) Copyright 2012 American Chemical Society, (42) Copyright 2016 American Chemical Society.

BIBLIOGRAPHY

- (1) Clark, L. C.; Lyons, C. Electrode Systems for Continuous Monitoring in Cardiovascular Surgery. *Ann. N. Y. Acad. Sci.* **1962**, *102* (1), 29–45.
- (2) Turner, A. P. F. Biosensors: Sense and Sensibility. *Chem. Soc. Rev.* **2013**, *42* (8), 3184.
- (3) Zourob, M. *Recognition Receptors in Biosensors*; Springer, 2010.
- (4) Liébana, S.; Drago, G. A. Bioconjugation and Stabilisation of Biomolecules in Biosensors. *Essays Biochem.* **2016**, *60* (1), 59–68.
- (5) Cooper, M. A. Label-Free Screening of Bio-Molecular Interactions. *Anal. Bioanal. Chem.* **2003**, *377* (5), 834–842.
- (6) Schuck, P.; Zhao, H. The Role of Mass Transport Limitation and Surface Heterogeneity in the Biophysical Characterization of Macromolecular Binding Processes by SPR Biosensing. *Methods Mol. Biol.* **2010**, *627*, 15–54.
- (7) Rusling, J. F.; Kumar, C. V.; Gutkind, J. S.; Patel, V. Measurement of Biomarker Proteins for Point-of-Care Early Detection and Monitoring of Cancer. *Analyst* **2010**, *135* (10), 2496.
- (8) Homola, J.; Piliarik, M. Surface Plasmon Resonance (SPR) Sensors. *Springer Ser Chem Sens Biosens* **2006**, *4*, 45–67.
- (9) Campbell, D. P. Interferometric Biosensors. In *Principles of Bacterial Detection: Biosensors, Recognition Receptors and Microsystems*; Springer New York: New York, NY, 2008; pp 169–211.
- (10) Vollmer, F.; Arnold, S. Whispering-Gallery-Mode Biosensing: Label-Free Detection down to Single Molecules. *Nat. Methods* **2008**, *5* (7), 591–596.

- (11) Damborsky, P.; vitel, J.; Katrlík, J. Optical Biosensors. *Essays Biochem.* **2016**, *60* (1), 91–100.
- (12) Wan, S.; Niu, R.; Ren, H.-L.; Zou, C.-L.; Guo, G.-C.; Dong, C.-H. Experimental Demonstration of Dissipative Sensing in a Self-Interference Microring Resonator. **2018**.
- (13) Li, B.-B.; Clements, W. R.; Yu, X.-C.; Shi, K.; Gong, Q.; Xiao, Y.-F. Single Nanoparticle Detection Using Split-Mode Microcavity Raman Lasers. *Proc. Natl. Acad. Sci. U. S. A.* **2014**, *111* (41), 14657–14662.
- (14) Wade, J. H.; Alsop, A. T.; Vertin, N. R.; Yang, H.; Johnson, M. D.; Bailey, R. C. Rapid, Multiplexed Phosphoprotein Profiling Using Silicon Photonic Sensor Arrays. *ACS Cent. Sci.* **2015**, *1* (7), 374–382.
- (15) Zhang, C.; Zou, C.-L.; Zhao, Y.; Dong, C.-H.; Wei, C.; Wang, H.; Liu, Y.; Guo, G.-C.; Yao, J.; Zhao, Y. S. Organic Printed Photonics: From Microring Lasers to Integrated Circuits. *Sci. Adv.* **2015**, *1* (8), e1500257.
- (16) Werquin, S.; Hoste, J.-W.; Martens, D.; Claes, T.; Bienstman, P. Silicon Ring Resonator-Based Biochips. In *Computational Photonic Sensors*; Springer International Publishing: Cham, 2019; pp 385–421.
- (17) Fan, X.; Sun, Y.; Suter, J. D.; Lee, W.; Wu, C. S.; Li, H. Optofluidic Ring Resonator Lasers: Principles and Applications. *2011 IEEE Winter Top. WTM 2011* **2011**, *1* (D), 97–98.
- (18) Juan-Colás, J.; Parkin, A.; Dunn, K. E.; Scullion, M. G.; Krauss, T. F.; Johnson, S. D. The Electrophotonic Silicon Biosensor. *Nat. Commun.* **2016**, *7*, 1–7.
- (19) Genalyte <https://www.genalyte.com/> (accessed May 7, 2019).
- (20) Miyara, M.; Charuel, J.-L.; Mudumba, S.; Wu, A.; Ghillani-Dalbin, P.; Amoura, Z.; Burlingame, R. W.; Musset, L. Detection in Whole Blood of Autoantibodies for the Diagnosis of Connective Tissue Diseases in near Patient Testing Condition. *PLoS One* **2018**, *13* (8), e0202736.

- (21) Mudumba, S.; de Alba, S.; Romero, R.; Cherwien, C.; Wu, A.; Wang, J.; Gleeson, M. A.; Iqbal, M.; Burlingame, R. W. Photonic Ring Resonance Is a Versatile Platform for Performing Multiplex Immunoassays in Real Time. *J. Immunol. Methods* **2017**, *448*, 34–43.
- (22) Gavela, A. F.; García, D. G.; Ramirez, J. C.; Lechuga, L. M. Last Advances in Silicon-Based Optical Biosensors. *Sensors (Switzerland)* **2016**, *16* (3), 1–15.
- (23) Stievater, T. H.; Pruessner, M. W.; Park, D.; Rabinovich, W. S.; McGill, R. A.; Kozak, D. a; Furstenberg, R.; Holmstrom, S. A.; Khurgin, J. B. Trace Gas Absorption Spectroscopy Using Functionalized Microring Resonators. *Opt. Lett.* **2014**, *39* (4), 969–972.
- (24) Cicek, K.; Eryürek, M.; Kiraz, A. Single-Slot Hybrid Microring Resonator Hydrogen Sensor. *J. Opt. Soc. Am. B* **2017**, *34* (7), 1465.
- (25) Bonnot, K.; Cuesta-Soto, F.; Rodrigo, M.; Varriale, A.; Sanchez, N.; D’Auria, S.; Spitzer, D.; Lopez-Royo, F. Biophotonic Ring Resonator for Ultrasensitive Detection of DMMP as a Simulant for Organophosphorus Agents. *Anal. Chem.* **2014**, *86* (10), 5125–5130.
- (26) Borjian, S.; Saunders, J.; Wu, X.; Crudden, C. M.; Loock, H.-P.; Danxia-Xu, X. Aqueous Lead and Mercury Detection Using Mesoporous Silicate Coated Silicon-on-Insulator Ring Resonators. In *Imaging and Applied Optics 2015*; OSA: Washington, D.C., 2015; p AIM2D.4.
- (27) Stanton, A. L. D.; Serrano, K. A.; Braun, P. V.; Bailey, R. C. Polymer Brush-Modified Microring Resonators for Partition-Enhanced Small Molecule Chemical Detection. *ChemistrySelect* **2017**, *2* (4), 1521–1524.
- (28) Chalyan, T.; Pasquardini, L.; Gandolfi, D.; Guider, R.; Samusenko, A.; Zanetti, M.; Pucker, G.; Pederzolini, C.; Pavesi, L. Aptamer- and Fab’- Functionalized Microring Resonators for Aflatoxin M1 Detection. *IEEE J. Sel. Top. Quantum Electron.* **2016**, *23* (c), 1–1.
- (29) Shia, W. W.; Bailey, R. C. Single Domain Antibodies for the Detection of Ricin Using Silicon Photonic Microring Resonator Arrays. *Anal. Chem.* **2013**, *85* (2), 805–810.

- (30) Ghasemi, F.; Hosseini, E. S.; Song, X.; Gottfried, D. S.; Chamanzar, M.; Raeiszadeh, M.; Cummings, R. D.; Eftekhari, A. A.; Adibi, A. Multiplexed Detection of Lectins Using Integrated Glycan-Coated Microring Resonators. *Biosens. Bioelectron.* **2016**, *80*, 682–690.
- (31) McClellan, M. S.; Domier, L. L.; Bailey, R. C. Label-Free Virus Detection Using Silicon Photonic Microring Resonators. *Biosens. Bioelectron.* **2012**, *31* (1), 388–392.
- (32) Qavi, A. J.; Bailey, R. C. Multiplexed Detection and Label-Free Quantitation of MicroRNAs Using Arrays of Silicon Photonic Microring Resonators. *Angew. Chemie Int. Ed.* **2010**, *49* (27), 4608–4611.
- (33) Suter, J. D.; White, I. M.; Zhu, H.; Shi, H.; Caldwell, C. W.; Fan, X. Label-Free Quantitative DNA Detection Using the Liquid Core Optical Ring Resonator. *Biosens. Bioelectron.* **2008**, *23* (7), 1003–1009.
- (34) Lo, S. M.; Hu, S.; Gaur, G.; Kostoulas, Y.; Weiss, S. M.; Fauchet, P. M. Photonic Crystal Microring Resonator for Label-Free Biosensing. *Opt. Express* **2017**, *25* (6), 7046.
- (35) Shin, Y.; Perera, A. P.; Park, M. K. Label-Free DNA Sensor for Detection of Bladder Cancer Biomarkers in Urine. *Sensors Actuators B Chem.* **2013**, *178*, 200–206.
- (36) Liu, Q.; Lim, B. K. L.; Lim, S. Y.; Tang, W. Y.; Gu, Z.; Chung, J.; Park, M. K.; Barkham, T. Label-Free, Real-Time and Multiplex Detection of Mycobacterium Tuberculosis Based on Silicon Photonic Microring Sensors and Asymmetric Isothermal Amplification Technique (SPMS-AIA). *Sensors Actuators B Chem.* **2018**, *255*, 1595–1603.
- (37) Graybill, R. M.; Cardenosa-Rubio, M. C.; Yang, H.; Johnson, M. D.; Bailey, R. C. Multiplexed MicroRNA Expression Profiling by Combined Asymmetric PCR and Label-Free Detection Using Silicon Photonic Sensor Arrays. *Anal. Methods* **2018**, *10* (14), 1618–1623.
- (38) Cardenosa-Rubio, M. C.; Graybill, R. M.; Bailey, R. C. Combining Asymmetric PCR-Based Enzymatic Amplification with Silicon Photonic Microring Resonators for the Detection of LncRNAs from Low Input Human RNA Samples. *Analyst* **2018**, *143* (5), 1210–1216.

- (39) Graybill, R. M.; Para, C. S.; Bailey, R. C. PCR-Free, Multiplexed Expression Profiling of MicroRNAs Using Silicon Photonic Microring Resonators. *Anal. Chem.* **2016**, *88* (21), 10347–10351.
- (40) Luchansky, M. S.; Washburn, A. L.; McClellan, M. S.; Bailey, R. C. Sensitive On-Chip Detection of a Protein Biomarker in Human Serum and Plasma over an Extended Dynamic Range Using Silicon Photonic Microring Resonators and Sub-Micron Beads. *Lab Chip* **2011**, *11* (12), 2042–2044.
- (41) Washburn, A. L.; Luchansky, M. S.; Bowman, A. L.; Bailey, R. C. Quantitative, Label-Free Detection of Five Protein Biomarkers Using Multiplexed Arrays of Silicon Photonic Microring Resonators. *Anal. Chem.* **2010**, *82* (1), 69–72.
- (42) Luchansky, M. S.; Bailey, R. C. Rapid, Multiparameter Profiling of Cellular Secretion Using Silicon Photonic Microring Resonator Arrays. *J. Am. Chem. Soc.* **2011**, *133* (50), 20500–20506.
- (43) Washburn, A. L.; Shia, W. W.; Lenkeit, K. A.; Lee, S.-H.; Bailey, R. C. Multiplexed Cancer Biomarker Detection Using Chip-Integrated Silicon Photonic Sensor Arrays. *Analyst* **2016**, *141* (18), 5358–5365.
- (44) Kindt, J. T.; Luchansky, M. S.; Qavi, A. J.; Lee, S.-H.; Bailey, R. C. Subpicogram Per Milliliter Detection of Interleukins Using Silicon Photonic Microring Resonators and an Enzymatic Signal Enhancement Strategy. *Anal. Chem.* **2013**, *85* (22), 10653–10657.
- (45) Robison, H. M.; Escalante, P.; Valera, E.; Erskine, C. L.; Auvil, L.; Sasieta, H. C.; Bushell, C.; Welge, M.; Bailey, R. C. Precision Immunoprofiling to Reveal Diagnostic Signatures for Latent Tuberculosis Infection and Reactivation Risk Stratification. *Integr. Biol.* **2019**, *11* (1), 16–25.
- (46) Estrada, I. A.; Burlingame, R. W.; Wang, A. P.; Chawla, K.; Grove, T.; Wang, J.; Southern, S. O.; Iqbal, M.; Gunn, L. C.; Gleeson, M. A. Multiplex Detection of Pathogen Biomarkers in Human Blood, Serum, and Saliva Using Silicon Photonic Microring Resonators; Southern, S. O., Ed.; International Society for Optics and Photonics, 2015; Vol. 9490, p

94900E.

- (47) Park, M. K.; Kee, J. S.; Quah, J. Y.; Netto, V.; Song, J.; Fang, Q.; La Fosse, E. M.; Lo, G.-Q. Label-Free Aptamer Sensor Based on Silicon Microring Resonators. *Sensors Actuators B Chem.* **2013**, *176*, 552–559.
- (48) Chen, Y.; Liu, Y.; Shen, X.; Chang, Z.; Tang, L.; Dong, W.-F.; Li, M.; He, J.-J.; Chen, Y.; Liu, Y.; et al. Ultrasensitive Detection of Testosterone Using Microring Resonator with Molecularly Imprinted Polymers. *Sensors* **2015**, *15* (12), 31558–31565.
- (49) Luo, Y.; Chen, X.; Xu, M.; Chen, Z.; Fan, X. Optofluidic Glucose Detection by Capillary-Based Ring Resonators. *Opt. Laser Technol.* **2014**.
- (50) Ramachandran, A.; Wang, S.; Clarke, J.; Ja, S. J.; Goad, D.; Wald, L.; Flood, E. M.; Knobbe, E.; Hryniewicz, J. V.; Chu, S. T.; et al. A Universal Biosensing Platform Based on Optical Micro-Ring Resonators. *Biosens. Bioelectron.* **2008**, *23* (7), 939–944.
- (51) Gohring, J. T.; Fan, X.; Gohring, J. T.; Fan, X. Label Free Detection of CD4+ and CD8+ T Cells Using the Optofluidic Ring Resonator. *Sensors* **2010**, *10* (6), 5798–5808.
- (52) Sunde, R. A. mRNA Transcripts as Molecular Biomarkers in Medicine and Nutrition. *J. Nutr. Biochem.* **2010**, *21* (8), 665–670.
- (53) Xi, X.; Li, T.; Huang, Y.; Sun, J.; Zhu, Y.; Yang, Y.; Lu, Z. J. RNA Biomarkers: Frontier of Precision Medicine for Cancer. *Non-coding RNA* **2017**, *3* (1).
- (54) Sparano, J. A.; Gray, R. J.; Makower, D. F.; Pritchard, K. I.; Albain, K. S.; Hayes, D. F.; Geyer, C. E.; Dees, E. C.; Perez, E. A.; Olson, J. A.; et al. Prospective Validation of a 21-Gene Expression Assay in Breast Cancer. *N. Engl. J. Med.* **2015**, *373* (21), 2005–2014.
- (55) Mattick, J. S.; Makunin, I. V. Non-Coding RNA. *Hum. Mol. Genet.* **2006**, *15* (suppl_1), R17–R29.
- (56) Huang, Y.; Shen, X. J.; Zou, Q.; Wang, S. P.; Tang, S. M.; Zhang, G. Z. Biological Functions of MicroRNAs: A Review. *J. Physiol. Biochem.* **2011**, *67* (1), 129–139.

- (57) Wang, J.; Chen, J.; Sen, S. MicroRNA as Biomarkers and Diagnostics. *J. Cell. Physiol.* **2016**, *231* (1), 25–30.
- (58) Kamal, M.; Mushtaq, G.; Greig, N. Current Update on Synopsis of MiRNA Dysregulation in Neurological Disorders. *CNS Neurol. Disord. - Drug Targets* **2015**, *14* (4), 492–501.
- (59) Zhou, S.; Jin, J.; Wang, J.; Zhang, Z.; Freedman, J. H.; Zheng, Y.; Cai, L. MiRNAs in Cardiovascular Diseases: Potential Biomarkers, Therapeutic Targets and Challenges. *Acta Pharmacol. Sin.* **2018**, *39* (7), 1073–1084.
- (60) Roberts, A. P. E.; Lewis, A. P.; Jopling, C. L. The Role of MicroRNAs in Viral Infection. *Prog. Mol. Biol. Transl. Sci.* **2011**, *102*, 101–139.
- (61) Gupta, R. a; Shah, N.; Wang, K. C.; Kim, J.; Horlings, H. M.; Wong, D. J.; Tsai, M.-C.; Hung, T.; Argani, P.; Rinn, J. L.; et al. Long Non-Coding RNA HOTAIR Reprograms Chromatin State to Promote Cancer Metastasis. *Nature* **2010**, *464* (7291), 1071–1076.
- (62) Rinn, J. L.; Chang, H. Y. Genome Regulation by Long Noncoding RNAs. *Annu. Rev. Biochem.* **2012**, *81* (1), 145–166.
- (63) Magistri, M.; Faghihi, M. A.; St Laurent, G.; Wahlestedt, C. Regulation of Chromatin Structure by Long Noncoding RNAs: Focus on Natural Antisense Transcripts. *Trends Genet.* **2012**, *28* (8), 389–396.
- (64) Qi, P.; Du, X. The Long Non-Coding RNAs, a New Cancer Diagnostic and Therapeutic Gold Mine. *Mod. Pathol.* **2013**, *26* (2), 155–165.
- (65) Chen, Z.; Wei, L.-L.; Shi, L.-Y.; Li, M.; Jiang, T.-T.; Chen, J.; Liu, C.-M.; Yang, S.; Tu, H.; Hu, Y.; et al. Screening and Identification of LncRNAs as Potential Biomarkers for Pulmonary Tuberculosis. *Sci. Reports 2017 71* **2017**, *7* (1), 16751.
- (66) Hobuß, L.; Bär, C.; Thum, T. Long Non-Coding RNAs: At the Heart of Cardiac Dysfunction? *Front. Physiol.* **2019**, *10*, 30.
- (67) Qureshi, I. A.; Mattick, J. S.; Mehler, M. F. Long Non-Coding RNAs in Nervous System

- Function and Disease. *Brain Res.* **2010**, *1338*, 20–35.
- (68) Git, A.; Dvinge, H.; Salmon-Divon, M.; Osborne, M.; Kutter, C.; Hadfield, J.; Bertone, P.; Caldas, C. Systematic Comparison of Microarray Profiling, Real-Time PCR, and next-Generation Sequencing Technologies for Measuring Differential MicroRNA Expression. *RNA* **2010**, *16* (5), 991–1006.
- (69) Schena, M.; Shalon, D.; Davis, R. W.; Brown, P. O. Quantitative Monitoring of Gene Expression Patterns with a Complementary DNA Microarray. *Science* **1995**, *270* (5235), 467–470.
- (70) Sealson, S. C.; Chu, T. T. RNA and DNA Microarrays; Humana Press, Totowa, NJ, 2011; pp 3–34.
- (71) Cieřlik, M.; Chinnaiyan, A. M. Cancer Transcriptome Profiling at the Juncture of Clinical Translation. *Nat. Rev. Genet.* **2017**, *19* (2), 93–109.
- (72) Stenton, S. L.; Prokisch, H. The Clinical Application of RNA Sequencing in Genetic Diagnosis of Mendelian Disorders. *Adv. Mol. Pathol.* **2018**, *1* (1), 27–36.
- (73) Sweeney, B. A.; Petrov, A. I.; Burkov, B.; Finn, R. D.; Bateman, A.; Szymanski, M.; Karlowski, W. M.; Gorodkin, J.; Seemann, S. E.; Cannone, J. J.; et al. RNAcentral: A Hub of Information for Non-Coding RNA Sequences. *Nucleic Acids Res.* **2019**, *47* (D1), D221–D229.
- (74) Zhao, Y.; Li, H.; Fang, S.; Kang, Y.; wu, W.; Hao, Y.; Li, Z.; Bu, D.; Sun, N.; Zhang, M. Q.; et al. NONCODE 2016: An Informative and Valuable Data Source of Long Non-Coding RNAs. *Nucleic Acids Res.* **2016**, *44* (D1), D203–D208.
- (75) Carrascosa, L. G.; Huertas, C. S.; Lechuga, L. M. Prospects of Optical Biosensors for Emerging Label-Free RNA Analysis. *TrAC Trends Anal. Chem.* **2016**, *80*, 177–189.
- (76) Huertas, C. S.; Carrascosa, L. G.; Bonnal, S.; Valcárcel, J.; Lechuga, L. M. Quantitative Evaluation of Alternatively Spliced mRNA Isoforms by Label-Free Real-Time Plasmonic Sensing. *Biosens. Bioelectron.* **2016**, *78*, 118–125.

- (77) Su, J.; Wang, D.; Nörbel, L.; Shen, J.; Zhao, Z.; Dou, Y.; Peng, T.; Shi, J.; Mathur, S.; Fan, C.; et al. Multicolor Gold–Silver Nano-Mushrooms as Ready-to-Use SERS Probes for Ultrasensitive and Multiplex DNA/MiRNA Detection. *Anal. Chem.* **2017**, *89* (4), 2531–2538.
- (78) Qiu, X.; Hildebrandt, N. Rapid and Multiplexed MicroRNA Diagnostic Assay Using Quantum Dot-Based Förster Resonance Energy Transfer. *ACS Nano* **2015**, *9* (8), 8449–8457.
- (79) Hamidi-Asl, E.; Palchetti, I.; Hasheminejad, E.; Mascini, M. A Review on the Electrochemical Biosensors for Determination of MicroRNAs. *Talanta* **2013**, *115*, 74–83.
- (80) Qavi, A. J.; Kindt, J. T.; Gleeson, M. A.; Bailey, R. C. Anti-DNA:RNA Antibodies and Silicon Photonic Microring Resonators: Increased Sensitivity for Multiplexed MicroRNA Detection. *Anal. Chem.* **2011**, *83*, 5949–5956.
- (81) Scheler, O.; Kindt, J. T.; Qavi, A. J.; Kaplinski, L.; Glynn, B.; Barry, T.; Kurg, A.; Bailey, R. C. Label-Free, Multiplexed Detection of Bacterial TmRNA Using Silicon Photonic Microring Resonators. *Biosens. Bioelectron.* **2012**, *36* (1), 56–61.
- (82) Kindt, J. T.; Bailey, R. C. Chaperone Probes and Bead-Based Enhancement To Improve the Direct Detection of mRNA Using Silicon Photonic Sensor Arrays. *Anal. Chem.* **2012**, *84* (18), 8067–8074.
- (83) Sanchez, J. A.; Pierce, K. E.; Rice, J. E.; Wangh, L. J. Linear-After-The-Exponential (LATE)–PCR: An Advanced Method of Asymmetric PCR and Its Uses in Quantitative Real-Time Analysis. *Proc. Natl. Acad. Sci.* **2004**, *101* (7), 1933–1938.
- (84) Mordan, E. H.; Wade, J. H.; Wiersma, Z. S. B.; Pearce, E.; Pangburn, T. O.; deGroot, A. W.; Meunier, D. M.; Bailey, R. C. Silicon Photonic Microring Resonator Arrays for Mass Concentration Detection of Polymers in Isocratic Separations. *Anal. Chem.* **2019**, *91* (1), 1011–1018.
- (85) Shin, Y.; Soo, R. A.; Yoon, J.; Promoda Perera, A.; Yoon, Y. J.; Park, M. K. Rapid and Label-Free Amplification and Detection Assay for Genotyping of Cancer Biomarker.

Biosens. Bioelectron. **2015**.

- (86) Raymond, C. K.; Roberts, B. S.; Garrett-Engele, P.; Lim, L. P.; Johnson, J. M. Simple, Quantitative Primer-Extension PCR Assay for Direct Monitoring of MicroRNAs and Short-Interfering RNAs. *RNA* **2005**, *11* (11), 1737–1744.
- (87) Qavi, A. J.; Bailey, R. C. Multiplexed Detection and Label-Free Quantitation of MicroRNAs Using Arrays of Silicon Photonic Microring Resonators. *Angew. Chemie Int. Ed.* **2010**, *49* (27), 4608–4611.
- (88) Stenton, S. L.; Prokisch, H. The Clinical Application of RNA Sequencing in Genetic Diagnosis of Mendelian Disorders. **2018**.
- (89) Kindt, J. T.; Bailey, R. C. Chaperone Probes and Bead-Based Enhancement to Improve the Direct Detection of mRNA Using Silicon Photonic Sensor Arrays. *Anal. Chem.* **2012**, *84* (18), 8067–8074.

CHAPTER II

Multiplexed microRNA expression profiling by combined asymmetric PCR and label-free detection using silicon photonic sensor arrays

Acknowledgements:

This chapter has been adapted from the research article “Multiplexed microRNA expression profiling by combined asymmetric PCR and label-free detection using silicon photonic sensor arrays” (Graybill, R.M.; Cardenosa-Rubio, M.C.; Yang, H.; Johnson, M.D.; Bailey, R.C., *Analytical Methods* **2018**, *10*, 1618-1623). The article has been reproduced here with permission from the Royal Society of Chemistry © 2018[†].

Richard Graybill conceived the presented idea of combining amplification by asymmetric PCR with microring resonators. My contribution in this research corresponds to the design and optimization of the experiments, the realization of the calibration curves, analysis of the results and measurement in the patient samples. I also contributed to the writing of the manuscript and minor changes from the observations of the reviewers.

The authors gratefully acknowledge financial support from the National Cancer Institute of the National Institutes of Health through Grant CA177462. R. M. G. acknowledges support from the National Cancer Institute Alliance for Nanotechnology in Cancer “Midwest Cancer Nanotechnology Training Center” Grant R25 CA154015A. M. C. R. acknowledges support from la Caixa Banking Foundation Fellowship. We also appreciate the support provided through UIUC's Institute for Genomic Biology.

[†] <http://www.rsc.org/journals-books-databases/journal-authors-reviewers/licences-copyright-permissions/>

Abstract

Analysis methods based upon the quantitative, real-time polymerase chain reaction are extremely powerful; however, they face intrinsic limitations in terms of target multiplexing. In contrast, silicon photonic microring resonators represent a modularly multiplexable sensor array technology that is well-suited to the analysis of targeted biomarker panels. In this manuscript we employ an asymmetric polymerase chain reaction approach to selectively amplify copies of cDNAs generated from targeted miRNAs before being multiplexed, and the label-free quantitation through hybridization to microring resonator arrays pre-functionalized with capture sequences. This method, which shows applicability to low input amounts and a large dynamic range, was demonstrated for the simultaneous detection of eight microRNA targets from twenty primary brain tumor samples with expression profiles in good agreement with literature precedent.

1. Introduction

It is well accepted that multiplexed diagnostics can provide a more holistic view of biomolecular dynamics that supports an improved understanding of disease onset and progression.^{1,2} One of the important potential outcomes of multiplexed analysis is a deeper understanding of the role of microRNA (miRNA) molecules and the interconnected networks through which they help regulate protein expression.³ Dysregulation of miRNA levels leads to altered protein expression, which has profound implications in a wide range of pathophysiological conditions.⁴⁻⁸ An increasing appreciation for plasticity and redundancy within miRNA regulatory networks motivates the development of methods to perform multiplexed measurements to simultaneously profile multiple miRNA expression levels from sample-limited clinical specimens.^{9,10}

Unfortunately, technological gaps exist that have hindered the translation of miRNA-based diagnostics to the clinic.^{10,11} Specifically, RT-qPCR methods, which are very sensitive, relatively rapid, and cost effective, (typically) only measure levels of one miRNA per assay. Microarrays, are well-suited for multiplexed analyses, but are typically slow, less sensitive, and more expensive. Next-generation sequencing allows global profiling and discovery of RNA signatures, including miRNAs; however, it requires complex processing steps and intensive bioinformatics to interpret sequencing reads. As a result, sequencing has yet to emerge as a standard diagnostic tool to guide clinical intervention. That said, previous efforts of sequencing and bioinformatic data reduction have identified panels of miRNAs

that are promising as sets of actionable biomarkers,¹² motivating the development of moderately multiplexable miRNA analysis technologies that can fill the present void by providing targeted detection of clinically relevant panels.

Silicon photonic microring resonators are surface-sensitive optical sensors that are intrinsically multiplexable on account of their fabrication *via* established semiconductor methods. These devices support optical resonances that are sensitive to local environment, and, when functionalized with appropriate capture agents, analyte binding-induced changes in local refractive index can be detected as shifts in resonance wavelength, as previously described.¹³ The sensors can be functionalized with different classes of receptors to afford selectivity towards different classes of biomolecular targets.^{14–19} Applied to the detection of miRNAs, these sensors have been operated in a label-free format,²⁰ as well in both antibody-,²¹ and enzyme-enhanced assays.²² While these studies demonstrated robust performance and multiplexing capacity, they suffered from insufficient limits of detection that required either large sample input or lengthy analysis times, both of which are restrictive for clinical miRNA profiling applications.

In this manuscript we exploit the advantages of both PCR (target-specific amplification) and microring resonators (multiplexed detection) to profile multiple miRNAs from clinically-relevant samples using a label-free, hybridization-based method. While others have successfully coupled solid phase PCR with optical biosensors,²³ we elected to move away from traditional PCR since it produces double stranded DNA products which are not amenable for hybridization based assays. Instead, asymmetric PCR (aPCR) was used to selectively produce single stranded DNA products by using an excess of one of the PCR primers.^{24,25} This combination greatly improves upon previous microring resonator-based miRNA detection assays and allows analyses from only nanograms of total RNA—an amount comparable with standard, single-plex PCR methods. aPCR was originally demonstrated for solution-phase DNA detection²⁴ and has also been combined with surface plasmon resonance (SPR) for detection.²⁶ For RNA analysis, aPCR has been applied to mRNAs using microarrays²⁷ and 16S rRNAs *via* a magnetic bead-based method.²⁸ Here, we utilize silicon photonic sensor arrays and report a new stem loop primer motif that firstly allows detection of miRNAs using a modified aPCR approach. We then demonstrate the ability to profile expression levels of eight miRNAs simultaneously from primary surgical glioma specimens.

2. Experimental

Materials

All nucleic acid sequences were purchased from Integrated DNA Technologies (IDT; Coralville, IA) and are listed in Table 2.1. The TaqMan® microRNA Reverse Transcription Kit and the Platinum® Multiplex PCR Master Mix were purchased from Thermo Fisher. All buffers and dilutions were prepared in nuclease-free ultrapure distilled water (Invitrogen). Phosphate-buffered saline (PBS) was obtained from Lonza and was used in the reconstitution of the DNA capture probes. For the functionalization of sensor chips, 3-(aminopropyl)-triethoxysilane (APTES) and bis(sulfosuccinimidyl)-suberate (BS3) were obtained from Thermo Fisher Scientific. For the hybridization steps, a high stringency hybridization buffer was made in 50 mL batches containing 15 mL of formamide (Fisher), 1 mL 10% sodium dodecyl sulfate (Fisher), 10 mL 20X saline-sodium phosphate buffer (Invitrogen), 6 mL 0.25 M ethylenediaminetetraacetic acid (Invitrogen) and 2.5 mL 50X Denhardt's solution (Invitrogen).

Instrumentation

Microring sensor arrays and measurement equipment were purchased from Genalyte, Inc. (San Diego, CA). Sensor arrays were fabricated using standard photolithography and etching techniques. The final sensor arrays are coated with a fluoropolymer coating, which is only removed from active microring sensor elements, and are diced so as to contain 132 individually-addressable microring resonator sensors. For hybridization experiments, sensor arrays are loaded into a cell formed by a Mylar gasket and Teflon lid that directs solutions into two defined flow chambers aligned with the sensor elements. Integrated pumps under software control automated all liquid handling steps.

Resonant wavelengths for each microring were determined by coupling a tunable laser source into an adjacent linear waveguide *via* on-chip grating couplers. The laser output was then swept through an appropriate spectral window and the light intensity at the end of the linear waveguide was used to determine the resonance wavelength. This process was serially repeated for each ring in the array, and the resultant shifts in resonance were recorded as a function of time.

The resonances supported by the microring resonator sensors meet the following mathematical condition:

$$m\lambda = 2\pi r n_{\text{eff}}$$

where m equals a non-zero integer, λ is the wavelength of propagating light supported by the microring resonator sensor, r is the microring radius, and n_{eff} is the effective refractive index sampled by the optical mode. Light is confined in the waveguide by total internal reflection resulting in an evanescent field extending only a short distance from the surface of the microring sensor. Biomolecular binding events within the region leads to a change in the resonant wavelength of the cavity, which is monitored by the optical scanning instrumentation. The binding of biomolecules results in a resonance shift to longer wavelengths: a positive shift that is listed in units of Δ picometers (Δpm).

Surface functionalization

Surface functionalization was performed using one of two protocols: manually spotting by hand or automated microspotting.

Manual spotting was used in validation experiments and for obtaining calibration curves. Prior to chip functionalization, chips were cleaned with a piranha solution (70% sulphuric acid/30% hydrogen peroxide) for 30 seconds at 60 °C. CAUTION: Piranha solution reacts vigorously with organics and should be handled with care. Then, the chips were rinsed with water and dried with nitrogen. Once dried, chips were immersed in acetone for 2 minutes, followed by the surface silanization with a 5% APTES solution (diluted in acetone) for 4 minutes. After silanization, the chips were immersed in acetone and isopropanol for 2 minutes each. All steps were completed with continued shaking. Chips were rinsed with water and nitrogen dried to complete the silanization process. Next, 20 μL of a freshly prepared BS3 solution (2.85 mg mL^{-1} in 2 mM acetic acid) was placed on the microring array for 3 minutes. BS3 served as the linker between the amine groups of the silanized surface and the amino-functionalized nucleic acid capture probes. After BS3 incubation, the chips were dried with nitrogen, and the final step consisted of spotting approximately 0.26 μM of 200 μM 5' amino functionalized DNA capture probes onto discrete microring sensors. The chips were then left to incubate for at least 4 hours in a humidity chamber.

Automated microspotting was used to create sensor arrays for the cross reactivity studies and clinical sample profiling. This procedure was similar to manual spotting conditions with the only differences being the use of a 1% APTES solution, a lower concentration of BS3 (1 mg mL^{-1}), and a lower concentration of the DNA capture probes ($100 \text{ }\mu\text{M}$).

Reverse transcription-asymmetric PCR amplification

Reverse transcription reactions were conducted using a TaqMan microRNA Reverse Transcription Kit. Each $15 \text{ }\mu\text{L}$ reaction volume contained $4.16 \text{ }\mu\text{L}$ of nuclease free water, $1.5 \text{ }\mu\text{L}$ of 10X RT buffer, $1 \text{ }\mu\text{L}$ of Multiscribe™ RT enzyme ($50 \text{ U }\mu\text{L}^{-1}$), $0.19 \text{ }\mu\text{L}$ of RNase inhibitor ($20 \text{ U }\mu\text{L}^{-1}$), $0.15 \text{ }\mu\text{L}$ dNTP mix (100 mM), $5 \text{ }\mu\text{L}$ of RNA sample (10 ng of RNA in the case of patient samples) and $3 \text{ }\mu\text{L}$ of the reverse transcription primer. The concentration of the stem loop primer was $20 \text{ }\mu\text{M}$ for all experiments, except for the data presented in **Figure 2-2** where $200 \text{ }\mu\text{M}$ was used. The thermal profile was completed following the manufacturer's protocol: $16 \text{ }^\circ\text{C}$ (30 min), $42 \text{ }^\circ\text{C}$ (30 min), and $85 \text{ }^\circ\text{C}$ (5 min).

Asymmetric PCR was performed using the Platinum Multiplex PCR Master Mix. Each $50 \text{ }\mu\text{L}$ reaction volume was composed of $14 \text{ }\mu\text{L}$ nuclease free water, $25 \text{ }\mu\text{L}$ of Platinum® Multiplex PCR Master Mix, $5 \text{ }\mu\text{L}$ of each primer and $1 \text{ }\mu\text{L}$ of the reversed transcription product. The concentration of the forward primer (the limiting primer) was $2 \text{ }\mu\text{M}$ while the concentration of the reverse primer was $200 \text{ }\mu\text{M}$. The reactions were incubated at $95 \text{ }^\circ\text{C}$ for 2 min , followed by cycles of $95 \text{ }^\circ\text{C}$ for 30 s , $56 \text{ }^\circ\text{C}$ for $1 \text{ min } 30 \text{ s}$, and $72 \text{ }^\circ\text{C}$ for 1 min .

Sample introduction and fluidic handling

For hybridization experiments, the $50 \text{ }\mu\text{L}$ PCR reaction volume was diluted with $350 \text{ }\mu\text{L}$ of hybridization buffer and then subjected to the fluidic handling recipe outlined in Table 2.2.

Data analysis

Data was analyzed with Origin Pro 9.0 and completed in three steps: (1) calculation of the hybridization response; (2) determination of $C(t)$ values; and (3) compilation of heat maps.

To calculate the hybridization response, sensor traces were first corrected for temperature and instrumental drift by using a series of reference sensors that were not in contact with the sample solution.

Resonance shifts from aPCR product hybridization were calculated by subtracting the baseline buffer signal (resonance shift) at 5 minutes from the post-hybridization response (22 minutes). The shift from off-target control sensors was then subtracted from the response from miRNA-specifically-functionalized sensors.

Threshold cycle [$C(t)$] values were determined by plotting the net resonance wavelength shifts *versus* the PCR cycle number for every target (**Figure 2-2**). $C(t)$ s were calculated in one of two ways: by either determining the point at which the second derivative of the logistic fit equaled zero (second derivative method), or the point at which 40% of the maximal signal was as the cycle number that achieved 40% of the maximum signal (linear thresholding). $C(t)$ values were found to be linear with input miRNA concentration for all targets (**Figure 2-4**).

To compare relative expression levels of multiple miRNAs from primary tumor samples, a heat map was produced by subtracting $C(t)$ values for each miRNA measured from the primary samples from a commercial “healthy” brain total RNA sample (Thermo Fisher). The resulting values are plotted in Table 2.4 using a log₂ scale. Positive values represent higher expression in tumor tissue and negative values represent lower expression in tumor tissue, relative to healthy.

Cross-reactivity experiments

To probe the specificity of the capture probes, reverse transcription followed by 20 cycles of asymmetric PCR was carried out using 200 nM dilutions of all eight target miRNAs. The resulting products (50 μ L) were diluted in 350 μ L of hybridization buffer and flowed across the surface following the recipe described in **Table 2-2**.

3. Results and discussion

The overall workflow for this analytical scheme is shown in **Figure 2-1**. After isolation of total RNA, uniquely-designed, sequence-specific stem loop primers were used to reverse transcribe (RT) miRNAs into cDNAs.²⁹ RT products were then amplified *via* asymmetric PCR to generate single-stranded targets that were flowed across microring resonator arrays for label-free, hybridization-based detection. PCR primers were designed such that the limiting primer targeted the microRNA-specific region of the RT product. The primer used in excess (100 \times) targeted a universal region common to each target-specific stem-loop probe. Importantly, the same excess primer could be used for the entire panel

of miRNA targets. As illustrated in **Figure 2-1**, dsDNA is produced until the limiting PCR primer is exhausted, after which point additional thermal cycles create ssDNAs by extending only from the remaining excess primer. After aPCR, the product was diluted into a high stringency hybridization buffer and flowed across a sensor array for label-free, hybridization-based detection. The transition from duplex to single-strand production is dependent upon target concentration and thus directly proportional to the initial concentration of the miRNA target in the sample. The concentration of single stranded DNA product after a defined number of cycles therefore also is directly proportional to the amount of miRNA in the initial solution. In this way, the combination of stem loop primers, aPCR, and silicon photonic microring resonators can be used to performed multiplexed miRNA expression profiling.

To validate this approach, primer sets, including target-specific stem-loop sequences, were designed for eight miRNAs (sequences provided in **Table 2-1**). Using synthetic miRNAs RT was first performed, followed by aPCR for defined numbers of thermal cycles. After aPCR, the resulting amplicon-containing solution was flowed across microring sensors presenting a capture sequence. **Figure 2-2A** shows the resonance shifts for the detection of a representative target (let-7f) across a range of input concentrations as a function of cycle number. Each of the concentration-dependent resonance shift data sets was fit with a logistic function for clarity. Higher concentrations of let-7f give observable resonance shifts at as few as 15 cycles with lower concentrations requiring larger numbers of cycles. That is to say that logistic functions for lower concentrations were shifted to higher cycle numbers. In this way, the onset of ssDNA production and microring hybridization response was dependent upon input miRNA concentration.

To enable quantitation of miRNA concentrations, we explored two different approaches to assign a numerical threshold cycle value associate with the hybridization response. This is analogous to $C(t)$ values from conventional RT-qPCR analysis,³⁰ and we have adopted the same naming convention. Our first approach involved assigning $C(t)$ as the value at which the second derivative of the logistic function equaled zero. A second approach involved determining the $C(t)$ value at which 40% of the maximal shift was observed *via* interpolation of the linear response region. The resulting calibration curves relating concentration to $C(t)$ values determined *via* both the 2nd derivative and linear thresholding methods for a representative target miRNA, let 7-f, are in good agreement, as shown in **Figure 2-2B**. Notably, both show dynamic ranges in excess of six orders of magnitude in target concentration. For the second derivative method, error bars come from the logistic fit parameter estimate variance. For the

linear thresholding approach, error bars were generated by propagating the error from measurements from the array of technical replicate sensors. Similar calibration curves were obtained for the other miRNA targets in the multiplexed panel (**Figure 2-4**).

Target specificity is obviously of high importance in miRNA analysis. In order to test specificity of this combined aPCR and microring resonator method, RT-aPCR amplification was performed separately for each of the eight targets with each amplicon-containing solution flowed over an array of microring sensors functionalized with capture probes against each specific target. As shown in **Figure 2-3**, hybridization responses are only observed for sensors functionalized with the appropriate sequence-specific capture probes, demonstrating a high degree of specificity.

Following the validation and calibration of this approach, we applied it to the simultaneous profiling of eight miRNA targets from total RNA extracted from twenty primary surgical brain tumor specimens, as well as a commercial “healthy” brain total RNA sample. RT followed by aPCR at defined cycle numbers was performed before hybridization analysis on the multiplexed microring sensor array. Data from the healthy total RNA sample and a representative glioma specimen (Subject A) are shown in **Figure 2-5A and B**, respectively, as a function of cycle number. $C(t)$ determination was achieved *via* the linear thresholding approach.

For visual comparison of relative fold changes²⁹ between the miRNA expression levels in the twenty brain tumor samples relative to the healthy control, the sensor responses were compiled into a heat map, shown in **Figure 2-6**. Differential miRNA expression is observed across the data set with some miRNAs showing higher expression (red) and others lower abundance (blue). Tumor samples are clearly heterogeneous and so it is important not to draw too substantial conclusions from this initial data. However, there are several observations that are at least partially consistent with literature precedent. For example, miRs-10b, 155, and 222 have been reported to be upregulated in some gliomas.³⁰⁻³² By contrast, miRs-34a and 29a have been reported as downregulated, again, in some gliomas.^{33,34} Larger scale miRNA expression profiling efforts might help identify important biomarkers with diagnostic utility for some tumor specimens/subtypes and the described microring resonator approach, coupled with aPCR, is a potentially valuable method for measuring targeted miRNA panels from larger research subject cohorts given the inherent scalability of the technology.

4. Conclusions

In summary, the integration of asymmetric PCR and silicon photonic microring resonator arrays resulted in the successful profiling of miRNAs from surgical glioma specimens with expression levels consistent with literature precedent. This approach leverages aPCR to selectively amplify miRNA targets using a new stem loop primer approach while enhancing multiplexing capacity over traditional qPCR methods through the use of label-free hybridization detection on using microring resonator arrays. We describe two methods for analyzing the hybridization responses as a function of cycle number and demonstrate that the conversion from duplex to single-strand amplification correlates with input target concentration. Importantly, this integrated approach is promising for targeted panel-based miRNA diagnostic approaches that continue to gain traction for applications in large cohort biomarker discovery. Future work that integrates together thermocycling with real-time, on-line hybridization measurements using sensor arrays could substantially lower reagent consumption and input requirements for multiplexed miRNA expression profiling.

FIGURES

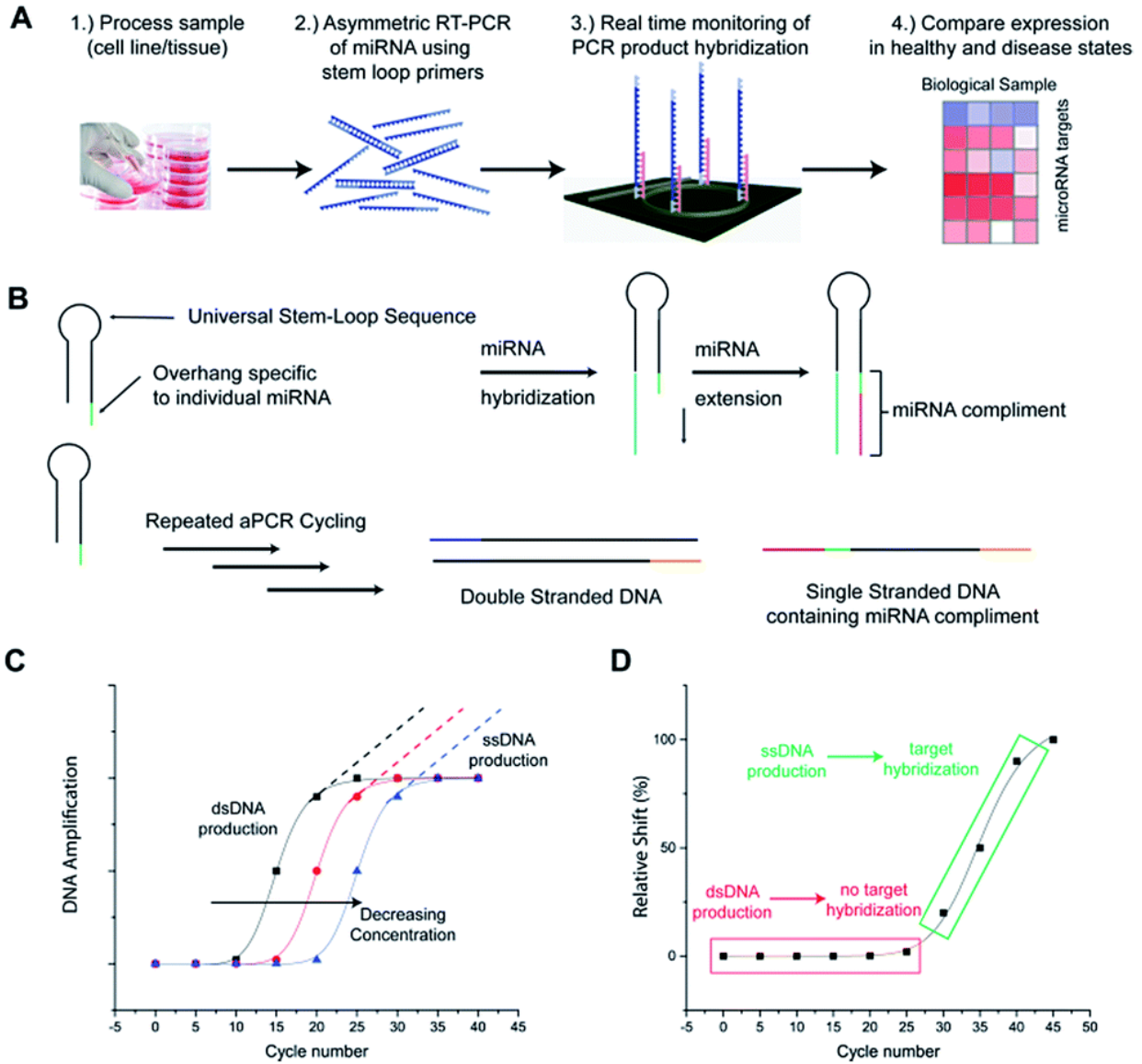


Figure 2-1. (A) Overview of the combined aPCR-microarray assay. Isolated RNA is reverse transcribed and asymmetrically amplified to single strand products that are detected *via* hybridization onto the sensor array. (B) Schematic illustration of reverse transcription using stem loop probes and aPCR amplification. (C) Plot showing DNA amplification as a function of increasing cycle number. Double-stranded product is made until the limiting primer is consumed, after which further cycling yields single-stranded products. (D) Resonance wavelength shifts are only detected after the transition to single-stranded production, which allows amplicons to hybridize to capture sequences arrayed onto unique microarray sensor elements.

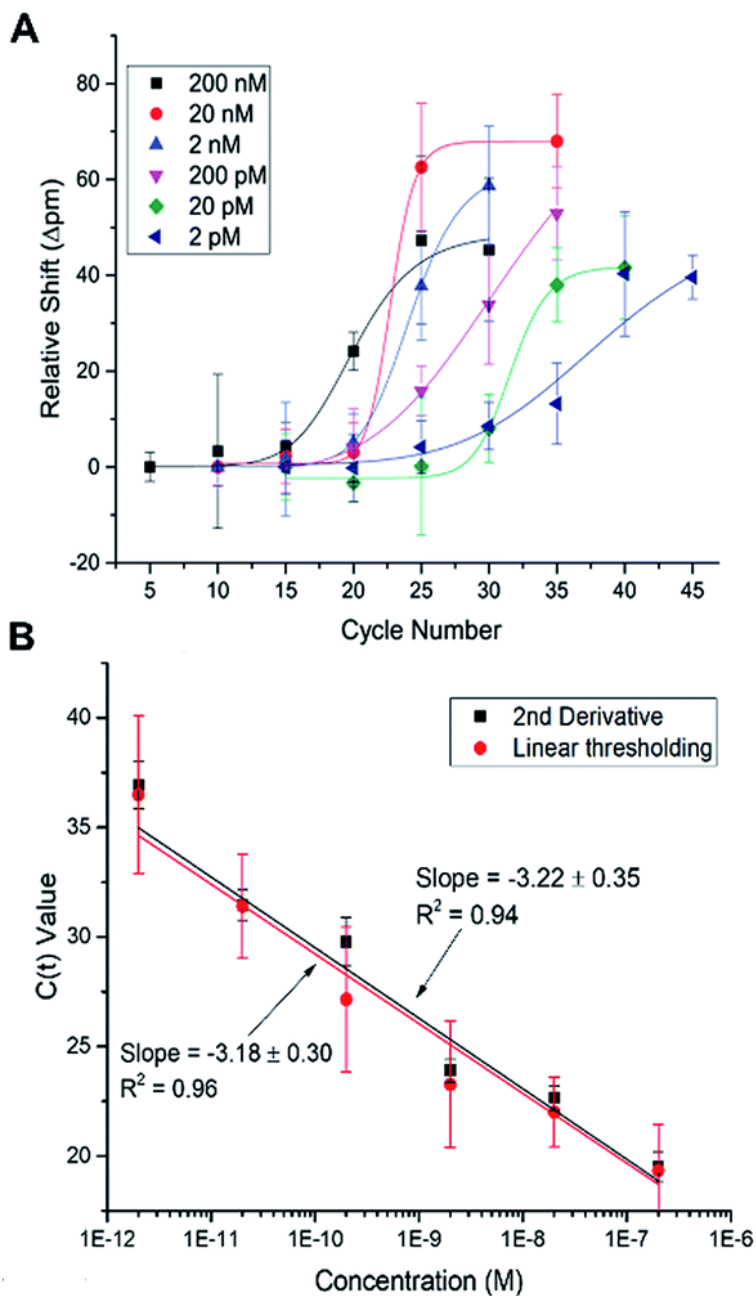


Figure 2-2. (A) Resonance wavelength shifts for various concentrations of let-7f as a function of cycle number. Error bars are the standard deviation from $n \geq 8$ microrings. Each cycle-dependent trace is fit with a logistic function. (B) Concentration-dependent calibration curves for let-7f determined using both the 2nd derivative and linear thresholding methods.

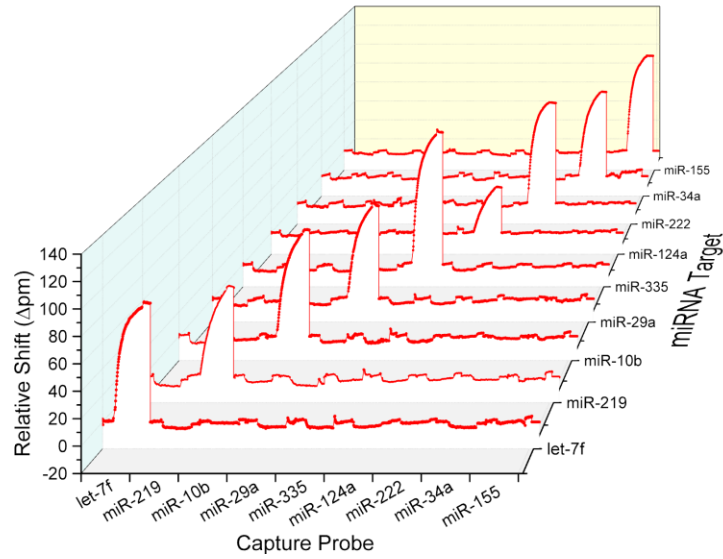


Figure 2-3. Cross reactivity experiments showing target-specific responses as each single miRNA aPCR product is flowed across a sensor array.

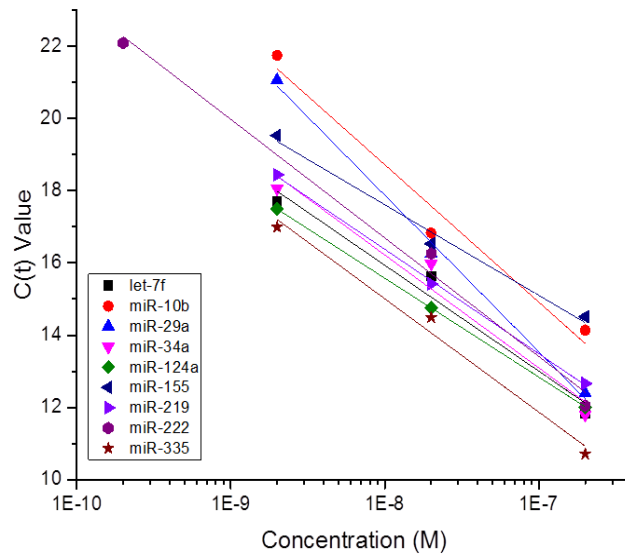


Figure 2-4. Amplification Validation of miRNA Targets. In order to prove linear amplification of all miRNA targets, 200 nM, 20 nM, and 2 nM samples of each target were subjected to the aPCR-microring assay using a stem loop primer concentration of 200 μ M. The results validated the designed primer sets by displaying linear amplification profiles.

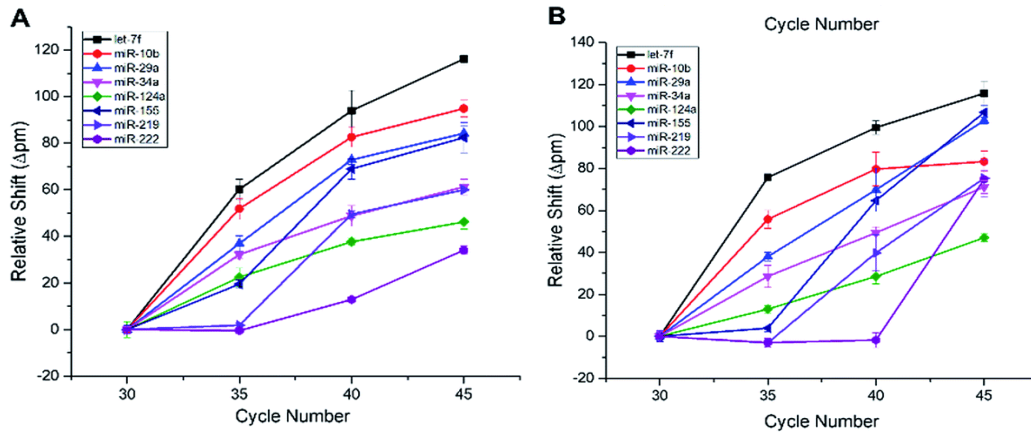


Figure 2-5. Resonance wavelength simultaneously measured by an array of microrings presenting capture probes for eight miRNAs after performing aPCR and hybridization analysis from a 10 ng input sample of (A) healthy brain total RNA, and (B) a representative primary glioma specimen (Subject A). (A and B) Results obtained when using a 10 ng input of a healthy control and glioma grade IV total RNA sample, respectively, and subjecting it to varying cycles of the aPCR-microring assay.

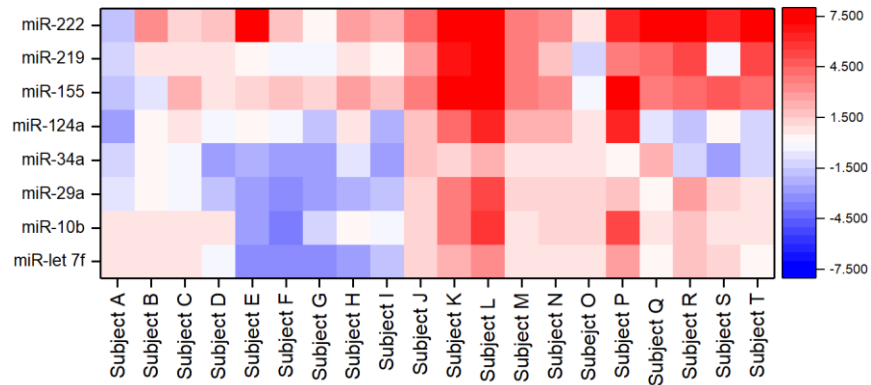


Figure 2-6. Heat map showing expression profiles from patient samples, relative to healthy control brain total RNA. Higher expression is indicated in red and lower in blue with numerical values plotted on a log₂ scale.

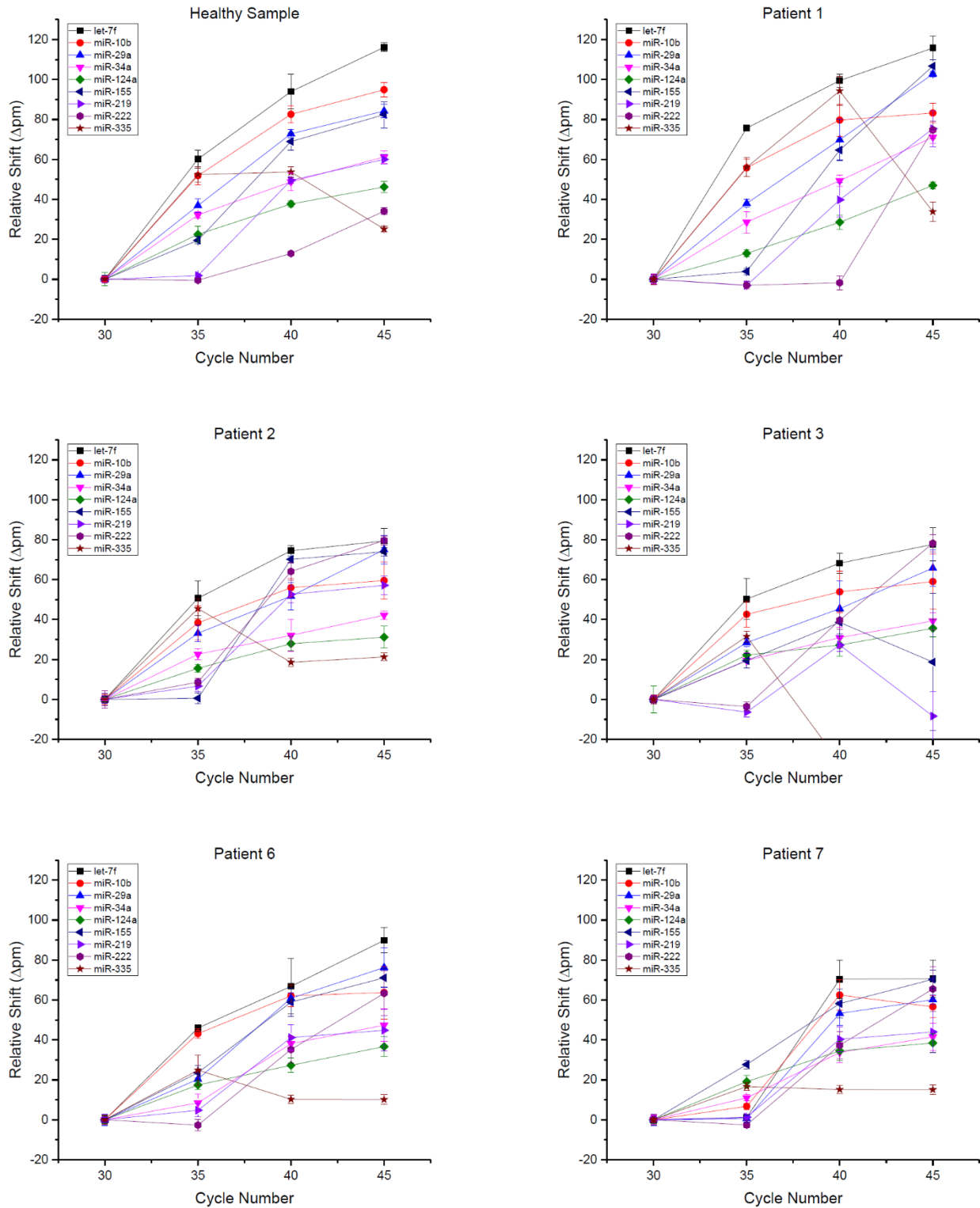


Figure 2-7. Plots used to calculate $C(t)$ values for each sample of interest.

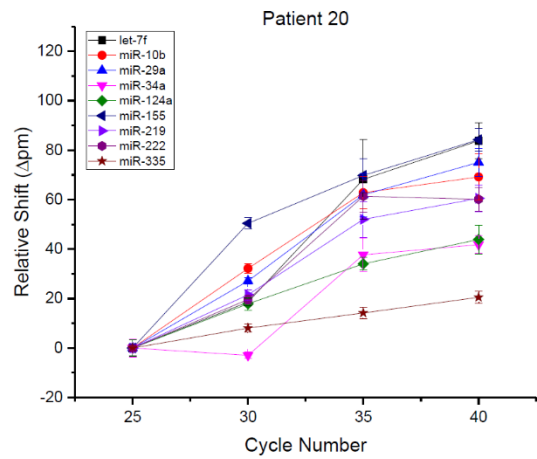
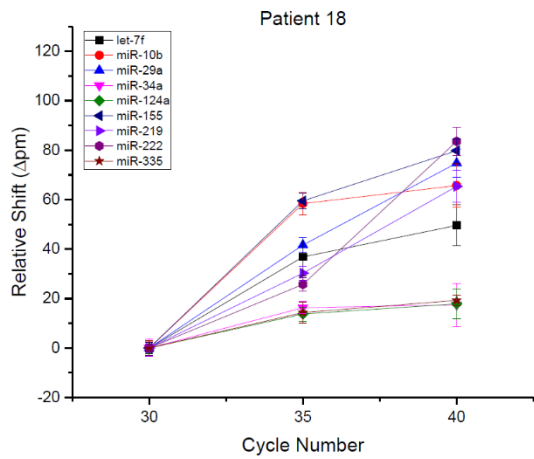
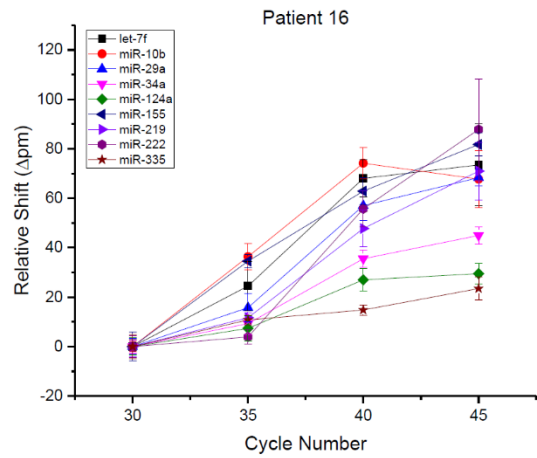
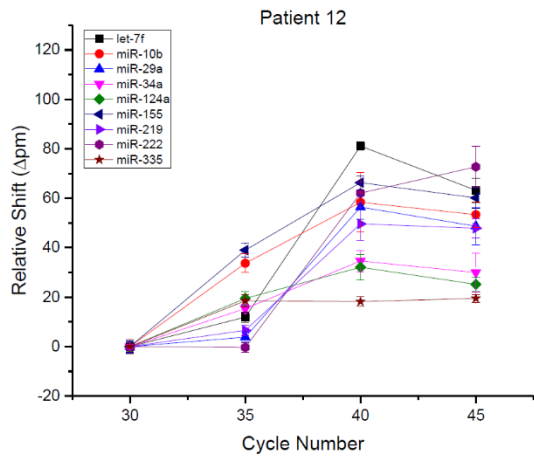
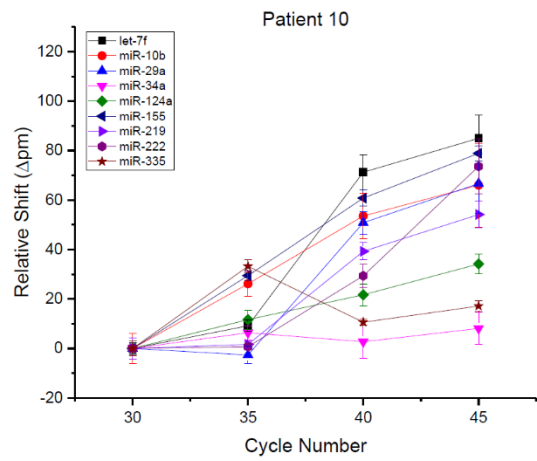
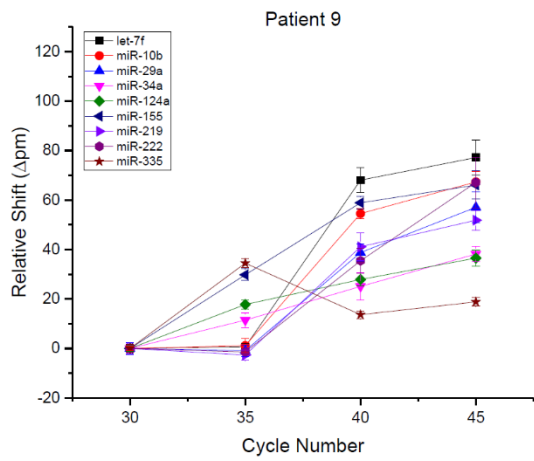


Figure 2-7: (cont.)

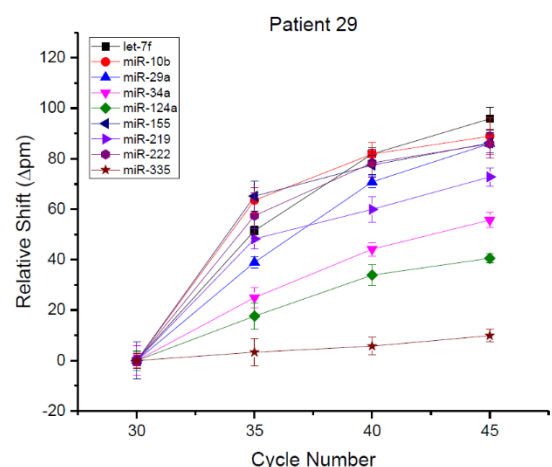
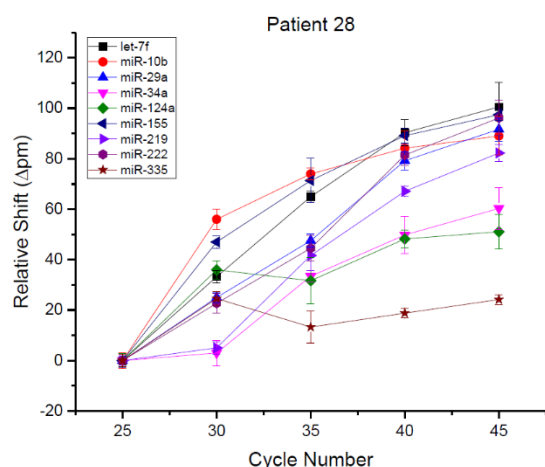
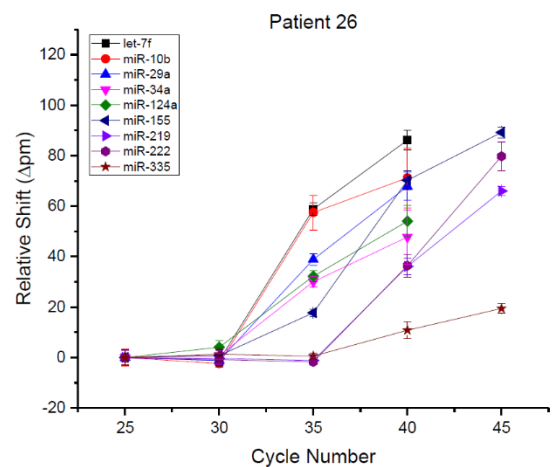
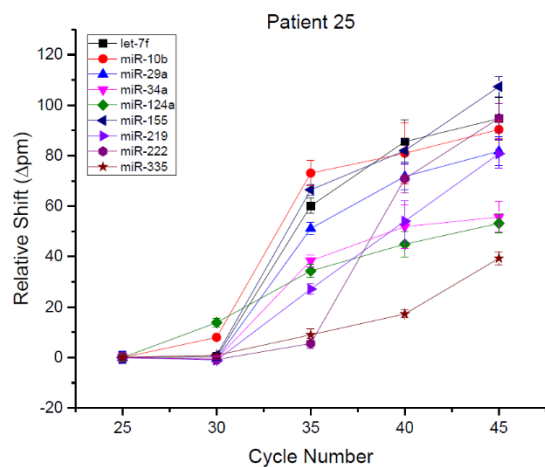
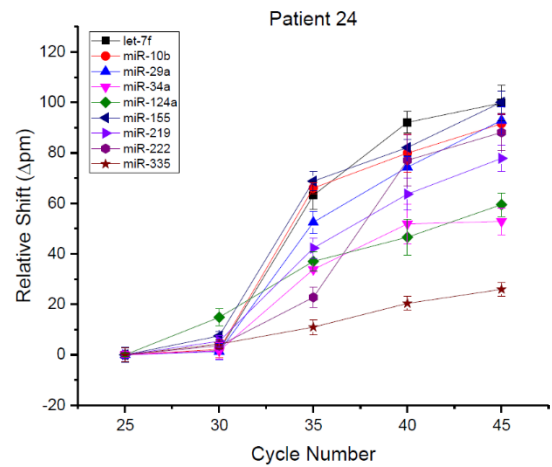
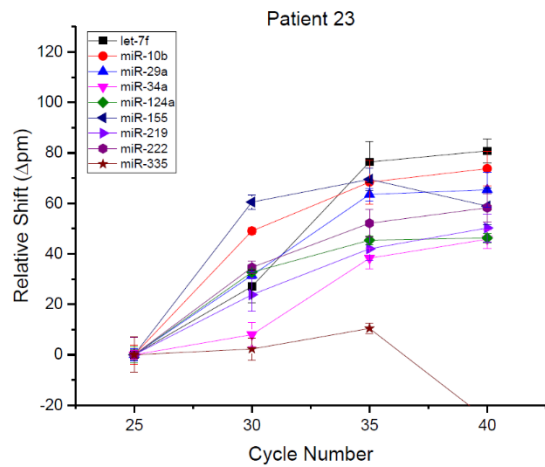


Figure 2-7: (cont.)

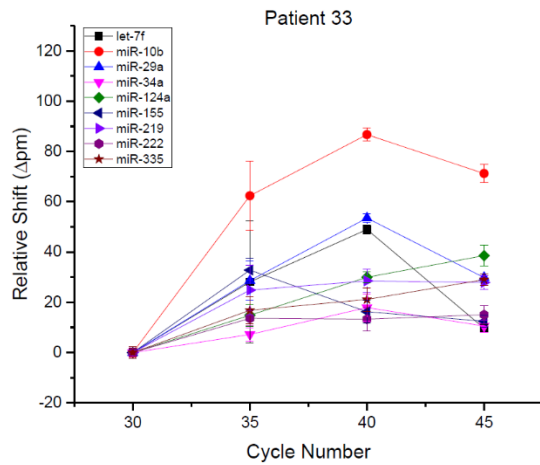
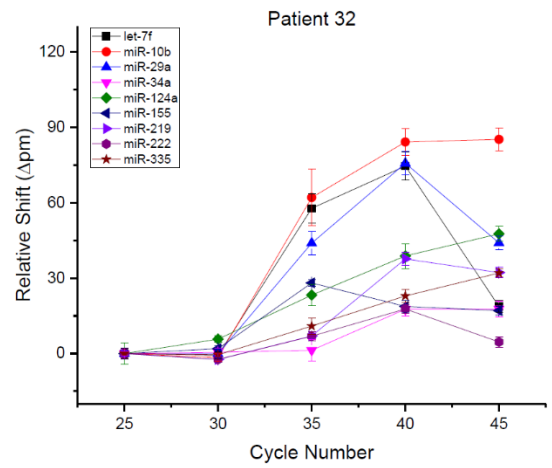
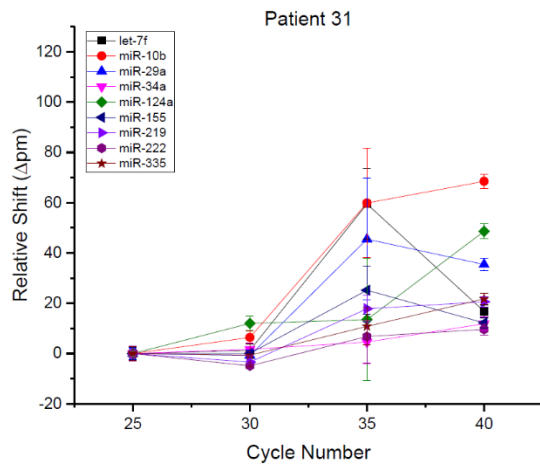


Figure 2-7: (cont.)

TABLES

Table 2-1. Summary of nucleic acid sequences.

	Sequence
hsa miRNA-let7f	UGAGGUAGUAGAUUGUAUAGUU
hsa miRNA-219	UGAUUGUCCAAACGCAAUUCU
hsa miRNA-10b	UACCCUGUAGAACCGAAUUUGUG
hsa miRNA-29a	UAGCACCAUCUGAAAUCGGUUA
hsa miRNA-335	UCAAGAGCAAUAACGAAAAAUGU
hsa miRNA-124a	UAAGGCACGCGGUGAAUGCC
hsa miRNA-222	AGCUACAUCUGGCUACUGGGUCUC
hsa miRNA-34a	UGGCAGUGUCUUAGCUGGUUGU
hsa miRNA-155	UAA AUGCUAAUCGUGAUAGGGGU
Conserved Stem Loop Primer	GTCGTATCCAGTGCAGGGTCCGAGGTATTCGCACTG GAT... miRNA specific overhang
miR-let7f SLP overhang	AACTATAC
miR-219 SLP overhang	AGAATTG
miR-10b SLP overhang	CACAAATTC
miR-29a SLP overhang	TAACCG
miR-335 SLP overhang	ACATTTTT
miR-124a SLP overhang	GGCATTG
miR-222 SLP overhang	GAGACCC
miR-34a SLP overhang	ACAACCA
miR-155 SLP overhang	ACCCCT
Conserved reverse primer	GTGCAGGGTCCGAGGT
miR-let7f PCR forward primer	CGCGCTGAGGTAGTAGATT
miR-219 PCR forward primer	CGCGTGATTGTCAAACG
miR-10b forward primer	GCGTACCCTGGTAGAACC
miR-29a forward primer	CGCTAGCACCATCTGAAAT
miR-335 forward primer	CGCGTCAAGAGCAATAACG
miR-124a forward primer	CGTAAGGCACGCGGT
miR-222 forward primer	CGAGCTACATCTGGCTACT
miR-34a forward primer	GCGTGGCAGTGTCTTAGC
miR-155 forward primer	CGCGTTAATGCTAATCGTGAT

Table 2-2. Details on fluid flow conditions.

Step	Sequence	Duration (min)
Hybridization buffer	20	5
RT-PCR product	20	15
Hybridization buffer	20	5

Table 2-3. Patient information.

Patient Sample	Gender	Age	Cancer type
1	M	62	Glioma – grade IV
2	M	42	Glioma – grade IV
3	M	47	Glioma – grade IV
6	F	52	Glioma – grade II
7	F	67	Glioma – grade IV
9	F	75	Glioma – grade IV
10	F	29	Glioma – grade III
12	F	48	Glioma – grade IV
16	F	37	Glioma – grade III
18	F	35	Glioma – grade III
20	M	26	Glioma – grade IV
23	M	38	Glioma – grade IV
24	F	67	Glioma – grade IV
25	M	25	Glioma – grade III
26	F	27	Glioma – grade II
28	M	30	Glioma – grade III
29	M	51	Glioma – grade IV
31	F	63	Meningioma – grade I
32	F	69	Glioma – grade IV
33	F	74	Meningioma – grade I

Table 2-4. Fold changes presented in heat map (log2).

Patient	let	miR-	miR-	miR-	miR-	miR-	miR-	miR-	miR-
1	0.83	0.68	-0.92	-1.18	-2.76	-1.81	-1.19	-1.78	-1.27
2	0.73	0.55	0.09	0.05	0.12	-0.7	0.61	3.02	0.08
3	0.8	0.88	-0.14	-0.27	0.91	2.42	0.71	1.45	0.07
6	-	0.7	-1.65	-2.97	-0.08	0.73	0.53	1.7	0.07
7	-3.1	-2.95	-2.63	-2.44	0.11	1.29	0.27	8.05	-6.21
9	-	-3.72	-3.31	-2.62	-0.02	1.96	-0.01	1.87	0.07
10	-	-1.35	-2.89	-2.51	-1.89	1.03	-0.3	0.04	0.1
12	-2.6	0.23	-2.22	-0.74	0.81	2.98	0.84	2.67	-0.03
16	-	-0.43	-1.8	-2.85	-2.02	1.68	0.05	2.07	-2.25
18	1.21	1.43	1	1.66	1.51	3.6	2.86	4.32	-0.68
20	2.35	3.76	3.9	1.15	4.17	8.02	6.86	9.44	1.95
23	3.36	5.68	5.42	2.1	6.3	9.08	8.14	11.67	0.91
24	0.73	0.94	1.08	0.76	2.09	3.7	3.79	3.9	-2.51
25	0.69	1.46	1.38	0.88	2.23	3.14	1.54	3.15	-7.03
26	0.99	1.23	1.19	0.61	0.97	-0.38	-1.24	0.86	-6.44
28	2.73	5.46	1.97	0.32	6.23	8.51	3.54	6.45	5.05
29	0.11	0.83	0.17	2.35	-0.51	3.73	4.32	7.05	-4.29
31	1.94	1.68	2.6	-1.37	-1.76	4.4	5.38	9.48	-1.73
32	1.33	0.98	1.16	-2.98	0.31	4.59	-0.13	6.27	-3.55
33	0.37	0.86	0.83	-1.21	-1.1	4.38	5.01	7.85	-1.36

BIBLIOGRAPHY

- (1) Liotta, L.; Petricoin, E. Molecular Profiling of Human Cancer. *Nat. Rev. Genet.* **2000**, *1* (1), 48–56.
- (2) Hanash, S. M.; Baik, C. S.; Kallioniemi, O. Emerging Molecular Biomarkers—blood-Based Strategies to Detect and Monitor Cancer. *Nat. Rev. Clin. Oncol.* **2011**, *8* (3), 142–150.
- (3) Pritchard, C. C.; Cheng, H. H.; Tewari, M. MicroRNA Profiling: Approaches and Considerations. *Nat. Publ. Gr.* **2012**, *13*, 358-369.
- (4) Calin, G. A.; Croce, C. M. MicroRNA-Cancer Connection: The Beginning of a New Tale. *Cancer Res.* **2006**, *66* (15), 7390–7394.
- (5) Madrigal-Matute, J.; Rotllan, N.; Aranda, J. F.; Fernández-Hernando, C. MicroRNAs and Atherosclerosis. *Curr. Atheroscler. Rep.* **2013**, *15* (5), 322.
- (6) Vickers, K. C.; Rye, K.-A.; Tabet, F. MicroRNAs in the Onset and Development of Cardiovascular Disease. *Clin. Sci.* **2014**, *126* (3), 183–194.
- (7) Zhu, S.; Pan, W.; Qian, Y. MicroRNA in Immunity and Autoimmunity. *J. Mol. Med.* **2013**, *91* (9), 1039–1050.
- (8) Abe, M.; Bonini, N. M. MicroRNAs and Neurodegeneration: Role and Impact. *Trends Cell Biol.* **2013**, *23* (1), 30–36.
- (9) Fan, Y.; Siklenka, K.; Arora, S. K.; Ribeiro, P.; Kimmins, S.; Xia, J. MiRNet - Dissecting MiRNA-Target Interactions and Functional Associations through Network-Based Visual Analysis. *Nucleic Acids Res.* **2016**, *44* (W1), W135–W141.
- (10) Graybill, R. M.; Bailey, R. C. Emerging Biosensing Approaches for MicroRNA Analysis. *Anal. Chem.* **2016**, *88* (1), 431–450.

- (11) Carrascosa, L. G.; Huertas, C. S.; Lechuga, L. M. Prospects of Optical Biosensors for Emerging Label-Free RNA Analysis. *TrAC Trends Anal. Chem.* **2016**, *80*, 177–189.
- (12) Henriksen, M.; Johnsen, K. B.; Andersen, H. H.; Pilgaard, L.; Duroux, M. MicroRNA Expression Signatures Determine Prognosis and Survival in Glioblastoma Multiforme—a Systematic Overview. *Mol. Neurobiol.* **2014**, *50* (3), 896–913.
- (13) Iqbal, M.; Gleeson, M. A.; Spaugh, B.; Tybor, F.; Gunn, W. G.; Hochberg, M.; Baehr-Jones, T.; Bailey, R. C.; Gunn, L. C. Label-Free Biosensor Arrays Based on Silicon Ring Resonators and High-Speed Optical Scanning Instrumentation. *IEEE J. Sel. Top. Quantum Electron.* **2010**, *16* (3), 654–661.
- (14) Washburn, A. L.; Gunn, L. C.; Bailey, R. C. Label-Free Quantitation of a Cancer Biomarker in Complex Media Using Silicon Photonic Microring Resonators. *Anal. Chem.* **2009**, *81* (22), 9499–9506.
- (15) Wade, J. H.; Alsop, A. T.; Vertin, N. R.; Yang, H.; Johnson, M. D.; Bailey, R. C. Rapid, Multiplexed Phosphoprotein Profiling Using Silicon Photonic Sensor Arrays. *ACS Cent. Sci.* **2015**, *1* (7), 374–382.
- (16) Sloan, C. D. K.; Marty, M. T.; Sligar, S. G.; Bailey, R. C. Interfacing Lipid Bilayer Nanodiscs and Silicon Photonic Sensor Arrays for Multiplexed Protein–Lipid and Protein–Membrane Protein Interaction Screening. *Anal. Chem.* **2013**, *85* (5), 2970–2976.
- (17) Kindt, J. T.; Bailey, R. C. Chaperone Probes and Bead-Based Enhancement To Improve the Direct Detection of mRNA Using Silicon Photonic Sensor Arrays. *Anal. Chem.* **2012**, *84* (18), 8067–8074.
- (18) Qavi, A. J.; Mysz, T. M.; Bailey, R. C. Isothermal Discrimination of Single-Nucleotide Polymorphisms via Real-Time Kinetic Desorption and Label-Free Detection of DNA Using Silicon Photonic Microring Resonator Arrays. *Anal. Chem.* **2011**, *83* (17), 6827–6833.
- (19) McClellan, M. S.; Domier, L. L.; Bailey, R. C. Label-Free Virus Detection Using Silicon Photonic Microring Resonators. *Biosens. Bioelectron.* **2012**, *31* (1), 388–392.
- (20) Qavi, A. J.; Bailey, R. C. Multiplexed Detection and Label-Free Quantitation of

- MicroRNAs Using Arrays of Silicon Photonic Microring Resonators. *Angew. Chemie Int. Ed.* **2010**, *49* (27), 4608–4611.
- (21) Qavi, A. J.; Kindt, J. T.; Gleeson, M. A.; Bailey, R. C. Anti-DNA:RNA Antibodies and Silicon Photonic Microring Resonators: Increased Sensitivity for Multiplexed MicroRNA Detection. *Anal. Chem* **2011**, *83*, 5949–5956.
- (22) Graybill, R. M.; Para, C. S.; Bailey, R. C. PCR-Free, Multiplexed Expression Profiling of MicroRNAs Using Silicon Photonic Microring Resonators. *Anal. Chem.* **2016**, *88* (21), 10347–10351.
- (23) Pollet, J.; Janssen, K. P. F.; Knez, K.; Lammertyn, J. Real-Time Monitoring of Solid-Phase PCR Using Fiber-Optic SPR. *Small* **2011**, *7* (8), 1003–1006.
- (24) Gyllensten, U. B.; Erlich, H. A. Generation of Single-Stranded DNA by the Polymerase Chain Reaction and Its Application to Direct Sequencing of the HLA-DQA Locus. *Proc. Natl. Acad. Sci. U. S. A.* **1988**, *85* (20), 7652–7656.
- (25) Sanchez, J. A.; Pierce, K. E.; Rice, J. E.; Wangh, L. J. Linear-After-The-Exponential (LATE)–PCR: An Advanced Method of Asymmetric PCR and Its Uses in Quantitative Real-Time Analysis. *Proc. Natl. Acad. Sci.* **2004**, *101* (7), 1933–1938.
- (26) Eriko Kai, †; Shinya Sawata, ‡; Kazunori Ikebukuro, †; Tetsuya Iida, §; Takeshi Honda, § and; Isao Karube*, †. Detection of PCR Products in Solution Using Surface Plasmon Resonance. **1999**.
- (27) Zhu, L.-X.; Zhang, Z.-W.; Liang, D.; Jiang, D.; Wang, C.; Du, N.; Zhang, Q.; Mitchelson, K.; Cheng, J. Multiplex Asymmetric PCR-Based Oligonucleotide Microarray for Detection of Drug Resistance Genes Containing Single Mutations in Enterobacteriaceae. *Antimicrob. Agents Chemother.* **2007**, *51* (10), 3707–3713.
- (28) Chung, H. J.; Castro, C. M.; Im, H.; Lee, H.; Weissleder, R. A Magneto-DNA Nanoparticle System for Rapid Detection and Phenotyping of Bacteria. *Nat. Nanotechnol.* **2013**, *8* (5), 369–375.
- (29) Chen, C.; Ridzon, D. A.; Broomer, A. J.; Zhou, Z.; Lee, D. H.; Nguyen, J. T.; Barbisin, M.;

- Xu, N. L.; Mahuvakar, V. R.; Andersen, M. R.; et al. Real-Time Quantification of MicroRNAs by Stem-Loop RT-PCR. *Nucleic Acids Res.* **2005**, *33* (20), e179.
- (30) Schmittgen, T. D.; Livak, K. J. Analyzing Real-Time PCR Data by the Comparative C(T) Method. *Nat. Protoc.* **2008**, *3* (6), 1101–1108.
- (31) Lin, J.; Teo, S.; Lam, D. H.; Jeyaseelan, K.; Wang, S. MicroRNA-10b Pleiotropically Regulates Invasion, Angiogenicity and Apoptosis of Tumor Cells Resembling Mesenchymal Subtype of Glioblastoma Multiforme. *Cell Death Dis.* **2012**, *3* (10), e398–e398.
- (32) Zhou, J.; Wang, W.; Gao, Z.; Peng, X.; Chen, X.; Chen, W.; Xu, W.; Xu, H.; Lin, M. C.; Jiang, S. MicroRNA-155 Promotes Glioma Cell Proliferation via the Regulation of MXI1. *PLoS One* **2013**, *8* (12), e83055.
- (33) Quintavalle, C.; Garofalo, M.; Zanca, C.; Romano, G.; Iaboni, M.; del Basso De Caro, M.; Martinez-Montero, J. C.; Incoronato, M.; Nuovo, G.; Croce, C. M.; et al. MiR-221/222 Overexpression in Human Glioblastoma Increases Invasiveness by Targeting the Protein Phosphate PTP μ . *Oncogene* **2012**, *31* (7), 858–868.
- (34) Yin, D.; Ogawa, S.; Kawamata, N.; Leiter, A.; Ham, M.; Li, D.; Doan, N. B.; Said, J. W.; Black, K. L.; Phillip Koeffler, H. MiR-34a Functions as a Tumor Suppressor Modulating EGFR in Glioblastoma Multiforme. *Oncogene* **2013**, *32* (9), 1155–1163.

CHAPTER III

Combining asymmetric PCR-based enzymatic amplification with silicon photonic microring resonators for the detection of lncRNAs from low input human RNA samples

Acknowledgments

This chapter has been adapted from the research article “Combining asymmetric PCR-based enzymatic amplification with silicon photonic microring resonators for the detection of lncRNAs from low input human RNA samples” (Cardenosa-Rubio, M.C.; Graybill, R.M.; Bailey, R.C., *Analyst*, **2018**, *143*, 1210-1216). The article has been reproduced here with permission from the Royal Society of Chemistry © 2018.[‡]

My contribution in this research correspond to the research idea, biomarker choice, primer design and optimization of the experiments, the realization of the calibration curves, analysis of the results and measurement in the patient samples. I also wrote the article. Richard Graybill contributed in the research idea and helped in the collection of the data. He also helped with the final revision of the paper.

The authors gratefully acknowledge financial support from the National Cancer Institute of the National Institutes of Health through Grant R33CA1774. MCR acknowledges support from a la Caixa Banking Foundation Fellowship. RMG acknowledges support from the National Cancer Institute Alliance for Nanotechnology in Cancer “Midwest Cancer Nanotechnology Training Center” Grant R25CA154015A. We appreciate technical assistance from the University of Michigan DNA Sequencing Core. We would also like to thank Dr Jann Sarkaria, Mark Schroeder, and Brett Carlson (Mayo Clinic) for providing the GBM6 patient-derived xenograft cells.

[‡] <http://www.rsc.org/journals-books-databases/journal-authors-reviewers/licences-copyright-permissions/>

Abstract

A method for quantifying biologically relevant long-non-coding RNAs by combining nucleic acid amplification via asymmetric polymerase chain reaction (PCR) with label-free PCR product detection using silicon photonic microring resonator arrays is described. This approach eliminates the need for fluorophores, which presents a limit for spectral multiplexing in conventional qPCR methods, and rather offers potential for much higher levels of plexity by spatially arraying capture probes. Here, we demonstrate the potential of this technique to detect two differentially expressed lncRNA transcripts and an internal control mRNA transcript in different commercial human tissue specimens, as well as in a glioblastoma cell line using only nanogram input amounts of total RNA. The obtained results were validated using single-plex RT-qPCR and found to be in good agreement, demonstrating the potential of this technique for lncRNA quantification applications.

1. Introduction

In recent years increased attention has been given to multiplexed biomolecular analysis because of its potential to revolutionize areas of human health, such as disease diagnosis and therapeutic selection. The discovery of potential biomarkers for different diseases has been one of the main drivers in the development of multiplexed diagnostic analysis. Among the different types of biomarkers, RNA molecules have risen in importance thanks to the use of next generation sequencing and the resulting insights in cell signaling regulation.¹ Furthermore, accumulating reports noting the differential expression of non-coding RNAs (ncRNAs) in disease suggest that they may also emerge as diagnostic biomarkers for a number of diseases.²

Though having profound regulatory effects at the levels of transcription and translation, ncRNAs do not encode for proteins. ncRNAs are commonly divided into two major groups based on their length: small non coding RNAs, which include Piwi-interacting RNAs, small-interfering RNAs and microRNAs; and long non-coding RNAs, lncRNAs, which are defined as those longer than 200 nucleotides.³ Since the discovery of the first well-studied lncRNA, H19,⁴ many additional lncRNAs have been identified that affect diverse biological functions.⁵⁻⁷ For example, in cancer lncRNAs can support both tumor suppressive and oncogenic functions.^{8,9}

It has been suggested that multiplexed lncRNA-based diagnostics revealing differential, disease-specific expression in cancers such as glioma might provide valuable information regarding subtype and malignancy in these tumors.^{10,11} One study, based on in silico analysis of

data from The Cancer Genome Atlas, identified a signature of six lncRNAs that might be predictive of survival in patients with glioblastoma. Another report utilized microarray data to subtype and grade of glioma based on lncRNA signatures. Importantly, this study showed that from an initial large pool of potential lncRNA biomarkers (~2,000 potential lncRNA), around 25-50 targets held diagnostic significance. This example, which is supported by other biomarkers studies, places an impetus on developing moderately multiplexed approaches to detecting targeted panels of lncRNAs for clinical diagnostic applications.

To date, the most common approaches to detecting lncRNA expression have been based upon RT-qPCR, hybridization assays such as microarrays, and RNA sequencing.^{12,13} While these techniques are generally robust, sensitive, and, in the case of RNA sequencing, allow for the discovery of new lncRNAs, each has limitations for the realization of panel-based diagnostics in the clinical laboratory settings. RT-qPCR-based approaches typically only detect a single target per sample. Microarrays detect many targets, but are laborious and often only qualitative. RNA sequencing has become commonplace for lncRNA discovery and expression profiling; however, it is still prohibitively expensive for studies looking at large numbers of clinical samples, and also requires extensive bioinformatic data analysis. Therefore, there is an opportunity for the emergence of new biosensing technologies to fill this void by offering moderately multiplexed, targeted lncRNA detection capabilities that are quantitative, robust, and cost-effective.

In response to this challenge, we have developed a silicon photonic microring resonator technology that is well-suited to the multiplexed detection of targeted biomarker panels. The specifics of this technology have been previously discussed generally,^{14,15} and more relevant to this work, for label-free RNA analysis.¹⁶ The sensing principle is based on the change of refractive index near the surface of the rings, which occurs when biomolecules selectively bind to receptors covalently bound to the microring surface. The label-free operation of this technology provides advantages over those that rely upon fluorescent or enzymatic tags to generate the detectable signal. Another advantage of this technology is the ability to create spatially-arrayed, high density sensor arrays, which intrinsically affords the potential for multiplexed detection. The promise of these sensors for multiplexed analysis has been previously demonstrated for RNA targets;¹⁶⁻¹⁹ however, the limits of detection for these approaches were insufficient for many clinical applications where sample input is restricted.

In this manuscript, we report an approach to lncRNA analysis that leverages asymmetric PCR (aPCR) to selectively produce single stranded DNA (ssDNA) products upstream of label-free, hybridization-based detection using microring resonator arrays (**Figure 3-1**). aPCR is based upon standard PCR; however, an excess of one primer results in the creation of single stranded products after consumption of all of the limiting primer.^{20,21} This combination allowed RNA quantification with a 1000-fold reduction in input RNA, compared to our previous report of mRNA detection using microring resonators.¹⁸ In addition to detecting two lncRNAs, we also included in the panel an internal control mRNA sequence. We demonstrated the applicability to detect these disease-relevant targets from both cultured cells and commercially-obtained human total RNA samples. We validated this approach by parallel analysis with RT-qPCR and also found that disease- and tissue-specific relative lncRNA expression profiles were consistent with literature precedent. Together, these comparisons support the promise of this combined aPCR-microring resonator approach for multiplexed lncRNA analysis in both clinical and basic research settings.

2. Materials and methods

Materials

All nucleic acid sequences (primers and capture probes) were purchased from Integrated DNA Technologies (IDT; Coralville, IA). The TaqMan® microRNA Reverse Transcription Kit, Platinum® Multiplex PCR Master Mix, SYBR® Select Master Mix, 3-aminopropyltriethoxysilane (APTES) and bis(sulfosuccinimidyl)suberate (BS3) were purchased from ThermoFisher. All buffer dilutions, DNA primer reconstitution, and DNA primer dilutions were prepared in nuclease-free Ultrapure distilled water (Invitrogen). Phosphate-buffered saline (PBS) was obtained from Lonza and was used in the reconstitution of the oligonucleotide capture probes. A high stringency hybridization buffer was made in 50 mL batches containing 15 mL of formamide (Fisher), 1 mL 10% sodium dodecyl sulfate (Fisher), 10 mL 20X saline-sodium phosphate buffer (Invitrogen), 6 mL 0.25 M ethylenediaminetetraacetic acid (Invitrogen) and 2.5 mL 50X Denhardt's solution (Invitrogen).

RNA sample preparation

Total RNA was extracted from GBM6 cell lines lysates with a miRNeasy® Mini kit (Quiagen) using manufacture's protocol. After extraction, total RNA was assessed for purity and

quantity using a Nanodrop UV–vis spectrometer and stored at -80°C until further use. Brain and Lung Reference total RNA samples were obtained from ThermoFisher and stored at -80°C until further use.

Amplification primers and capture probe design.

Specific primers and capture probes for the amplification and detection of the human lncRNAs MALAT1 and KIAA0495, and the internal control β -actin, were designed using sequence annotations from Genbank (NCBI) and the Primer-Blast platform (NCBI). Secondary structures were visualized using the Dinamelt web server.²² Sequences of the primers and capture probes are listed in **Table 3-1**.

Silicon Photonic Microring Resonator Instrumentation

Microring sensor arrays and sensor scanner equipment were purchased from Genalyte, Inc. (San Diego, CA), and the detection instrumentation and method has been described previously.^{14,15} Sensor arrays were fabricated on silicon-on-insulator wafers by photolithography and standard etching techniques. After etching to define the microrings, a polymer cladding was deposited across the entire substrate and then selectively etched to expose active sensor rings. Four microrings remaining occluded and served as controls for thermal drift. The final sensor chips were diced to 6 mm x 4 mm and each contain 132 individually-addressable microring resonator sensors. For sensing experiments, the chips are loaded into a fluidic cartridge with a Mylar gasket and Teflon lid directing solution flow across the array in two separate channels. There are 64 active sensors in each channel. Fluid flow is controlled by integrated syringe pumps under software control.

Surface functionalization of the microring resonators

Sensors were first silanized with a 5% APTES solution in acetone for 4 min followed by successive two-minute rinses in acetone and isopropanol. These steps were completed with continuous shaking. Chips were then rinsed with water and dried under a stream of nitrogen. Next, 20 μL of a freshly prepared BS3 solution (2.85 mg/mL in 2 mM acetic acid) was pipetted onto the microring array and allowed to react for 3 minutes, followed by drying under a stream of nitrogen. The final step of functionalization involved spotting approximately 260 nL of 200 μM solutions

containing 5'-amino functionalized DNA captures probes onto discrete microring sensors. The chips were then incubated overnight in a humidity chamber.

Reverse transcription–asymmetric PCR

Reverse transcription reactions were performed using the TaqMan microRNA Reverse Transcription Kit. Each 15 μL reaction volume contained 4.16 μL of nuclease free water, 1.5 μL of 10x RT buffer, 1 μL of Multiscribe™ RT enzyme (50 U/ μL), 0.19 μL of RNase inhibitor (20 U/ μL), 0.15 μL dNTP mix (100 mM), 5 μL of RNA sample (40 ng RNA total), and 3 μL of reverse transcription primer. The concentration of the reverse primer was 200 μM when only one transcript was reverse-transcribed and 66 μM when three transcripts were reverse transcribed. The thermal profile was completed following the manufacturer's suggested protocol: 65° C (5 min), 4° C (2 min), 42° C (30 min), and 85° C (5 min).

Asymmetric PCR was performed using the Platinum® Multiplex PCR Master Mix. Each 50 μL reaction volume was composed of 14 μL nuclease free water, 25 μL of Platinum® Multiplex PCR Master Mix, 5 μL of each primer, and 1 μL of the reverse transcription product. The concentration of the forward primer (limiting primer) was 2 μM while the concentration of the reverse primer (excess primer) was 200 μM . The reactions were incubated at 95° C for 2 min, followed by cycles of 95° C for 30 s, 58° C for 45 s, and 72° C for 30 s. To profile the amplification process, PCR samples were taken from the thermocycler at different cycle numbers (i.e. every two cycles or every five cycles).

Sensor fluidics and sample introduction

PCR samples (50 μL) were diluted in 350 μL of the hybridization buffer described in the Materials section. Hybridization of the amplified products was carried out at room temperature by flowing solutions across the chip surface at a rate of 20 $\mu\text{L}/\text{min}$ for 13 min. After the hybridization of each cycle sample, the chip was rinsed with the hybridization buffer for 2 min before introduction of the next sample of successively higher cycle number. The full hybridization assay protocol is provided in **Table 3-2**.

Quantitative PCR

Real-time quantitative PCR (RT-qPCR) was performed using a 7900HT Fast Real-Time PCR system (Thermo Fisher) using the RT protocol described above. Each reaction contained 5.6

μL of nuclease free water, 10 μL of SYBR® Select Master Mix, 2 μL of each primer (2 μM) and 0.4 μL of the reverse transcription product. The reaction was initiated at 95° C for 2 min, followed by 40 cycles that included 95° C for 15 s followed by 58° C for 1 min. Threshold cycle (Ct) was automatically determined by the provided software.

Data analysis

The microring response was analyzed using OriginPro8 (OriginLab, Northampton, MA). The net shift signal from specific rings was corrected for temperature and instrument drift by subtracting the signal of thermal control rings from the active rings functionalized with DNA capture probes. The data for every target in each sample was detected and averaged using between 8 and 16 replicate microrings on a single chip.

3. Results and discussion

In this study, we used asymmetric PCR to amplify two long non-coding RNAs and quantify expression levels within three different RNA samples using a label-free microring resonator detection platform. The schematic of the assay is shown in **Figure 3-1**. In this assay, lncRNAs from different RNA samples were reversed transcribed using the target specific primers listed in **Table 3-1**. After reverse transcription, asymmetric PCR was used to selectively produce ssDNA at cycle numbers that are proportional to the initial concentration of the target within the sample of interest. In asymmetric PCR one of the primers is in a limiting concentration so that when all of the limiting primer is consumed, exponential amplification transitions to linear amplification creating ssDNA from the excess primer.^{20,21} The resulting ssDNA product can then be detected by hybridization to complementary capture probes covalently attached to the surface of microring resonators.

With this assay, we aimed to mimic the quantification process of qPCR, so we collected asymmetric PCR samples after varying numbers of thermal cycles. In the case of conventional qPCR, double stranded DNA is detected by the addition of SYBR dyes® and fluorescence intensity increases upon double stranded DNA (dsDNA) accumulation. The fluorescent intensity is plotted against increasing PCR cycle number and expression profiles can be calculated based on the cycle at which fluorescent signal begins. With the aPCR-microring system, we quantitate ssDNA accumulation instead of dsDNA. Resonance wavelength shifts increase upon hybridization

of increasing concentrations of generated ssDNA, which occurs only after the transition from exponential dsDNA generation to linear amplification upon limiting primer consumption (**Figure 3-1B**). As a result, quantitation occurs at higher cycle numbers than traditional qPCR.

An important step in the optimization of this approach was the design of primer pairs and the resulting PCR products to avoid targeting regions of extensive secondary structure, which would preclude primer or capture probe hybridization. Primer-BLAST²³ was used to analyze secondary structures of lncRNAs to identify regions optimal for primer targeting. Following primer design, the secondary structure of the resulting amplicon was modeled using the Dinamelt web server²² to ensure that has minimal secondary structure at sequence regions targeted by surface capture probes. Examples of amplicon secondary structure analysis and effects of optimization are provided in the Supplemental Information (**Figures 3-2** and **3-3**). In particular, **Figure 3-3** shows that the hybridization response for the optimized β -actin amplicon was improved through this secondary structure-based refinement approach. Following design and optimization, all of the primer pairs were validated using gel electrophoresis to ensure that they selectively produce a single band of appropriate size (**Figure 3-3**).

With primer pairs for the lncRNA targets in hand, we next proceeded to assess the specificity of detection to capture probes arrayed on the sensor chip surface. Four capture probes were spotted onto microrings in each channel of the sensor chip as indicated in **Figure 3-4**. Next, RT-aPCR was separately performed for each target using the healthy brain RNA reference sample. An initial input of 40 ng RNA was used for the RT, followed by 45 aPCR amplification cycles. Each aliquot of the sample, amplified using a single target-specific primer pair, was flowed separately across the functionalized sensor array. As shown in **Figure 3-5**, large positive resonance shifts were observed upon hybridization to ssDNA amplicons to sequence-specific capture probes with minimal non-specific binding.

After verification of aPCR primer sets and sequence specificity for hybridization-based RNA detection, an approach for determining relative target expression was developed. As opposed to smaller targets, such as microRNAs, synthetic target probes cannot be readily synthesized for lncRNAs and therefore we chose to use the commercially obtained healthy brain RNA sample as reference material. RNA targets were separately amplified with primer sets for defined numbers

of cycles and then flowed across the sensor array sequentially with hybridization buffer steps in between. By introducing each amplicon-containing sample as a function of cycle number and increasing hybridization response was observed as each sample of increasing cycle number was flowed. Samples were analyzed every 2 cycles between 30 and 40. No detectable hybridization response was observed at cycle numbers below 30, and signal saturation was achieved beyond 40 cycles under the chosen sample dilution conditions. Samples were flowed across the sensor array for 13 mins allowing for hybridization. The chip was then washed for 2 minutes with hybridization buffer, after which the relative resonance wavelength shift was determined. Responses from control rings were subtracted from the signal of target specific rings (**Figure 3-6A**, red trace). After the buffer rinse, the next higher cycle number sample was flowed across the array. A representative real-time hybridization response for the detection of the lncRNA KIAA0495 is shown in **Figure 3-6A** with data representing the average 16 replicate microring measurements simultaneously made on a single chip.

Similar to traditional qPCR analysis, the resulting calculated net shift induced by ssDNA hybridization was plotted versus the PCR cycle number to enable relative quantitation, as shown for KIAA0495 in **Figure 3-6B**. In order to compare expression between samples, we determined a cycle threshold ($C(t)$) value, again analogous to qPCR.²⁴ To achieve this, the cycle number corresponding to 40% of the maximum resonance shift at high cycle numbers was extrapolated and assigned as the $C(t)$ value from a given sample. Forty percent of the maximum signal was chosen because it was significantly above the noise of the baseline (signal obtained at lower cycles where no DNA is detectable) and also well below saturation.

Having established a method for $C(t)$, which is related to the concentration of a given lncRNA within an unknown sample, we demonstrated the applicability of this combined approach to determine differential expression of these targets in multiple human-derived samples. Samples included two commercially available pooled healthy total RNA samples from brain and lung tissue, and total RNA extracted from a patient-derived xenograft glioblastoma cell line (GBM6). Given their roles in brain cancer, two lncRNAs of potential disease relevance were chosen. KIAA0495/PDAM has been shown to act as a tumor suppressor in oligodendrioglioma.²⁵ MALAT1 (metastasis associated lung adenocarcinoma transcript 1), is a lncRNA that has been studied in different tumors.²⁶ MALAT1 was first studied in the context of NSCLC (non-small cell

lung cancer cell) where it was found that higher expression of the lncRNA correlated with elevated metastasis.²⁷ In glioblastoma, however, MALAT1 can act as a tumor suppressor.²⁸ We also developed primer sets and a capture probe for β -actin, which was used as an input control to correct for any sample processing variability.²⁹

Hybridization response versus cycle number was measured for these three RNA targets in each sample as described above. Following control subtraction, real-time resonance wavelength shifts are shown in Figure 3.7. C(t) values (Table 3.3) were determined from the amplification curves presented in Figure 3.8 and were used to contextualize differences in RNA expression between samples. The internal control, β -actin, was used to normalize the results and correct for initial input of RNA and other variabilities. Expression differences between both lncRNA targets in healthy brain and lung samples were small, and consistent with RT-qPCR measurements, as shown in Figure 3.9A. Both MALAT1 and KIAA were found at slightly lower levels in lung tissue relative to brain, which is consistent with expression values available through the EMBL-EBI Expression Atlas³⁰ (KIAA is indexed as TP73-AS1). Comparison of the GBM6 cell line with healthy brain tissue was more interesting, as lncRNAs have been shown to be differentially expressed in cancer.³¹

Considering lncRNA expression in the GBM6 xenograft cell line, Figure 3.9B again shows consistency between the aPCR- microring and conventional RT-qPCR measurements. KIAA shows minimally higher expression in GBM6 cells compared to healthy brain tissue. However, MALAT1 shows significantly lower expression in the GBM6 sample. This result is interesting given that this lncRNA has previously been found to be downregulated in glioblastoma samples.²⁸ Moreover, while the expression of MALAT1 in GBM 6 cells has not been previously reported, the downregulation of its tumor suppressive actions would be consistent with a malignant phenotype.

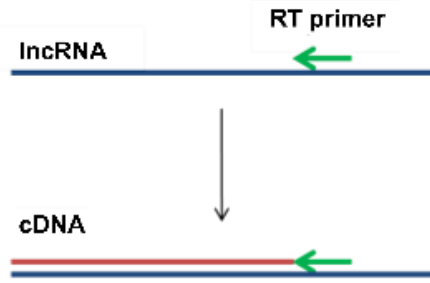
4. Conclusions

Given the continuing emergence of lncRNAs as important regulatory elements associated with many disease phenotypes, the development of analytical methods to characterize their expression from clinically-relevant samples is of high importance. We have demonstrated an integrated analysis approach for multiplexed detection of lncRNAs that leverages the ability for sequence-specific target amplification via asymmetric PCR

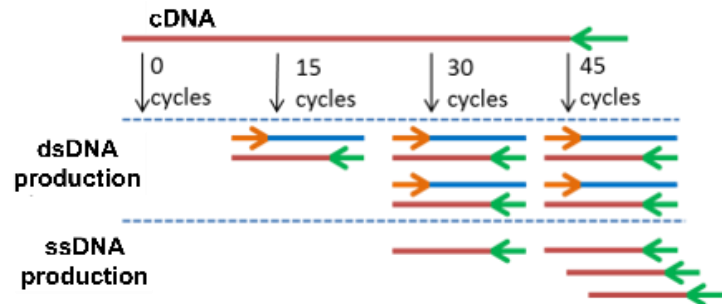
and label-free, spatially-multiplexed hybridization-based detection using silicon photonic microring resonators. We report the design of specific primer sets for the detection of two lncRNAs and found that expression levels determined from healthy brain and lung tissue, as well as a patient-derived xenograft model of glioblastoma, were consistent with both conventional, single-plex RT-qPCR and literature precedent. We also designed primer sets for β -actin mRNA, which was used as a control to normalize for differences in input—a step important for applications with clinical samples. While this proof-of-principle study focused on a detailed discussion of the probe design and validation process for two targets, the multiplexing capacity of microring resonators makes this overall approach suitable for simultaneously probing many more lncRNAs from single samples in the future. Expanded lncRNA panels probed using this approach in the future might reveal new biomarker signatures as well as new fundamental insights into lncRNA actions in disease onset and progression.

FIGURES

A. Reverse Transcription



B. Asymmetric PCR



C. Sample collection and ring hybridization

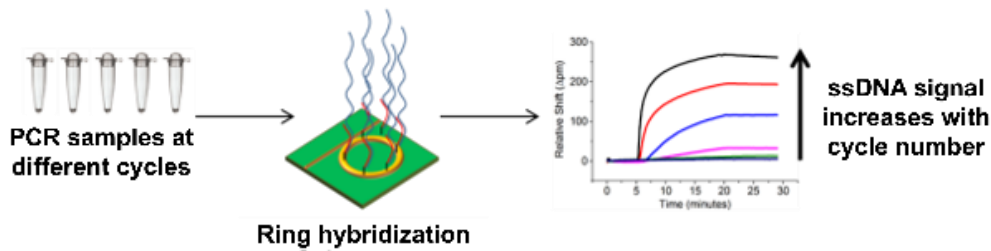


Figure 3-1. Schematic outline of the overall assay for lncRNA detection including (A) reverse transcription, (B) asymmetric PCR, and (C) label-free, hybridization-based detection with microring resonator arrays.

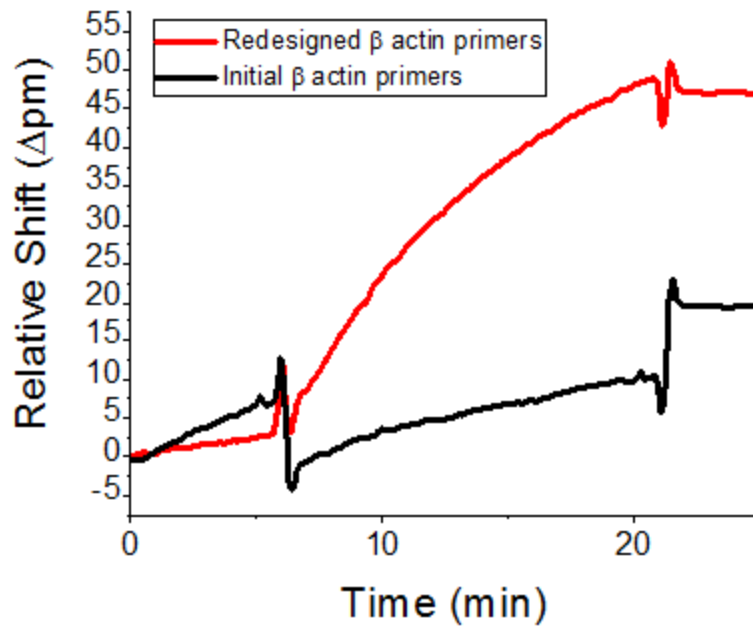


Figure 3-3. Comparison of β -actin PCR product binding with and without optimized primer design. The red trace shows improved binding when using the optimized primer sets (predicted structure shown in in Figure 3.2b). The black trace shows data obtained using the PCR amplicon with a high degree of secondary structure (Figure 3.2A). At $t = 5$ minutes, the solution was changed from hybridization buffer to the amplicon-containing solution, then returned to hybridization buffer at $t = 20$ minutes. The larger positive resonance shift confirmed improved amplification with new primer design.

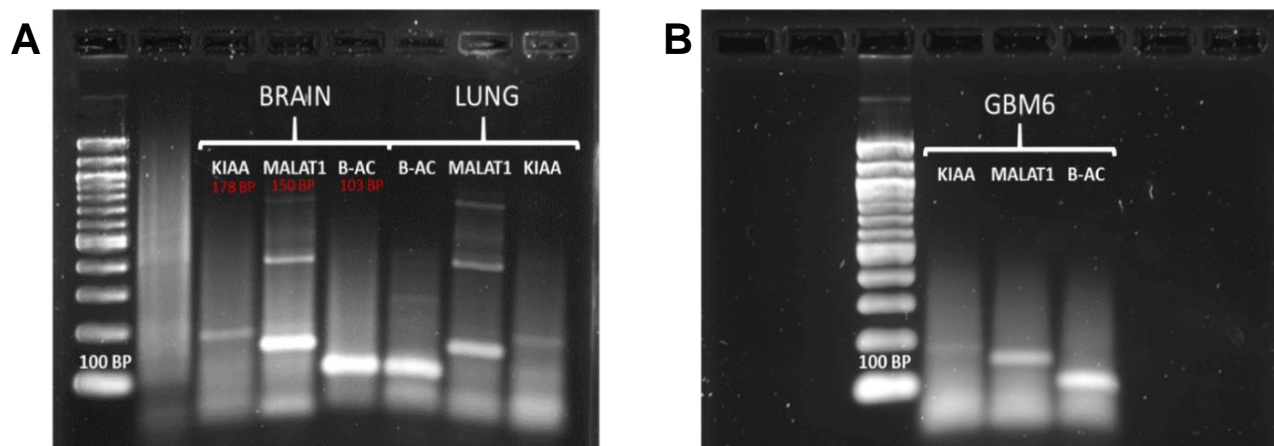


Figure 3-4: Agarose gel electrophoresis (2% agarose; SYBR Gold Stain) used to prove specific PCR amplification of lncRNAs and β -actin in (A) commercial brain and lung RNA samples; and (B) RNA isolated from GBM6 cells.

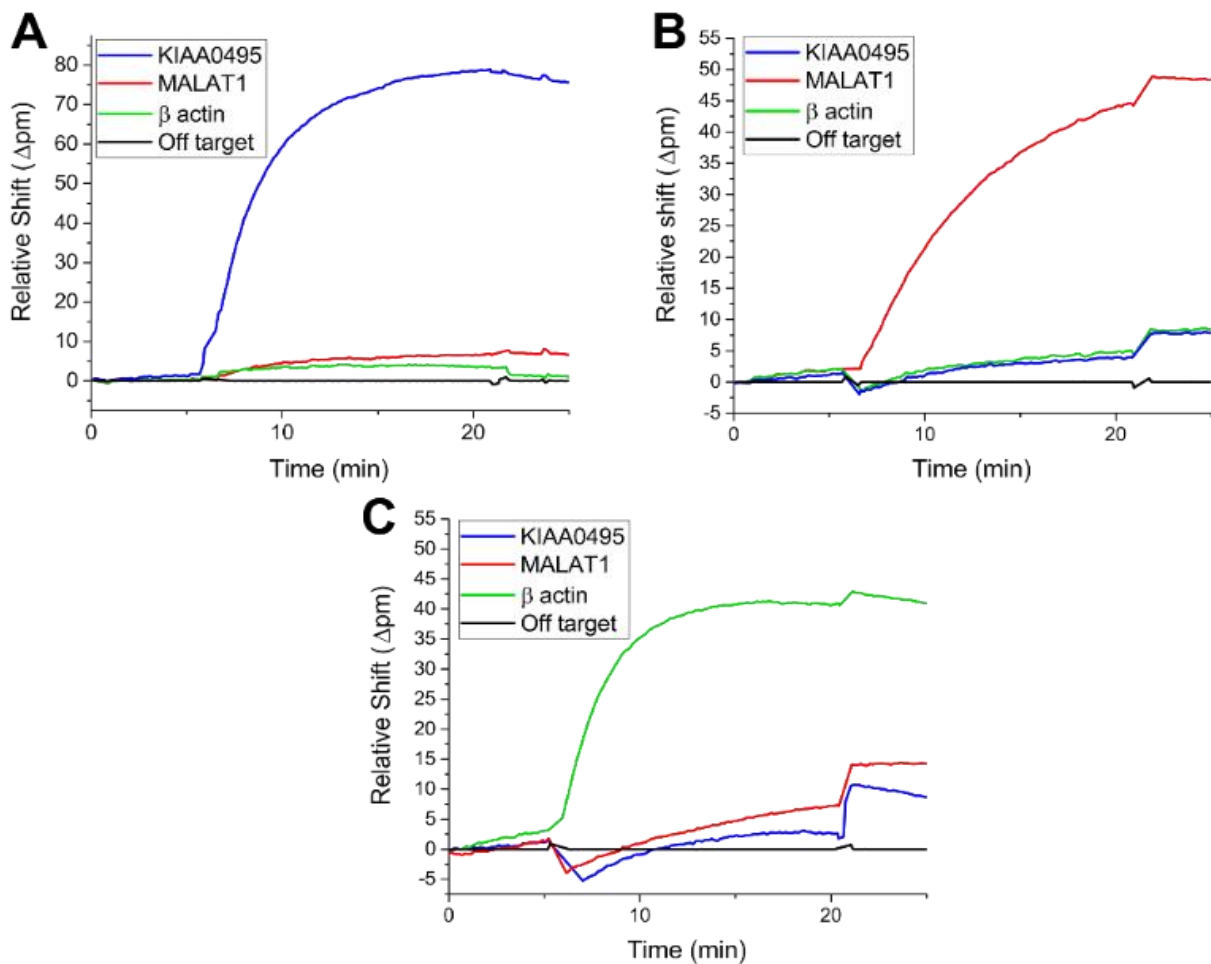


Figure 3-5. Verification of capture probe specificity. Each target was amplified individually in a separate volume of sample and then flowed across a sensor array containing capture probes for all targets. Large, specific hybridization responses were observed at appropriately-functionalized microring sensors for (A) KIAA0495, (B) MALAT1, and (C) β -actin. Buffer was initially flowed across the sensor array before the amplicon solutions were introduced at $t=5$ minutes. The solution was changed back to buffer after hybridization ($t=22$ minutes). Resonance shifts localized only to buffer/sample changes were due to differences in bulk solution refractive index.

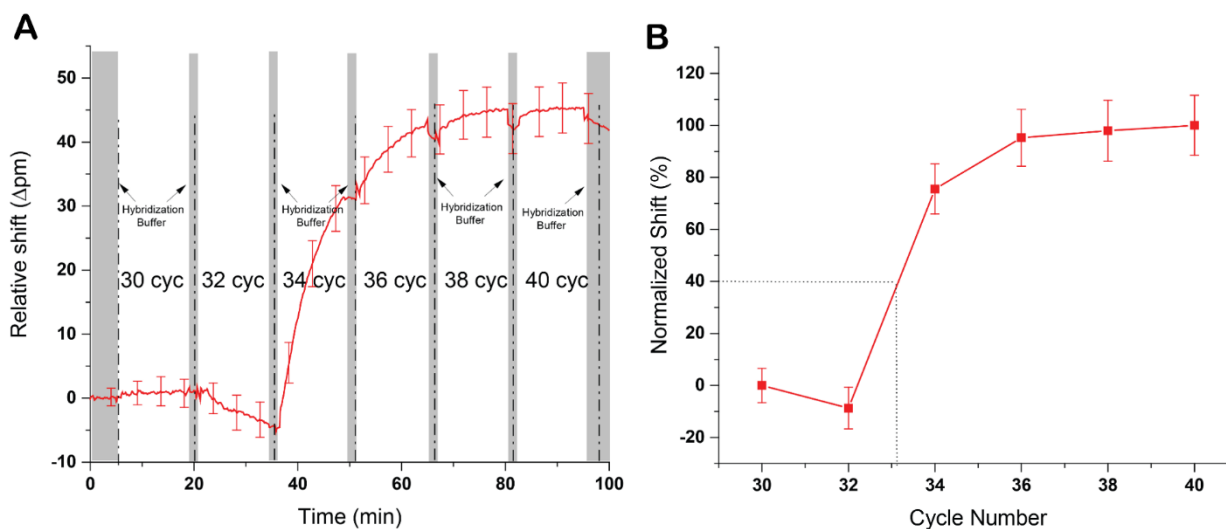


Figure 3-6. (A) Detection of the KIAA0495 aPCR product from healthy brain total RNA at different cycle numbers. The amplicon solutions from each cycle number were sequentially flowed across the sensor array separated by brief returns to hybridization buffer. Real-time resonance wavelength shifts are shown for microrings functionalized with target-specific (red) probes. Increasing hybridization responses are clearly observed with increasing cycle numbers. Error bars represent \pm s.d. from $n=16$ replicate sensors. (B) Normalized hybridization response for KIAA0495 from healthy brain reference RNA as a function of cycle number. A $C(t)$ value was assigned as the cycle number corresponding to 40% of the maximum hybridization response.

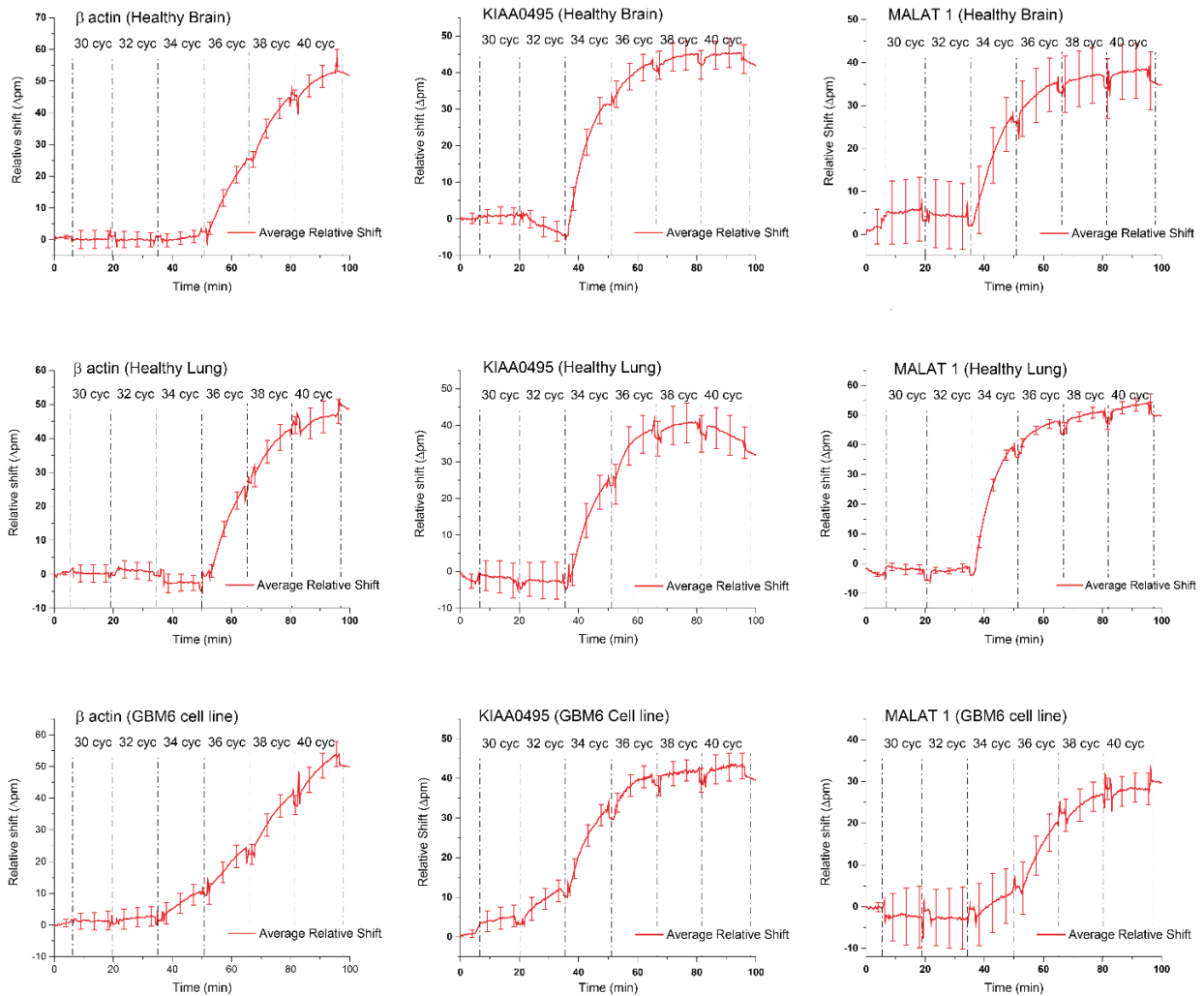


Figure 3-7. Microring traces used to calculate amplification plots in Figure 4. The trace signal represents the average of at least 8 replicate microrings simultaneously measure on the same chip minus the off control signal from non-specific functionalized rings. Error bars represent \pm s.d. for n=8-16 replicate measurements on the same microring sensor array.

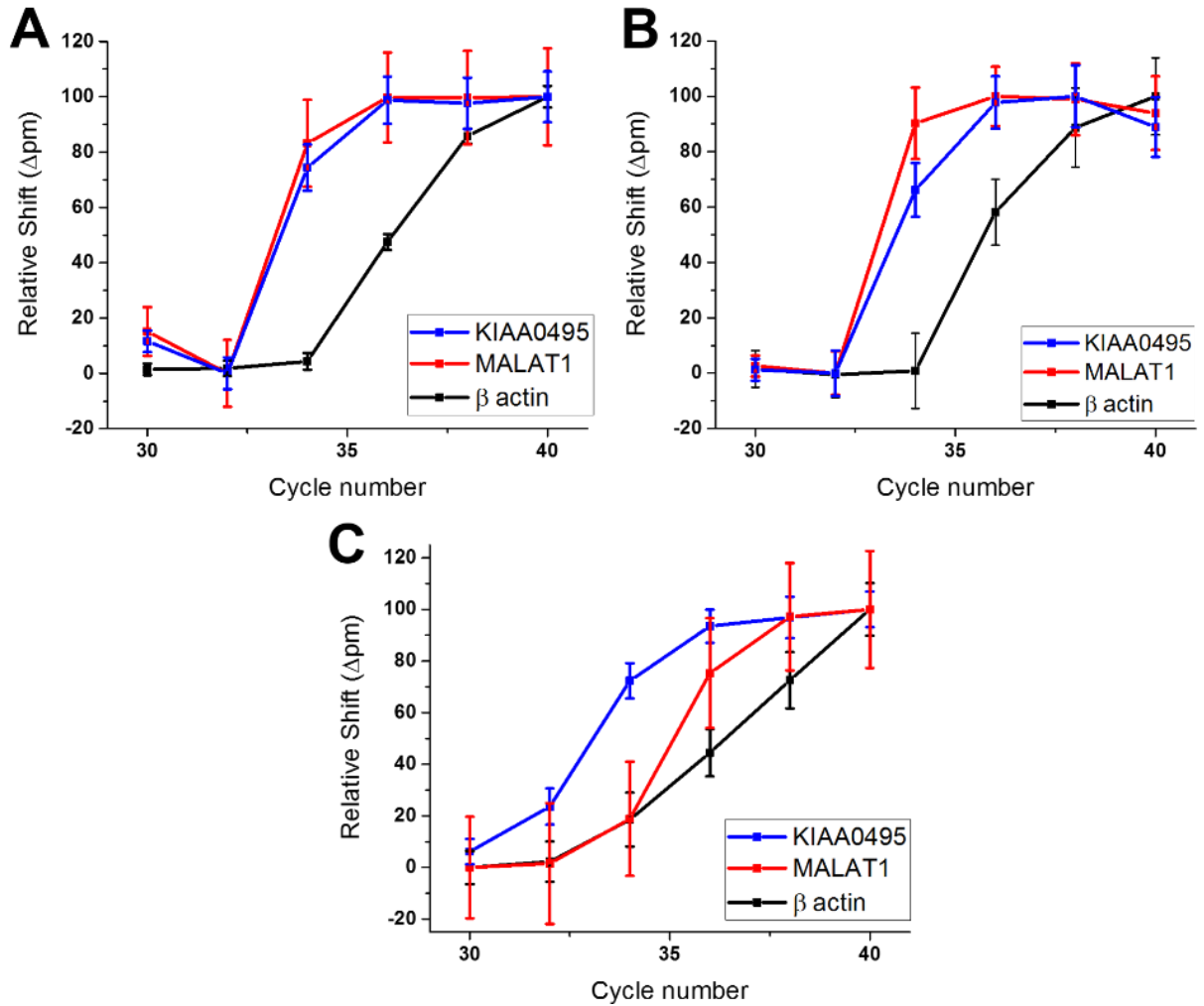


Figure 3-8. Amplification curves for the lncRNAs and internal control target measured (A) Healthy brain total RNA, (B) Healthy Lung total RNA, and (C) total RNA extracted from GBM6 cells, a glioblastoma patient-derived xenograft sample. Error bars represent \pm s.d. from n=8-16 replicate measurements on the same chip.

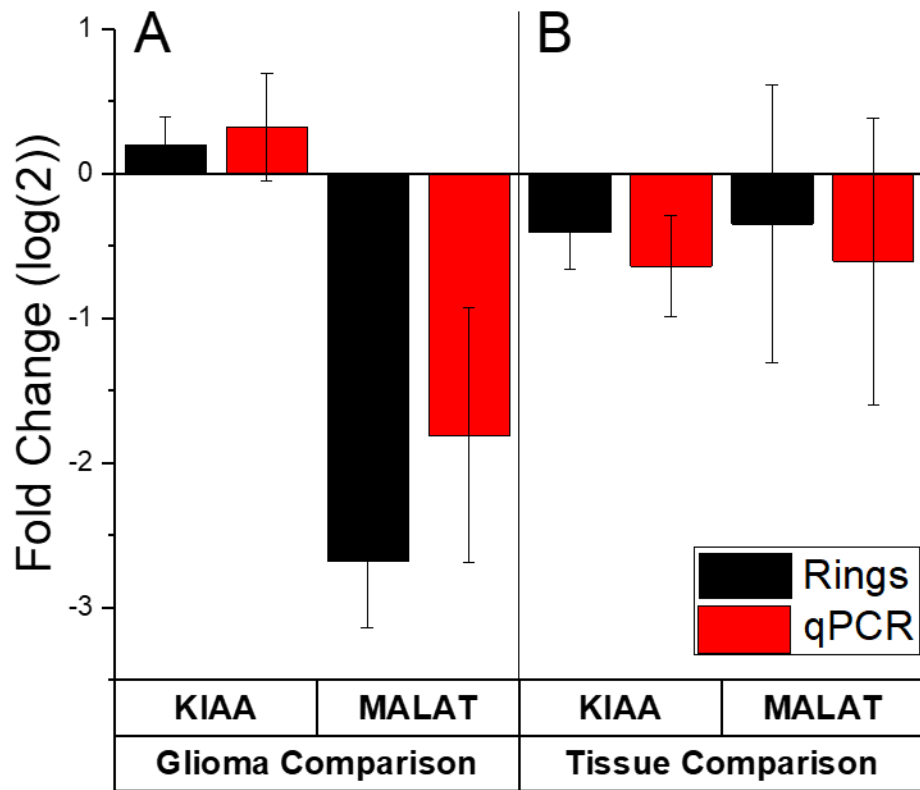


Figure 3-9. Comparison of RNA target fold changes using the combined aPCR-microarray resonator approach relative to conventional, single-plex RT-qPCR. Fold changes were calculated by normalizing to a β -actin internal control. (A) Comparison of lncRNA expression in GBM6 using healthy brain tissue as reference. KIAA showed slightly increased expression in the GBM6 sample, relative to healthy brain, but MALAT showed reduced expression in the xenograft cell line. (B) Comparison of KIAA and MALAT1 expression in healthy lung using brain tissue as reference. Both KIAA and MALAT1 have slightly lower expression in lung tissue, relative to brain.

TABLES

Table 3-1. Primers (RP, reverse primer; FP, forward primer) and capture probes (CP) used in the experiments for reverse transcription (RT), asymmetric PCR, and RT-qPCR. Melting temperatures for primers were calculated using the Primer-Blast platform.

Targeted transcript		Sequence (5' → 3')	T _m (°C)	Amplicon length
KIAA0495	RP (RT primer)	GCTGCTTGCTGTACGTGGTG	62.18	178 nt
	FP	CGTGGCTGACACAACTTGC	60.59	
	CP	/5AmMC12/GCTGCTTGCTGTACGTGGTG		
MALAT1	RP (RT primer)	GTGATGAAGGTAGCAGGCGG	60.81	150 nt
	FP	ACATATTGCCGACCTCACGG	60.18	
	CP	/5AmMC12/GTGATGAAGGTAGCAGGCGG		
β-actin	RP (RT primer)	CATTCCAAATATGAGATGCGTTGT	58.18	103 nt
	FP	TGTGGACTTGGGAGAGGACT	59.81	
	CP	/5AmMC12/CATTCCAAATATGAGATGCGTTGT		
Off Target Control	CP	/5AmMC12/CTACAAGTGCCTTCACTGCAGT		

Table 3-2. Fluidic handling protocol for the ring hybridization steps.

Step	Flow Rate (μL/min)	Duration (min)
Hybridization buffer	20	5
RT-PCR product cycle 30	20	13
Hybridization buffer	20	2
RT-PCR product cycle 32	20	13
Hybridization buffer	20	2
RT-PCR product cycle 34	20	13
Hybridization buffer	20	2
RT-PCR product cycle 36	20	13
Hybridization buffer	20	2
RT-PCR product cycle 38	20	13
Hybridization buffer	20	2
RT-PCR product cycle 40	20	13
Hybridization buffer	20	5

Table 3-3. Calculated qRT-PCR and microring C(t) values from healthy brain, healthy lung and GBM6 RNA samples. The RNA input for qRT-PCR experiments was 40 ng, and the qRT-PCR experiments were completed in triplicate.

RNA	Target	qRT-PCR C(t)	Rings C(t)	qPCR Fold change (log ₂)**	Rings Fold change (log ₂)**
Brain	B actin	17.40 ± 0.25	35.65 ± 0.32	-	-
	KIAA0495	21.16 ± 0.18	33.09 ± 0.19	-	-
	MALAT1	15.77 ± 0.46	33.04 ± 0.32	-	-
Lung	B actin	17.40*	35.65* ± 0.76	0 ± 0.39	0 ± 0.82
	KIAA0495	21.57*	33.44* ± 0.29	- 0.41 ± 0.25	- 0.64 ± 0.35
	MALAT1	16.38*	33.68* ± 0.91	- 0.61 ± 0.99	- 0.35 ± 0.96
GBM 6	B actin	17.40* ± 0.04	35.65* ± 0.73	0 ± 0.04	0 ± 0.79
	KIAA0495	21.36* ± 0.07	32.72* ± 0.32	0.20 ± 0.19	0.32 ± 0.37
	MALAT1	19.05* ± 0.05	34.90* ± 0.83	-2.68 ± 0.46	-1.81 ± 0.88

* Corrected signal with internal control

** Healthy brain as reference; Fold Change = $C(t)_{ref} - C(t)_{sample}$

BIBLIOGRAPHY

- (1) Byron, S. A.; Van Keuren-Jensen, K. R.; Engelthaler, D. M.; Carpten, J. D.; Craig, D. W. Translating RNA Sequencing into Clinical Diagnostics: Opportunities and Challenges. *Nat. Publ. Gr.* **2016**, *17*, 257-271.
- (2) Qi, P.; Du, X. The Long Non-Coding RNAs, a New Cancer Diagnostic and Therapeutic Gold Mine. *Mod. Pathol.* **2013**, *26* (2), 155–165.
- (3) Mattick, J. S.; Makunin, I. V. Non-Coding RNA. *Hum. Mol. Genet.* **2006**, *15* (90001), R17–R29.
- (4) Bartolomei, M. S.; Zemel, S.; Tilghman, S. M. Parental Imprinting of the Mouse H19 Gene. *Nature* **1991**, *351* (6322), 153–155.
- (5) Baker, M. Long Noncoding RNAs: The Search for Function. *Nat. Publ. Gr.* **2011**, *8* (5), 379-383.
- (6) Fatica, A.; Bozzoni, I. Long Non-Coding RNAs: New Players in Cell Differentiation and Development. *Nat. Publ. Gr.* **2013**, *15*, 7-21.
- (7) Rinn, J. L.; Chang, H. Y. Genome Regulation by Long Noncoding RNAs. *Annu. Rev. Biochem.* **2012**, *81* (1), 145–166.
- (8) Gibb, E. A.; Brown, C. J.; Lam, W. L. The Functional Role of Long Non-Coding RNA in Human Carcinomas. *Mol. Cancer* **2011**, *10* (1), 38.
- (9) Prensner, J. R.; Chinnaiyan, A. M. The Emergence of LncRNAs in Cancer Biology. *Cancer Discov.* **2011**, *1* (5), 391–407.
- (10) Zhang, X.; Sun, S.; Pu, J. K. S.; Tsang, A. C. O.; Lee, D.; Man, V. O. Y.; Lui, W. M.; Wong, S. T. S.; Leung, G. K. K. Long Non-Coding RNA Expression Profiles Predict Clinical Phenotypes in Glioma. *Neurobiol. Dis.* **2012**, *48* (1), 1–8.

- (11) Zhang, X.-Q.; Sun, S.; Lam, K.-F.; Kiang, K. M.-Y.; Pu, J. K.-S.; Ho, A. S.-W.; Lui, W.-M.; Fung, C.-F.; Wong, T.-S.; Leung, G. K.-K. A Long Non-Coding RNA Signature in Glioblastoma Multiforme Predicts Survival. *Neurobiol. Dis.* **2013**, *58*, 123–131.
- (12) Graybill, R. M.; Bailey, R. C. Emerging Biosensing Approaches for MicroRNA Analysis. *Anal. Chem.* **2016**, *88* (1), 431–450.
- (13) Pritchard, C. C.; Cheng, H. H.; Tewari, M. MicroRNA Profiling: Approaches and Considerations. *Nat. Rev. Genet.* **2012**, *13* (5), 358–369.
- (14) Iqbal, M.; Gleeson, M. A.; Spaugh, B.; Tybor, F.; Gunn, W. G.; Hochberg, M.; Baehr-Jones, T.; Bailey, R. C.; Gunn, L. C. Label-Free Biosensor Arrays Based on Silicon Ring Resonators and High-Speed Optical Scanning Instrumentation. *IEEE J. Sel. Top. Quantum Electron.* **2010**, *16* (3), 654–661.
- (15) Washburn, A. L.; Gunn, L. C.; Bailey, R. C. Label-Free Quantitation of a Cancer Biomarker in Complex Media Using Silicon Photonic Microring Resonators. *Anal. Chem.* **2009**, *81* (22), 9499–9506.
- (16) Qavi, A. J.; Bailey, R. C. Multiplexed Detection and Label-Free Quantitation of MicroRNAs Using Arrays of Silicon Photonic Microring Resonators. *Angew. Chemie Int. Ed.* **2010**, *49* (27), 4608–4611.
- (17) Graybill, R. M.; Para, C. S.; Bailey, R. C. PCR-Free, Multiplexed Expression Profiling of MicroRNAs Using Silicon Photonic Microring Resonators. *Anal. Chem.* **2016**, *88* (21), 10347–10351.
- (18) Kindt, J. T.; Bailey, R. C. Chaperone Probes and Bead-Based Enhancement to Improve the Direct Detection of mRNA Using Silicon Photonic Sensor Arrays. *Anal. Chem.* **2012**, *84* (18), 8067–8074.
- (19) Scheler, O.; Kindt, J. T.; Qavi, A. J.; Kaplinski, L.; Glynn, B.; Barry, T.; Kurg, A.; Bailey, R. C. Label-Free, Multiplexed Detection of Bacterial TmRNA Using Silicon Photonic Microring Resonators. *Biosens. Bioelectron.* **2012**, *36* (1), 56–61.
- (20) Gyllensten, U. B.; Erlich, H. A. Generation of Single-Stranded DNA by the Polymerase

- Chain Reaction and Its Application to Direct Sequencing of the HLA-DQA Locus. *Proc. Natl. Acad. Sci. U. S. A.* **1988**, *85* (20), 7652–7656.
- (21) Sanchez, J. A.; Pierce, K. E.; Rice, J. E.; Wang, L. J. Linear-After-The-Exponential (LATE)–PCR: An Advanced Method of Asymmetric PCR and Its Uses in Quantitative Real-Time Analysis. *Proc. Natl. Acad. Sci.* **2004**, *101* (7), 1933–1938.
- (22) Markham, N. R.; Zuker, M. DINAMelt Web Server for Nucleic Acid Melting Prediction. *Nucleic Acids Res.* **2005**, *33* (Web Server), W577–W581.
- (23) Ye, J.; Coulouris, G.; Zaretskaya, I.; Cutcutache, I.; Rozen, S.; Madden, T. L. Primer-BLAST: A Tool to Design Target-Specific Primers for Polymerase Chain Reaction. *BMC Bioinformatics* **2012**, *13* (1), 134.
- (24) Schmittgen, T. D.; Livak, K. J. Analyzing Real-Time PCR Data by the Comparative C(T) Method. *Nat. Protoc.* **2008**, *3* (6), 1101–1108.
- (25) Pang, J. C.-S.; Li, K. K.-W.; Lau, K.-M.; Ng, Y. L.; Wong, J.; Chung, N. Y.-F.; Li, H.-M.; Chui, Y.-L.; Lui, V. W. Y.; Chen, Z.; et al. KIAA0495/PDAM Is Frequently Downregulated in Oligodendroglial Tumors and Its Knockdown by SiRNA Induces Cisplatin Resistance in Glioma Cells. *Brain Pathol.* **2010**, *20* (6), 1021–1032.
- (26) Wu, Y.; Huang, C.; Meng, X.; Li, J. Long Noncoding RNA MALAT1: Insights into Its Biogenesis and Implications in Human Disease. *Curr. Pharm. Des.* **2015**, *21* (34), 5017–5028.
- (27) Ji, P.; Diederichs, S.; Wang, W.; Böing, S.; Metzger, R.; Schneider, P. M.; Tidow, N.; Brandt, B.; Buerger, H.; Bulk, E.; et al. MALAT-1, a Novel Noncoding RNA, and Thymosin B4 Predict Metastasis and Survival in Early-Stage Non-Small Cell Lung Cancer. *Oncogene* **2003**, *22* (39), 8031–8041.
- (28) Han, Y.; Wu, Z.; Wu, T.; Huang, Y.; Cheng, Z.; Li, X.; Sun, T.; Xie, X.; Zhou, Y.; Du, Z. Tumor-Suppressive Function of Long Noncoding RNA MALAT1 in Glioma Cells by Downregulation of MMP2 and Inactivation of ERK/MAPK Signaling. *Nat. Publ. Gr.* **2016**, *7*, e2123.

- (29) Thellin, O.; Zorzi, W.; Lakaye, B.; De Borman, B.; Coumans, B.; Hennen, G.; Grisar, T.; Igout, A.; Heinen, E. Housekeeping Genes as Internal Standards: Use and Limits. *J. Biotechnol.* **1999**, *75* (2–3), 291–295.
- (30) Petryszak, R.; Keays, M.; Tang, Y. A.; Fonseca, N. A.; Barrera, E.; Burdett, T.; Füllgrabe, A.; Fuentes, A. M.-P.; Jupp, S.; Koskinen, S.; et al. Expression Atlas Update—an Integrated Database of Gene and Protein Expression in Humans, Animals and Plants. *Nucleic Acids Res.* **2016**, *44* (D1), D746–D752.
- (31) Kiang, K.; Zhang, X.-Q.; Leung, G. Long Non-Coding RNAs: The Key Players in Glioma Pathogenesis. *Cancers (Basel)*. **2015**, *7* (3), 1406–1424.

CHAPTER IV

Dynamic profiling of miRNA and phosphoproteins in PDX derived cell lines under different treatments using silicon photonic microring resonators

Acknowledgments

I would like to acknowledge the contributions of Dr. Richard Graybill and Dr. James Wade for their guidance and help in the analysis of the miRNA panels. I would also like to acknowledge Jann Sarkaria from Mayo Clinic for PDX Glioblastoma cell lines and Colleen Riordan for passaging the cells, performing the treatments and cell lysis.

Abstract

MicroRNAs are known to be essential regulators of many critical biological processes, and deregulation of their normal expression patterns have been identified in a host of diseases. Here, we aim to study changes in microRNA expression patterns in response to targeted treatments using glioblastoma as a model system. We have identified a panel of eight microRNAs that are known to play a vital role in glioblastoma progression. Profiling of these targets is completed in cultured patient-derived xenografts treated with three therapies for differing amounts of time. To compile expression profiles, RNA was isolated from the samples of interest and subjected to Reverse Transcription-Asymmetric Polymerase Chain Reaction (RT-aPCR). The RT-aPCR products are detected by a silicon photonic microring resonator platform, a thoroughly validated and multiplexable technology. Each microring biosensor chip consists of an array of 32 clusters of microrings that can be individually functionalized, allowing multiplex detection of RNAs. By coupling RT-aPCR to the biosensor platform, we can relate the biosensor response to target expression levels in the sample to achieve the detection of very low amounts of nucleic acids.

Importantly, we can then use the changes in microRNA expression patterns presented here to inform treatment efficacy and to design better therapeutics in the future.

1. Introduction

Glioblastoma is the most frequent type of primary brain tumors and one of the most aggressive cancers. Although a lot effort has been invested in the development of new therapies and diagnostics, there is not yet an effective cure in the market and the general prognosis is about 15 months of survival after treatment¹. The current standard treatment is resection of the tumor followed by temozolomide, an alkylating agent that adds methyl groups to purine and pyrimidine in DNA². However, more than half of the patients are resistant to this drug, and consequently, researches are trying to develop more personalized therapeutic approaches by matching the patient molecular profile with the right drug³. The occurrence of GBM is usually associated with mutation or overexpression of the epidermal growth factor receptor, EGFR, and the phosphatidylinositol 3-kinase (PI3K)/Akt/rapamycin-sensitive mTOR-complex (mTOR) pathways⁴. The PI3K/Akt/mTOR is a pathway commonly upregulated in many solid tumors, and it has been mainly studied in glioblastoma as a susceptible route to target the different treatments.

Due to the difficulty of the extraction of tissue samples from patients, the development of study models has been crucial in the study of the glioblastoma. The current preclinical glioblastoma models are divided into three categories: xenografts, genetically engineered mouse models and syngenic murine models⁵. In the xenograft models, the human tumor cells are transplanted under the skin or into the organ of immunocompromised mice. These models are beneficial to understand the effect of tumor microenvironments on the tumor progression with or without treatment⁶. Xenografts can be produced using commercially available Glioblastoma cell lines (such as U87, U251, T98G, and A172) or using tumors cells directly from the patients, also known as Patient-Derived Xenografts (PDX). These kind of models have the advantage of retaining histological and genetic features of the original tumor, and so they could aid to the development of personalized therapeutic approaches.

Personalized therapeutic approaches are about matching the patient profile with the right drug. There have been many reports of how miRNA could be used in personalized medicine in diagnostics, disease progression, or therapeutic effect⁷. MiRNAs are short noncoding RNA

sequences of 22 nucleotides involved in the regulation of gene expression⁸. They function by binding full or partial complementary mRNA sequences. This recognition produces the binding of other proteins that cleave the mRNA or destabilize the translation complex. One of the limitations of using single miRNAs as biomarkers is the lack of specificity with the disease. The regulation of expression by miRNA is somewhat complicated because one miRNA can target several mRNAs and different miRNAs can target the same mRNA⁹. It is therefore essential to focus on the expression analysis of miRNA panels in order to identify signatures that could diagnose the disease, classify the subtypes or predict the outcome of the therapies¹⁰⁻¹³. When studying miRNA regulation, it is very informative to visualize their expression over time under certain stimuli. Studies have reported “snapshots” of gene expression under different conditions over the time. Such is the case of the study published by Susanne Reinsbach et al. where they investigated the expression of miRNA after the activation of a transcription factor by IFN gamma¹⁴. They employed different biostatistical approaches to gain insight into the biological network that took place after the activation. They found that miRNA were more significantly upregulated or downregulated after 24 hours of treatment, with fold changes larger than 7.0. With the biostatistical analysis, they were able to discover groups of miRNA that seemed co-regulated.

miRNA are conventionally detected and quantified by northern blots, microarrays, and qPCR^{15,16}. Also, thanks to the advancements in next-generation sequencing, RNA sequencing has been more permissive for the quantification and discovery of these transcripts¹⁷. Opposite to other RNA sequences, miRNAs have some challenges because of their short sequence, their similarity between miRNAs from the same family and the distinction between pre mature and mature forms. To overcome those challenges, people have created different strategies¹⁵. For example, in qPCR, researchers have designed stem-loop probes that contain an overhang to allow hybridization of miRNA in reverse transcription and provide a more extended sequence for future primer amplification in PCR¹⁸. Similar to this strategy, our lab combined the stem-loop recognition with asymmetric amplification (aPCR) in order to produce single-stranded DNA (ssDNA) that could be bound to capture probes on top of microring resonators¹⁹. This strategy that was described in chapters two and three was also used in this study for the miRNA expression measurements.

Our study aimed to dynamically profile a panel of miRNA to aid in the identification of susceptible pathways and targets of glioblastoma. For the profiling, we used two GBM cell lines

originated from GBM PDX that were exposed to three different protein inhibitors in the EGFR-mTOR pathway. After measuring the miRNA at different times after inhibitor exposure, exploratory statistical analyses were performed on the results to identify which of the targets had more expression variability. The final goal of this study is the ability to identify miRNA signatures associated with the different treatments, and then, use these signatures to evaluate the effectiveness of the treatments in the different patients. Future work will be to combine these signatures with the proteomic signatures to describe therapeutic effect with more precision.

2. Methodology

Materials

Dacomitinib, buparlisib, and dactolisib were purchased from MedChem Express. The nucleic acid sequences were purchased from Integrated DNA Technologies (IDT; Coraville, IA). The sequences can be seen in **Table 4-1**. The TaqMan® microRNA Reverse Transcription Kit and the Platinum® Multiplex PCR Master Mix were purchased from Thermo Fisher. Nuclease-free ultrapure water was purchased from Invitrogen. For the hybridization of the amplified sequences, a high stringency hybridization buffer was made (30 % formamide (Fisher), 0.2 % sodium dodecyl sulfate (Fisher), 5% 20X saline-sodium citrate buffer (Invitrogen), 30 mM EDTA (Invitrogen), and 5% 50X Denhardt solution (Invitrogen)).

Cell culture, treatments, and RNA isolation

The GBM PDX cultures were established as in the work of Carlson et al²⁰. Then, cell cultures were derived from these xenografts and grown in DMEM media with 10 % fetal bovine serum (FBS). The cells were only passaged twice before treatment. The treatments consisted of three molecules: dacomitinib (EGFR inhibitor), buparlisib (BKM120) (PIK3 inhibitor) and dactolisib (BEZ235) (PI3K/mTOR) inhibitor (**Table 4-2**). The treatments were dissolved in DMSO and added to the medium to a final concentration of 1 uM. For this study, we used two controls: DMEM with 10 % FBS and DMEM with 0.1 % DMSO. The cells for the different treatments were lysed at 0h, 1h, 12h, 24h and 48h using Cell Lysis Buffer (Cell Signaling Technology) and kept at -80C. Total RNA was extracted from lysates using a miRNeasy ®Mini kit (Quiagen) using manufacture's protocol. Total RNA extracted was quantified using Nanodrop and also checked for quality.

Instrumentation and sensing principles

Maverick M1 and microring array substrates were purchased from Genalyte Inc. Details about the instrument have been described in the previous chapters and elsewhere^{21,22}. Briefly, the substrates sensors are 4 mm by 6 mm in size and are fabricated on silicon on insulator wafers by photolithography and etching techniques. The final sensor array is covered by a fluoropolymer coating with open windows for the active microring elements. On each sensor, 132 individually addressable rings can be functionalized in a cluster of 4 microrings for multiplexed analysis. Grating couplers and waveguides guide the light from a tunable laser on the microring cavities. Specific wavelengths, known as resonant wavelength, can couple to the rings when the resonant conditions are met: $m\lambda = 2\pi r n_{\text{eff}}$; where m is an integer number, λ is the resonant wavelength, r is the radius of the microring (30 μm), and n_{eff} is the effective refractive index of the microring. The binding of the molecules to the microrings can be assessed by the evanescent field from the light coupled to the rings. The change of the refractive index in the surface by the binding events produces a change in the resonant wavelength, and this is the signal the instrument measures over time in units of the shift in picometers (Δpm).

The instrument is equipped with automatic fluidic handling. The sensors chip are loaded into a fluidic cartridge with a gasket that directs the flow of the solution across the array in two different channels. The fluid flow is controlled by integrated syringe pumps under software control.

Reverse transcription and asymmetric PCR

Reverse transcription (RT) and asymmetric PCR (aPCR) were conducted as described in chapter 2 using a TaqMan microRNA Reverse transcription kit and a Platinum Multiplex PCR Master Mix. For the RT, 40 ng of total RNA were combined with 4.16 μL RNase free water, 1.5 μL RT buffer, 1 μL Multiscribe™ transcriptase, 0.19 μL RNase inhibitor and 0.15 μL of 100 M dNTP mix. The concentration of the stem-loops is 20 μM for each primer. The reaction is completed at 16°C (30 min), 42°C (30 min) and 85°C (5 min).

For the aPCR, 14 μL water, 25 μL of Platinum Multiplex PCR Master Mix, 5 μL of each primer and 1 μL of the reversed transcription product were mixed. In aPCR, the concentration of the forward primer (limiting reagent) was 2 μM while the concentration of the reverse primer was 200 μM . The thermal profile of the reaction was: 95°C for 2 min, and then cycles of 95°C for 30

s, 56°C for 1 min 30s, and 72°C for 1 min. aPCR samples were taken every five cycles for measuring the amount of amplified DNA.

Ring hybridization

The 50 µL of the aPCR reactions were mixed with 350 µL the hybridization buffer previously described in the materials section. The mixture was flown over the surface at 20 µL/min for 15 min followed by a 2 min rinse with the hybridization buffer before the introduction of the next sample. All the amplification reaction from the same sample were analyzed on the same chip.

miRNA quantification analysis and statistical analysis

The analysis of the microring signal and the statistical analysis were processed with Origin 2017 (OriginLab, Northampton, MA). First, the sensor traces were thermally corrected. The net shifts and standard deviations for each of the aPCR samples were calculated by subtracting the initial baseline buffer signal from the buffer signal after hybridization. When all the net shifts were calculated, we plotted the net shifts versus the PCR cycle for every target and fitted the points to a logistic curve. The C(t) was calculated by determining the cycle point in the curve at 40% of the maximum signal²³.

To calculate the normalized expression, we used the mean expression value of all expressed microRNAs in a given sample^{24,25}. The fold difference of each transcript in each sample compared to the mean can be calculated as $2^{-(C(t)_{\text{transcript}} - C(t)_{\text{average mean}})}$. Then, these fold changes were used to plot the heatmaps for the different treatments and cell lines. We also used the normalized expression to do principal component analysis (PCA) and to make comparisons of the treatments in the same cell lines and between the two cell lines.

3. Results and discussion

The study used PDX GBM from the resected primary tumor of patients that could be then kept for short periods as xenograft cell cultures (**Figure 4-1.A**). We used two established xenograft cell lines previously characterized in other studies^{26,27}. These cell lines were subjected to three clinically-relevant targeted therapeutics: dacomitinib, buparlisib - BKM120, and dactolisib - BEZ235 (**Figure 4-1.B**). The procedure to analyze the miRNA panels can be observed in **Figure**

4-2 and has been extensively explained in chapter two and three. Briefly, miRNAs extracted from lysed cells are reversed transcribed using specific stem-loop primers for the sequences we chose to detect. After obtaining the cDNAs of the desired molecules, we perform asymmetric PCR, aCPR. aPCR consists of changing the ratio in the amplification primers, having a limiting amount of one of them^{28,29}. When the amount of the limiting primer is exhausted, there is no more double-stranded (dsDNA) production and single-stranded (ssDNA) is then made. Samples at different amplifications are collected and hybridized on pre-spotted probes on the microring sensors. Based on the signal of the rings at the different amplification cycles, we can make amplification curves (**Figure 4-3**) and use them to calculate the threshold cycles (C(t)) similarly to conventional qPCR, but setting the threshold at 40% of the maximum signal.

In order to normalize the results, it has been proved that the global mean normalization method can offer more accurate results for the appreciation of biological variance than including other reference genes²⁴. This method consists of defining the relative expression of the miRNAs by using either the mean or the mean expression value of all expressed miRNAs or the mean of the most stable RNA controls. In our case, we defined the mean C(t) of all measured miRNAs in each sample and then subtracted those means to the respective C(t) values. Heatmaps and PCA analysis were constructed with those values and results are evaluated in the following paragraphs.

3.1. Cell lines characteristics and miRNA panel

The two cell lines used in this study were GBM6 and GBM10^{26,27}. These cell lines have been characterized in previous studies mainly for mutations that can make them insensitive for some of the treatments. GBM6 contains amplification of EGFR mutation referred to as EGFRvIII that involves the deletions of exons 2 through 7. This mutation is frequently observed in GBM and is related to the limited efficacy of treatments with EGFR-tyrosine kinase inhibitors³⁰. In comparison, GBM10 has no mutation of EGFR.

The panel of miRNA used in the study and possible roles in GBM are described in **Table 4-3**. The miRNAs in these panels have been defined to have critical roles in the progression of the gliomas: some of them are usually upregulated with oncogenic properties (miR 10b, miR 335, miR 222 and miR 155), and others act as tumor suppressor genes (miR let 7f, miR 29a, miR 106a, and miR 124a). **MiR let 7f** has been reported to have lower expression in gliomas compared to the healthy brain tissue, and its upregulation is linked to inhibition of glioma cell proliferation in

vivo.³¹ **MiR 29a** has been reported to be upregulated by the EGFR pathway but at the same time acts as a tumor suppressor by the repression of essential genes involved in the cell proliferation.^{32,33} **MiR 106a** levels have been related with both cases: oncogenic roles involving the promotion of invasiveness of human glioma³⁴, and tumor suppression functions related to inhibition of proliferation by targeting E2F1.³⁵ **MiR 124a** is a miRNA related to neuronal differentiation. It is usually downregulated in GBM suggesting that it acts as a tumor suppressor by targeting cyclin-dependent kinase 6 and arresting the cell cycle.³⁶ **MiR 10b** is related to proliferation and survival of glioma cells and is highly expressed in all GBM subtypes.³⁷ **MiR 335** has been described as an anti-apoptotic miRNA with the potential tumor suppressor DAAM1.³⁸ **MiR 222** is usually upregulated in various types of malignancies and has been described as inducing the cell survival of GBM cells by also targeting apoptotic genes.^{39,40} **MiR 155** can be considered as an oncogene because it activates the NFkB pathway and inhibition of GABA receptors.⁴¹

3.2. Serum and DMSO control over time

For the study of the miRNA signatures, we needed to use controls without the treatments. We used two conditions, the media supplemented with the serum and the media supplemented with DMSO. DMSO was used to dissolve the treatments, and so we wanted to observe if DMSO had some effect in the cells, although there have been studies that claim that 10% DMSO did not produce a significant cellular alteration.⁴² Heatmaps from the two cell lines in serum and DMSO can be observed in **Figure 4-4**. Comparing the results from serum to DMSO, the only noticeable change is that miR 155 (usually described as an oncogene and proliferation promoter⁴¹) seems upregulated in the DMSO compared to the serum samples. Comparing both cell lines we can observe that GBM 10 has downregulated miR 222 and 335 (two oncogenes) and the DMSO treatment in these cell lines seems to increase the expression of (let 7f, 10b, and 29a).

3.3. Dacomitinib treatment over time

Dacomitinib is an inhibitor of EGFR. GBM6 has a mutation in EGFR that makes the cell line insensitive to EGFR inhibitor treatments^{26,30}. Comparing the differences in the miRNA profiling for the two cell lines (**Figure 4-5**), we can observe that there is an increase in the expression of miRNAs in GBM10 after 24h (miR 124a and 106a, tumor suppressors) while in GBM6 there is an increase in miR 222 and miR 335 (oncogenes) and a decrease of 124a, 106a, and 29a (tumor suppressors). These results might suggest that GBM6 cells show more proliferative behavior than

GBM10. The results from GBM10 are very similar to the results with DMSO and no serum, but different from the serum results, that might be indicative that the cells stop proliferating and start apoptotic routes.

3.4. Buparlisib treatment over time

Buparlisib (BKM120) is an oral-PI3K inhibitor whose efficacy has been studied especially in patients with PTEN loss. It is in clinical trials for several solid tumors and has manifested anti-proliferative and anti-apoptotic effects in GBM independent of PTEN or EGFR status⁴³. The heatmaps for the dynamic miRNA expression under buparlisib treatment can be visualized in **Figure 4-6**. In GBM6, results are very similar to the results obtained with Dacomitinib treatment (upregulation after 24h of miR222 and 335) and downregulation of 124a, 106a, and 29a. Similarly, the results in GBM10 are very similar to the ones obtained with Dacomitinib (upregulation of 124a and 106a) and downregulation of 10b (oncogene). Again, that might be suggestive of the most apoptotic behavior of GBM10.

3.5. Dactolisib treatment over time

Dactolisib (BEZ235) is a dual PI3K/mTOR inhibitor that has shown promising anti-neoplastic activity in different solid tumors.⁴⁴ Again, the results from GBM6 seem very similar to the previous treatments (**Figure 4-7**) (upregulation of miR 222 and miR 335, and downregulation of miR 124a, 106a, and 29a). In GBM10, the expression is also similar compared to the previous treatments, although miR 124a seems more downregulated this time.

3.6. Treatment comparison at 1h, 12h, 24h and 48h.

Treatments comparisons over time can be observed in **Figure 4-8**. Just doing an exploratory visualization, it can be realized that there are not many significant differences between the treatments. However, there is a discernible pattern of expression of miRNAs over time. GBM6 (**Figure 4-8A**) miRNA expression indicates no difference between the DMSO and the treatments. Unique observations are the upregulation of miR 335, miR 222 and miR 155 in all the samples. These transcripts are miRNAs that act as oncogenes, so the fact that they get upregulated over the time might be indicative of the lack of the effectiveness of the treatments in this cell line. MiR 106a, that acts as tumor suppressor, also seems downregulated over the 24h also indicating that the treatment is not being very effective. On the other hand, GBM10 (**Figure 4-8B**) exhibits low

expression of miR 335 and 222 (oncogenic miRNAs) and upregulation of 124a and 106a after 24h. That might be indicative that the cells are less proliferative and start to induce apoptotic routes.^{45,46}

3.7. Approaches for feature extraction

Principal Component Analysis is a technique used in large data sets to reduce the number of variables while still retaining much of the information. The reduction is possible by transforming the variables to a new subset, the principal components, which are not correlated and are ordered so that the first ones keep most of the variation of the original set of variables.⁴⁷ Taguchi et al. employed a method based on PCA, sparse PCA, to select miRNAs as biomarkers. Contrary to PCA, sparse PCA uses a smaller number of features to express the lower dimensional space⁴⁸. Many other studies have used PCA to separate between subpopulations of different disease states⁴⁹ or distinguish between healthy and malignant tissue⁵⁰.

In our study, PCA can help us to discover any correlation in the miRNA variable expression. First, we performed a PCA of the treatments for GBM6 and GBM10 separately (**Figure 4-9**). Analyzing the biplot from GBM6 (where the points are the treatments, and the vectors are the variability of the miRNA expression), we can observe that at 48h most of the variance comes from the upregulation of miR 335 and 222, and possibly their regulation seems to be correlated. On the other hand, the variability at longer times in GBM10 gets explained by the upregulation of miR 124a at 24h and 106a at 48h (both tumor suppressors).

We also made the PCA biplot of all the treatments (**Figure 4-10**). The projection discriminates the treatments at longer times between GBM6 and GBM10. In this plot, we can also observe what we explained in the previous paragraph, that most of the variability at longer times for GBM6 can be explained by the upregulation of miR 335 and miR 222 and most of the variability at longer times for GBM10 can be explained by upregulation of miR 106a and miR 124a. Also, we can observe the correlation between three different clusters of miRNAs in our panel: miR 222, 335 and 155 (all of them with oncogenic roles), miR 106 and 124a (tumor suppressors) and let 7f and 29a (tumor suppressors).

In this study, we have shown some exploratory data analysis to prove the potential of this strategy to study miRNA signatures. Using these signatures, we could classify the cell lines based on their expression profile and also provide indicators of treatment success or which direction to

follow for an alternative treatment. However, a more significant number of samples or more targets must be studied to obtain more conclusive results. Also, another kind of biomarkers, such as phosphoproteins could be integrated into the analysis to complement the miRNA profiling and observe how the up or downregulation of these small transcripts correlate with the expression of the proteins.

4. Conclusions

In this chapter, we have studied the expression profile of eight miRNAs by using the technology described in chapter 2. This technology employed asymmetric PCR for transcripts amplification and microring resonators as the detection device. This approach allows us to do quantitative multiplexed analysis in less than two hours per sample with inputs and detection levels comparable to conventional qPCR. Using this approach we have been able to see significant differences in a miRNA panel for two cells cultures from PDX over time and under different treatments. We have used a panel of just eight miRNAs, but the technology can do measurements of up to 16 targets. Also, future efforts will be guided towards the combination of RNA and protein targets to offer more insight about the co-regulation of different targets with the end to find which pathways are affected under the different treatments.

FIGURES

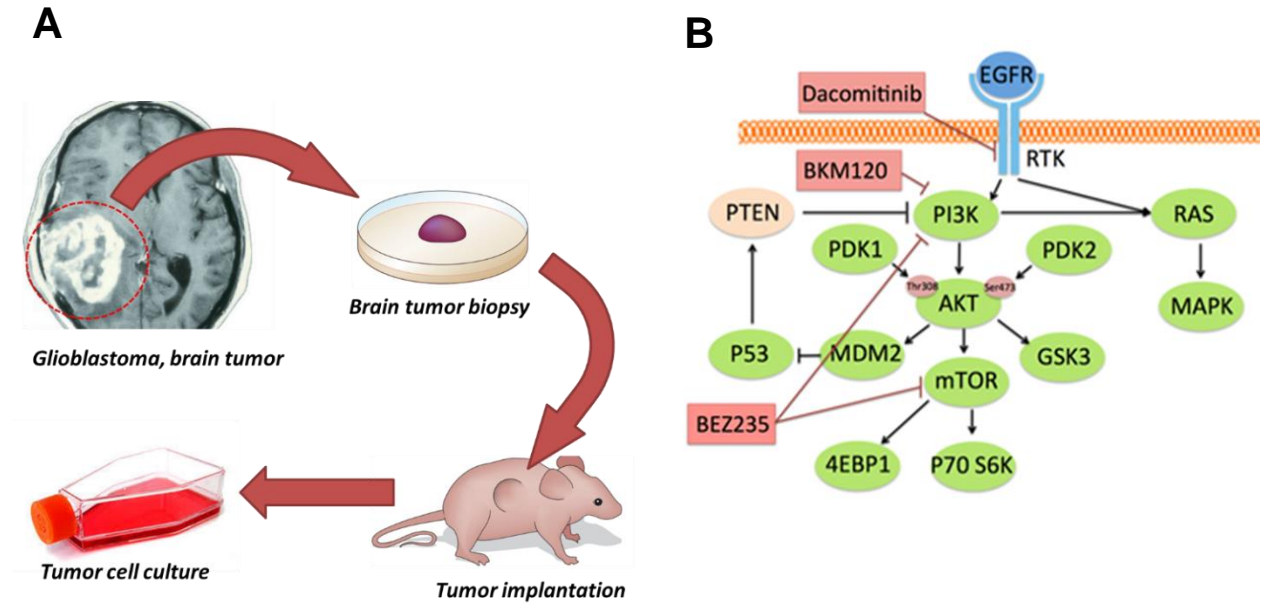


Figure 4-1. (A) Schematic of PDX cell culture. (B) EGFR/Akt/mTOR pathway with the treatments.

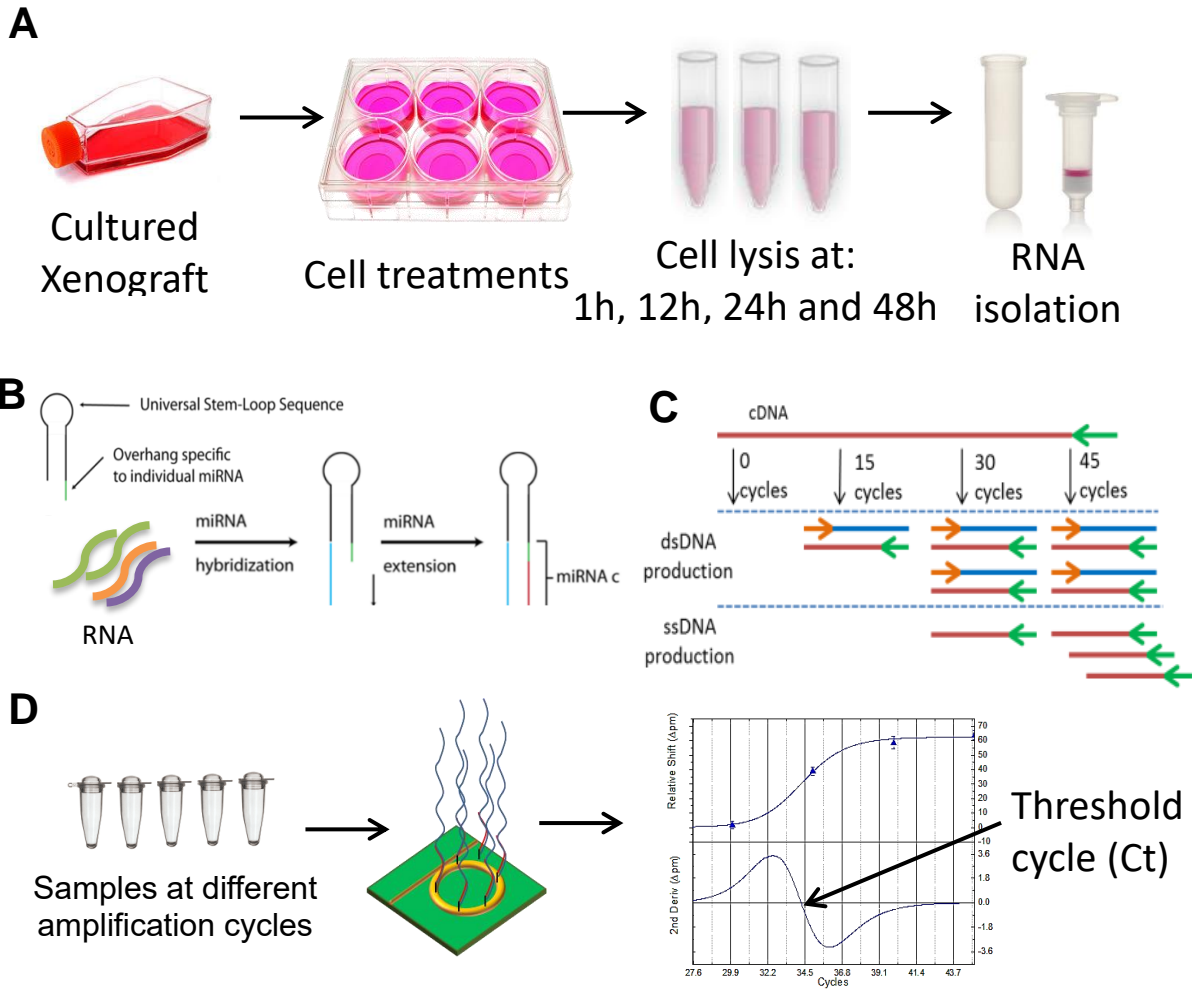


Figure 4-2. (A) Cell treatments and RNA extraction (B) Reverse transcription using stem-loop primers. (C) Asymmetric PCR (D) Sample collection and ring hybridization.

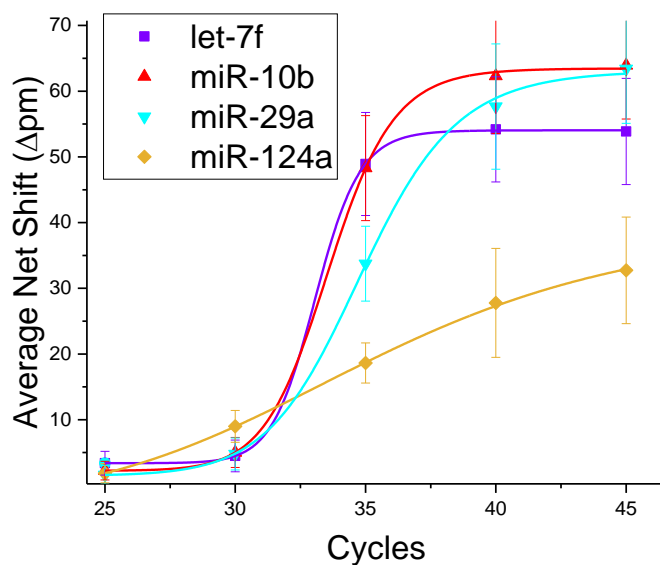
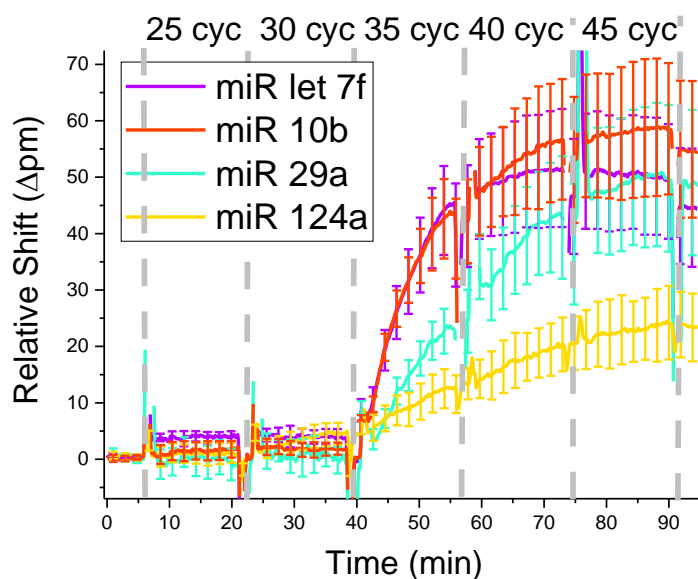


Figure 4-3. (A) Microring traces lines for the detection of 4 miRNAs from the serum control sample at time 0h. (B) Average net shifts as a function of cycle number for the detection of 4 miRNAs in the serum control sample at 0h. (Measurements were done simultaneously on eight miRNA and an off-target control, but for clarity, we have only plotted four). The average represents the signal of four microrings.

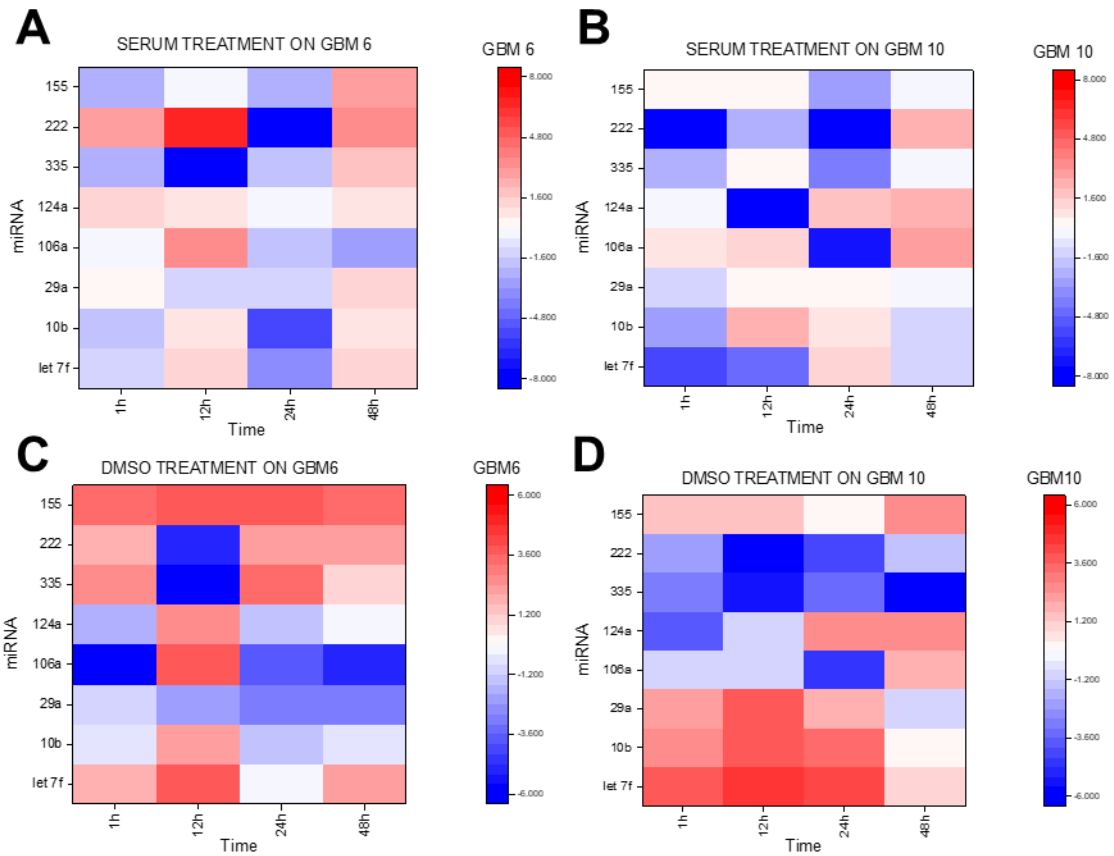


Figure 4-4. (A) Comparison of serum over time for GBM6 (B) Comparison of serum over time for GBM10 (C) Comparison of DMSO over time for GBM6 (D) Comparison of DMSO over time for GBM10.

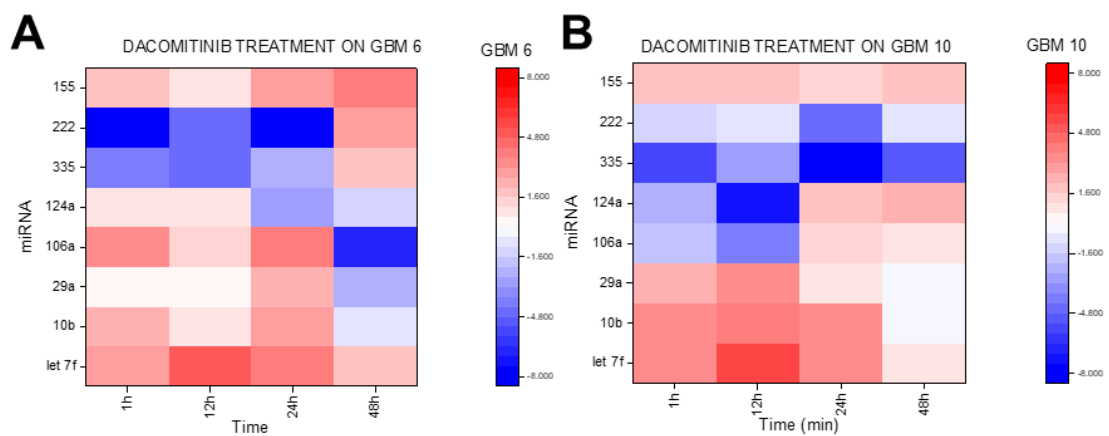


Figure 4-5. (A) Comparison of Dacomitinib treatment over time for GBM6. (B) Comparison of Dacomitinib treatment over time for GBM10.

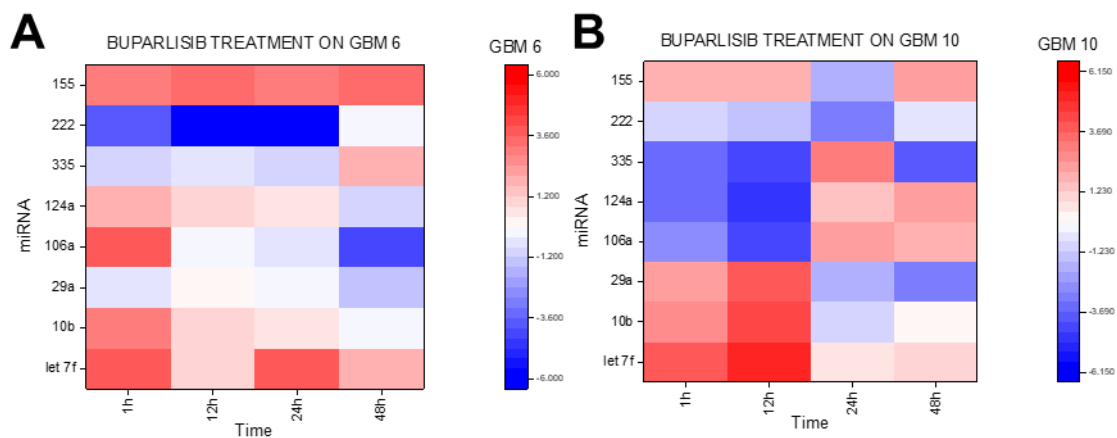


Figure 4-6. (A) Comparison of buparlisib treatment over time for GBM6. (B) Comparison of buparlisib treatment over time for GBM10.

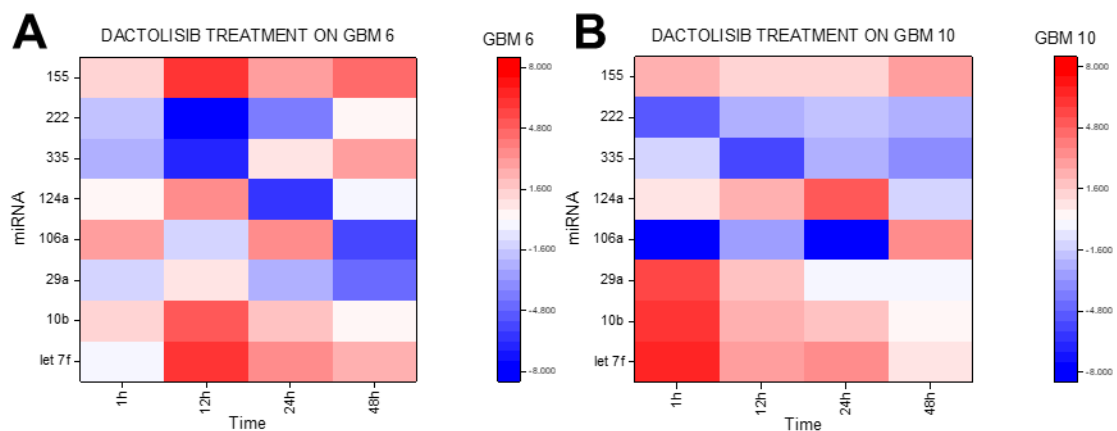


Figure 4-7. (A) Comparison of dactolisib treatment over time for GBM6. (B) Comparison of dactolisib treatment over time for GBM10.

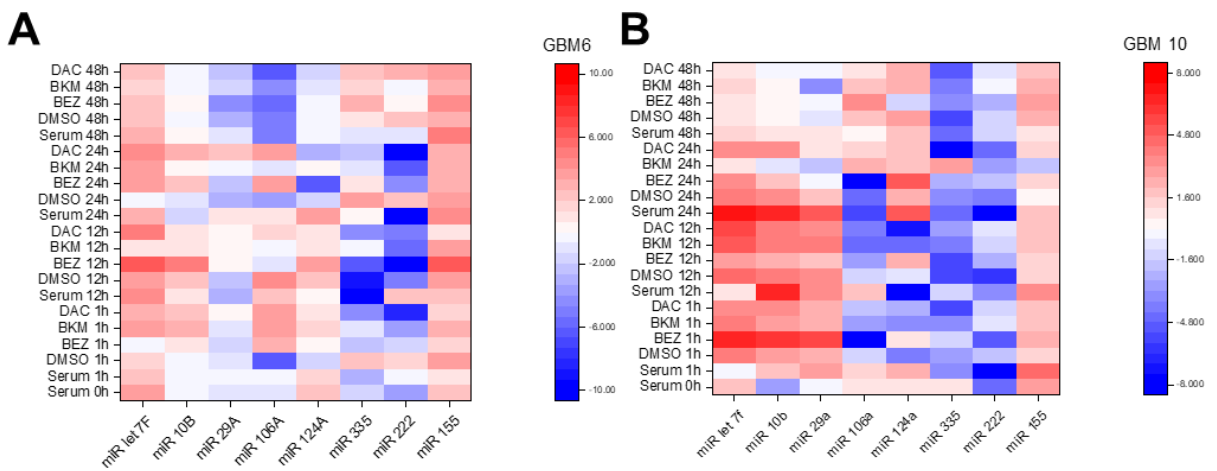


Figure 4-8 (A) Comparison of all the treatments for GBM6 (B) Comparison for all the treatments for GBM10.

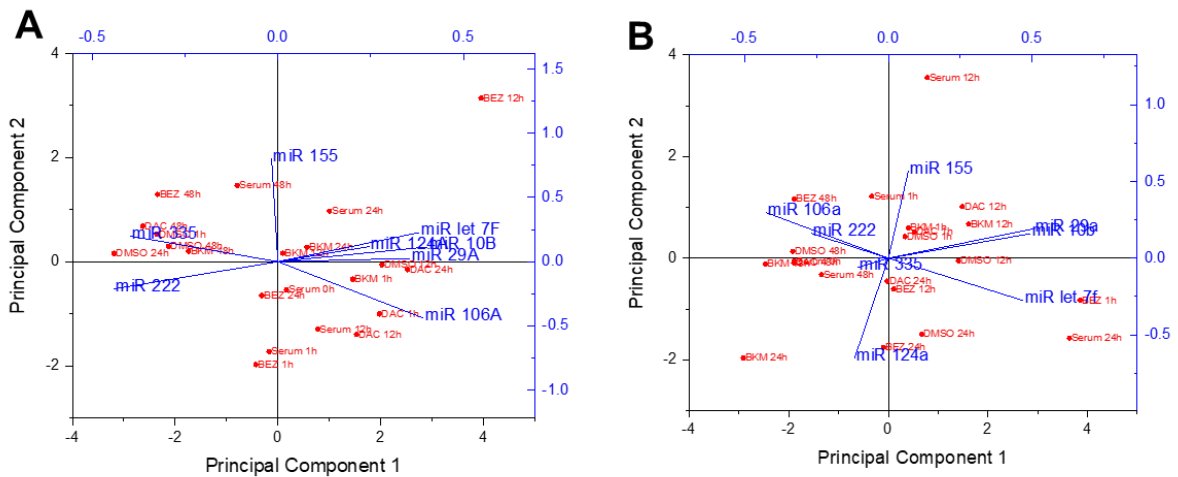


Figure 4-9 (A) PCA biplot for all the treatments for GBM6 (B) PCA biplot for all the treatments for GBM10.

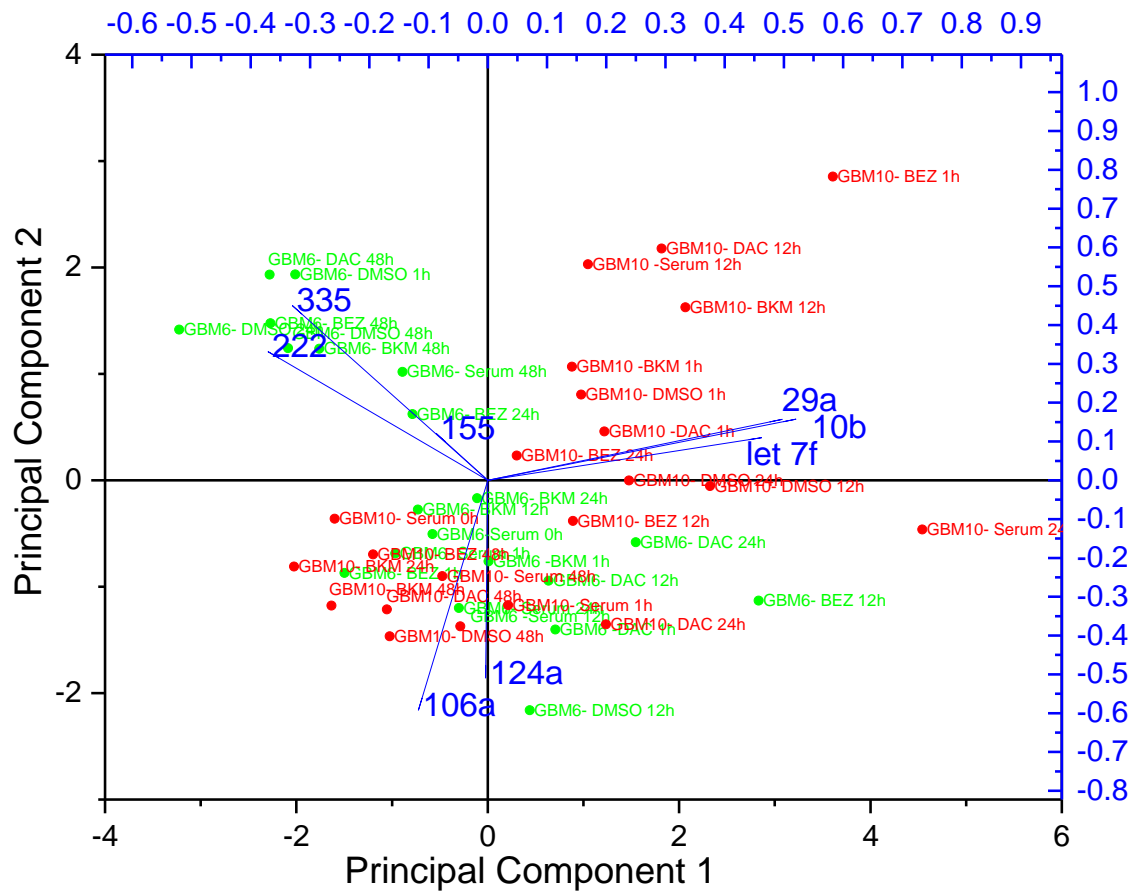


Figure 4-10. PCA biplot for all the treatments for GBM6 and GBM10.

TABLES

Table 4-1. Summary of nucleic acid sequences.

	Sequence
Conserved Stem Loop Primer	GTCGTATCCAGTGCAGGGTCCGAGGTATTCGCACTG GAT... miRNA specific overhang
miR-let7f SLP overhang	AACTATAC
miR-10b SLP overhang	CACAAATTC
miR-29a SLP overhang	TAACCG
miR-335 SLP overhang	ACATTTTT
miR-124a SLP overhang	GGCATTC
miR-222 SLP overhang	GAGACCC
miRNA-106a SLP overhang	CTACCTG
miR-155 SLP overhang	ACCCCT
Conserved reverse primer	GTGCAGGGTCCGAGGT
miR-let7f forward primer	CGCGCTGAGGTAGTAGATT
miR-10b forward primer	GCGTACCCTGGTAGAACC
miR-29a forward primer	CGCTAGCACCATCTGAAAT
miR-335 forward primer	CGCGTCAAGAGCAATAACG
miR-124a forward primer	CGTAAGGCACGCGGT
miR-222 forward primer	CGAGCTACATCTGGCTACT
miRNA-106a forward primer	CGCGAAAAGTGCTTACAGTG
miR-155 forward primer	CGCGTTAATGCTAATCGTGAT

Table 4-2. Inhibitors for the treatment of the xenograft cell cultures

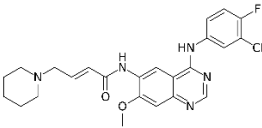
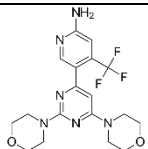
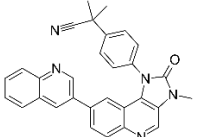
Drug name	Type	Target	Structure
Dacomitinib	Small molecule	EGFR	
Buparlisib (BKM120)	Small molecule	PI3K	
Dactolisib (BEZ235)	Small molecule	PI3K/mTOR	

Table 4-3. miRNA panel used in the study

miRNA	Role	Up/downregulation in GBM	Ref.
Let 7f	Targets: c-Myc, RAS, HMGA, JAK, STAT3, NIRF Let-7 is able to suppress tumor proliferative activities and survival by negatively mediating a number of oncogenes and by affecting critical regulators of the cell cycle, cell differentiation and apoptotic pathway	Down	31,51
10b	Targets: Tp53, FOXO3, .CYLD, PAX6, PTCH1, HOXD10 Upregulation promotes growth, invasion, and angiogenesis.	Up	37,52
29a	Target: MCL1 Downregulation suppresses apoptosis.	Dow	33
106a	Targets: E2F1 and SLC2A3 Downregulation promotes glucose uptake and proliferation.	Down	35,45
124a	Target: SNAI2 Its expression inhibits proliferation of GBM cells and induces differentiation of brain tumor stem cells.	Down	36
335	Target: Daam1 Upregulation increases viability and invasiveness of tumoral cells and decreases apoptosis.	Up	38
222	Targets: p27, p57, PTEN, and PTPu. Upregulation increases proliferation, cell migration, and invasiveness.	Up	39
155	Targets: GABRA1 Upregulation contributes to the malignant GBM cells proliferation removing growth inhibition	Up	41,53

BIBLIOGRAPHY

- (1) Sundeep Deorah, Charles F. Lynch, Z. A. S. and T. C. R. Trends in Brain Cancer Incidence and Survival in the United States: Surveillance, Epidemiology, and End Results Program, 1973 to 2001. *J. Neurosurg.* **2006**, 20 (4), E1.
- (2) Karachi, A.; Dastmalchi, F.; Mitchell, D. A.; Rahman, M. Temozolomide for Immunomodulation in the Treatment of Glioblastoma. *Neuro. Oncol.* **2018**, 20 (12), 1566–1572.
- (3) Paolillo, M.; Boselli, C.; Schinelli, S.; Paolillo, M.; Boselli, C.; Schinelli, S. Glioblastoma under Siege: An Overview of Current Therapeutic Strategies. *Brain Sci.* 2018, Vol. 8, Page 15 **2018**, 8 (1), 15.
- (4) Li, X.; Wu, C.; Chen, N.; Gu, H.; Yen, A.; Cao, L.; Wang, E.; Wang, L.; Li, X.; Wu, C.; et al. PI3K/Akt/MTOR Signaling Pathway and Targeted Therapy for Glioblastoma. *Oncotarget* **2016**, 7 (22), 33440–33450.
- (5) Kijima, N.; Kanemura, Y. *Mouse Models of Glioblastoma*; Codon Publications, 2017.
- (6) Richmond, A.; Su, Y. Mouse Xenograft Models vs GEM Models for Human Cancer Therapeutics. *Dis. Model. Mech.* **2008**, 1 (2–3), 78–82.
- (7) Detassis, S.; Grasso, M.; Del Vescovo, V.; Denti, M. A. MicroRNAs Make the Call in Cancer Personalized Medicine. *Front. Cell Dev. Biol.* **2017**, 5, 86.
- (8) Kiang, K.; Zhang, X.-Q.; Leung, G. Long Non-Coding RNAs: The Key Players in Glioma Pathogenesis. *Cancers (Basel)*. **2015**, 7 (3), 1406–1424.
- (9) Cai, Y.; Yu, X.; Hu, S.; Yu, J. A Brief Review on the Mechanisms of MiRNA Regulation. *Genomics Proteomics Bioinforma.* **2009**, 7, 147–154.
- (10) Si, Y.; Cui, X.; Crossman, D. K.; Hao, J.; Kazamel, M.; Kwon, Y.; King, P. H. Muscle

- MicroRNA Signatures as Biomarkers of Disease Progression in Amyotrophic Lateral Sclerosis. *Neurobiol. Dis.* **2018**, *114*, 85–94.
- (11) Zhao, H.; Shen, J.; Hodges, T. R.; Song, R.; Fuller, G. N.; Heimberger, A. B. Serum MicroRNA Profiling in Patients with Glioblastoma: A Survival Analysis. *Mol. Cancer* **2017**, *16* (1), 59.
- (12) Lu, J.; Getz, G.; Miska, E. A.; Alvarez-Saavedra, E.; Lamb, J.; Peck, D.; Sweet-Cordero, A.; Ebert, B. L.; Mak, R. H.; Ferrando, A. A.; et al. MicroRNA Expression Profiles Classify Human Cancers. *Nature* **2005**, *435* (7043), 834–838.
- (13) Hayes, J.; Peruzzi, P. P.; Lawler, S. MicroRNAs in Cancer: Biomarkers, Functions and Therapy. *Trends Mol. Med.* **2014**, *20* (8), 460–469.
- (14) Reinsbach, S.; Nazarov, P. V.; Philippidou, D.; Schmitt, M.; Wienecke-Baldacchino, A.; Muller, A.; Vallar, L.; Behrmann, I.; Kreis, S. Dynamic Regulation of MicroRNA Expression Following Interferon- γ -Induced Gene Transcription. *RNA Biol.* **2012**, *9* (7), 978–989.
- (15) Graybill, R. M.; Bailey, R. C. Emerging Biosensing Approaches for MicroRNA Analysis. *Anal. Chem.* **2016**, *88* (1), 431–450.
- (16) Pritchard, C. C.; Cheng, H. H.; Tewari, M. MicroRNA Profiling: Approaches and Considerations. *Nat. Rev. Genet.* **2012**, *13* (5), 358–369.
- (17) Byron, S. A.; Van Keuren-Jensen, K. R.; Engelthaler, D. M.; Carpten, J. D.; Craig, D. W. Translating RNA Sequencing into Clinical Diagnostics: Opportunities and Challenges. *Nat. Rev. Genet.* **2016**, *17* (5), 257–271.
- (18) Chen, C.; Ridzon, D. A.; Broomer, A. J.; Zhou, Z.; Lee, D. H.; Nguyen, J. T.; Barbisin, M.; Xu, N. L.; Mahuvakar, V. R.; Andersen, M. R.; et al. Real-Time Quantification of MicroRNAs by Stem-Loop RT-PCR. *Nucleic Acids Res.* **2005**, *33* (20), e179.
- (19) Graybill, R. M.; Cardenosa-Rubio, M. C.; Yang, H.; Johnson, M. D.; Bailey, R. C. Multiplexed MicroRNA Expression Profiling by Combined Asymmetric PCR and Label-Free Detection Using Silicon Photonic Sensor Arrays. *Anal. Methods* **2018**, *10* (14).

- (20) Carlson, B. L.; Pokorny, J. L.; Schroeder, M. A.; Sarkaria, J. N. Establishment, Maintenance, and In Vitro and In Vivo Applications of Primary Human Glioblastoma Multiforme (GBM) Xenograft Models for Translational Biology Studies and Drug Discovery. In *Current Protocols in Pharmacology*; John Wiley & Sons, Inc.: Hoboken, NJ, USA, 2011; Vol. 52, p 14.16.1-14.16.23.
- (21) Luchansky, M. S.; Washburn, A. L.; McClellan, M. S.; Bailey, R. C. Sensitive On-Chip Detection of a Protein Biomarker in Human Serum and Plasma over an Extended Dynamic Range Using Silicon Photonic Microring Resonators and Sub-Micron Beads. *Lab Chip* **2011**, *11* (12), 2042–2044.
- (22) Iqbal, M.; Gleeson, M. A.; Spaugh, B.; Tybor, F.; Gunn, W. G.; Hochberg, M.; Baehr-Jones, T.; Bailey, R. C.; Gunn, L. C. Label-Free Biosensor Arrays Based on Silicon Ring Resonators and High-Speed Optical Scanning Instrumentation. *IEEE J. Sel. Top. Quantum Electron.* **2010**, *16* (3), 654–661.
- (23) Cardenosa-Rubio, M. C.; Graybill, R. M.; Bailey, R. C. Combining Asymmetric PCR-Based Enzymatic Amplification with Silicon Photonic Microring Resonators for the Detection of LncRNAs from Low Input Human RNA Samples. *Analyst* **2018**, *143* (5).
- (24) Mestdagh, P.; Van Vlierberghe, P.; De Weer, A.; Muth, D.; Westermann, F.; Speleman, F.; Vandesompele, J. A Novel and Universal Method for MicroRNA RT-QPCR Data Normalization. *Genome Biol.* **2009**, *10* (6), R64.
- (25) D'haene, B.; Mestdagh, P.; Hellemans, J.; Vandesompele, J. Next-Generation MicroRNA Expression Profiling Technology: Methods and Protocols. *Methods Mol. Biol.* *822*.
- (26) Johnson, H.; Del Rosario, A. M.; Bryson, B. D.; Schroeder, M. A.; Sarkaria, J. N.; White, F. M. Molecular Characterization of EGFR and EGFRvIII Signaling Networks in Human Glioblastoma Tumor Xenografts. *Mol. Cell. Proteomics* **2012**, *11* (12), 1724–1740.
- (27) Sarkaria, J. N.; Yang, L.; Grogan, P. T.; Kitange, G. J.; Carlson, B. L.; Schroeder, M. A.; Galanis, E.; Giannini, C.; Wu, W.; Dinca, E. B.; et al. Identification of Molecular Characteristics Correlated with Glioblastoma Sensitivity to EGFR Kinase Inhibition through Use of an Intracranial Xenograft Test Panel. *Mol. Cancer Ther.* **2007**, *6* (3), 1167–

1174.

- (28) Kai, E.; Sawata, S.; Ikebukuro, K.; Iida, T.; Honda, T. and; Karube, I. Detection of PCR Products in Solution Using Surface Plasmon Resonance. *Anal. Chem.*, **1999**, *71*(4), 796–800.
- (29) Sanchez, J. A.; Pierce, K. E.; Rice, J. E.; Wangh, L. J. Linear-After-The-Exponential (LATE)–PCR: An Advanced Method of Asymmetric PCR and Its Uses in Quantitative Real-Time Analysis. *Proc. Natl. Acad. Sci.* **2004**, *101* (7), 1933–1938.
- (30) An, Z.; Aksoy, O.; Zheng, T.; Fan, Q.-W.; Weiss, W. A. Epidermal Growth Factor Receptor and EGFRvIII in Glioblastoma: Signaling Pathways and Targeted Therapies. *Oncogene* **2018**, *37* (12), 1561–1575.
- (31) Yan, S.; Han, X.; Xue, H.; Zhang, P.; Guo, X.; Li, T.; Guo, X.; Yuan, G.; Deng, L.; Li, G. Let-7f Inhibits Glioma Cell Proliferation, Migration, and Invasion by Targeting Periostin. *J. Cell. Biochem.* **2015**, *116* (8), 1680–1692.
- (32) Ru, P.; Hu, P.; Geng, F.; Mo, X.; Cheng, C.; Yoo, J. Y.; Cheng, X.; Wu, X.; Guo, J. Y.; Nakano, I.; et al. Feedback Loop Regulation of SCAP/SREBP-1 by MiR-29 Modulates EGFR Signaling-Driven Glioblastoma Growth. *Cell Rep.* **2016**, *16* (6), 1527–1535.
- (33) Xi, Z.; Wang, P.; Xue, Y.; Shang, C.; Liu, X.; Ma, J.; Li, Z.; Li, Z.; Bao, M.; Liu, Y.; et al. Overexpression of MiR-29a Reduces the Oncogenic Properties of Glioblastoma Stem Cells by Downregulating Quaking Gene Isoform 6. *Oncotarget* **2017**, *8* (15), 24949–24963.
- (34) Wang, Z.; Wang, B.; Shi, Y.; Xu, C.; Xiao, H. L.; Ma, L. N.; Xu, S. L.; Yang, L.; Wang, Q. L.; Dang, W. Q.; et al. Oncogenic MiR-20a and MiR-106a Enhance the Invasiveness of Human Glioma Stem Cells by Directly Targeting TIMP-2. *Oncogene* **2015**, *34* (11), 1407–1419.
- (35) Dai, D.-W.; Lu, Q.; Wang, L.-X.; Zhao, W.-Y.; Cao, Y.-Q.; Li, Y.-N.; Han, G.-S.; Liu, J.-M.; Yue, Z.-J. Decreased MiR-106a Inhibits Glioma Cell Glucose Uptake and Proliferation by Targeting SLC2A3 in GBM. *BMC Cancer* **2013**, *13* (1), 478.
- (36) Fowler, A.; Thomson, D.; Giles, K.; Maleki, S.; Mreich, E.; Wheeler, H.; Leedman, P.;

- Biggs, M.; Cook, R.; Little, N.; et al. MiR-124a Is Frequently down-Regulated in Glioblastoma and Is Involved in Migration and Invasion. *Eur. J. Cancer* **2011**, *47* (6), 953–963.
- (37) Teplyuk, N. M.; Uhlmann, E. J.; Gabriely, G.; Volfovsky, N.; Wang, Y.; Teng, J.; Karmali, P.; Marcusson, E.; Peter, M.; Mohan, A.; et al. Therapeutic Potential of Targeting MicroRNA-10b in Established Intracranial Glioblastoma: First Steps toward the Clinic. *EMBO Mol. Med.* **2016**, *8* (3), 268–287.
- (38) Shu, M.; Zheng, X.; Wu, S.; Lu, H.; Leng, T.; Zhu, W.; Zhou, Y.; Ou, Y.; Lin, X.; Lin, Y.; et al. Targeting Oncogenic MiR-335 Inhibits Growth and Invasion of Malignant Astrocytoma Cells. *Mol. Cancer* **2011**, *10* (1), 59.
- (39) Quintavalle, C.; Garofalo, M.; Zanca, C.; Romano, G.; Iaboni, M.; del Basso De Caro, M.; Martinez-Montero, J. C.; Incoronato, M.; Nuovo, G.; Croce, C. M.; et al. MiR-221/222 Overexpression in Human Glioblastoma Increases Invasiveness by Targeting the Protein Phosphate PTP μ . *Oncogene* **2012**, *31* (7), 858–868.
- (40) Zhang, C.-Z.; Zhang, J.-X.; Zhang, A.-L.; Shi, Z.-D.; Han, L.; Jia, Z.-F.; Yang, W.-D.; Wang, G.-X.; Jiang, T.; You, Y.-P.; et al. MiR-221 and MiR-222 Target PUMA to Induce Cell Survival in Glioblastoma. *Mol. Cancer* **2010**, *9*, 229.
- (41) Zhou, J.; Wang, W.; Gao, Z.; Peng, X.; Chen, X.; Chen, W.; Xu, W.; Xu, H.; Lin, M. C.; Jiang, S. MicroRNA-155 Promotes Glioma Cell Proliferation via the Regulation of MXII. *PLoS One* **2013**, *8* (12), e83055.
- (42) Haumeil, J. C. C.; Rnaud, P. A. Evaluación de La Citotoxicidad de DMSO En Cultivo de Celulas Tumorales de Colon.Pdf. **2002**, *25* (12), 1600–1603.
- (43) Speranza, M.-C.; Nowicki, M. O.; Behera, P.; Cho, C.-F.; Chiocca, E. A.; Lawler, S. E. BKM-120 (Buparlisib): A Phosphatidyl-Inositol-3 Kinase Inhibitor with Anti-Invasive Properties in Glioblastoma. *Sci. Rep.* **2016**, *6* (1), 20189.
- (44) Shi, F.; Zhang, J.; Liu, H.; Wu, L.; Jiang, H.; Wu, Q.; Liu, T.; Lou, M.; Wu, H. The Dual PI3K/MTOR Inhibitor Dactolisib Elicits Anti-Tumor Activity in Vitro and in Vivo.

Oncotarget **2018**, 9 (1), 706–717.

- (45) Yang, G.; Zhang, R.; Chen, X.; Mu, Y.; Ai, J.; Shi, C.; Liu, Y.; Shi, C.; Sun, L.; Rainov, N. G.; et al. MiR-106a Inhibits Glioma Cell Growth by Targeting E2F1 Independent of P53 Status. *J. Mol. Med.* **2011**, 89 (10), 1037–1050.
- (46) Karsy, M.; Arslan, E.; Moy, F. Current Progress on Understanding MicroRNAs in Glioblastoma Multiforme. *Genes Cancer* **2012**, 3 (1), 3–15.
- (47) Jolliffe, I. T. *Principal Component Analysis, Second Edition*; Springer -Verlag New York, 2002.
- (48) Taguchi, Y.; Murakami, Y. Principal Component Analysis Based Feature Extraction Approach to Identify Circulating MicroRNA Biomarkers. *PLoS One* **2013**, 8 (6), e66714.
- (49) Farina, N. H.; Ramsey, J. E.; Cuke, M. E.; Ahern, T. P.; Shirley, D. J.; Stein, J. L.; Stein, G. S.; Lian, J. B.; Wood, M. E. Development of a Predictive MiRNA Signature for Breast Cancer Risk among High-Risk Women. *Oncotarget* **2017**, 8 (68), 112170–112183.
- (50) Carlsson, J.; Davidsson, S.; Helenius, G.; Karlsson, M.; Lubovac, Z.; Andrén, O.; Olsson, B.; Klinga-Levan, K. A MiRNA Expression Signature That Separates between Normal and Malignant Prostate Tissues. *Cancer Cell Int.* **2011**, 11 (1), 14.
- (51) Mizuno, R.; Kawada, K.; Sakai, Y. The Molecular Basis and Therapeutic Potential of Let-7 MicroRNAs against Colorectal Cancer. *Can. J. Gastroenterol. Hepatol.* **2018**, 2018, 5769591.
- (52) Lin, J.; Teo, S.; Lam, D. H.; Jeyaseelan, K.; Wang, S. MicroRNA-10b Pleiotropically Regulates Invasion, Angiogenicity and Apoptosis of Tumor Cells Resembling Mesenchymal Subtype of Glioblastoma Multiforme. *Cell Death Dis.* **2012**, 3 (10), e398–e398.
- (53) Marsigliante, S.; D’Urso, O. F.; Storelli, C.; Mallardo, M.; Gianfreda, C. D.; Montinaro, A.; Cimmino, A.; Pietro, C.; Marsigliante, S. MiR-155 Is up-Regulated in Primary and Secondary Glioblastoma and Promotes Tumour Growth by Inhibiting GABA Receptors. *Int. J. Oncol.* **2012**, 41 (1), 228–234.

CHAPTER V

Quantification of PolyPhosphates using Microring Resonators

Acknowledgments

Stephanie Smith, Rachel Hemp and Catherine Baker from the Morrissey lab conceived the idea of the detection of polyphosphates using cationic polymers and a polyphosphate binding domain[§]. My contribution in this research included the adaptation of the detection protocol using the microring resonators, optimizing and designing the experiments, the realization of the calibration curves, analysis of the results and measurement in real sample. I would also like to acknowledge all the reagents and materials that the Morrissey lab donated to us in the course of this research. I would also like to thank the two students who helped in the realization of these experiments: Marina Sarcinella and Beau S. Schweitzer.

Abstract

Polyphosphate (polyP) is a linear, inorganic molecule composed of tens to thousands of linked phosphate residues. It has been identified in all higher organisms and more recently has been described in humans as a strong procoagulant and proinflammatory agent. This molecule can be released from platelets or bacterial pathogens causing symptoms found in conditions such as sepsis and other traumas. Therefore, it is essential to improve the methods for the detection of polyP to elucidate its role in disease states. Current polyP detection methods rely on fluorescence or colorimetric detection and can be very laborious and lack requisite sensitivity. We have developed an enzymatically-enhanced assay for polyP using silicon photonic microring resonators. This assay

[§] The patent application for this protocol can be found at: [https://experts.umich.edu/downloads/patents?ucid=WO-2018191582-](https://experts.umich.edu/downloads/patents?ucid=WO-2018191582-A1)

is based upon the high-affinity binding of polyP to a cationic polymer bound to the microring surface, followed by subsequent detection using a polyP binding domain and enzymatic signal enhancement. The microring resonator platform is sensitive to any changes in the refractive index near the sensor surface, and importantly here allows for assay optimization through real-time visualization of analyte and reagent binding steps. Taken together, we are working to optimize polyP detection in a range of relevant sample matrices and hope to achieve and lower limits of detection than conventional methods.

1. Introduction

Polyphosphate (polyP) is a linear inorganic molecule composed of tens to thousands of linked phosphate residues. PolyP can be found in prokaryotic and eukaryotic cells and have numerous and diverse biological functions. Microorganisms usually contain long polyP chains of 100-1000s phosphate monomers. These long molecules have roles that include acting as a substitute for ATP in kinase reactions, serving as a reservoir of inorganic phosphate (Pi), chelating metals (e.g., Mn^{2+} , Mg^{2+} , Ca^{2+}), buffering against alkali conditions, and playing a regulatory role in the physiological adjustments to growth, development, stress, and deprivation ¹.

Shorter polyP chains of 10-100 monomers were first described in mammalian cells by Kumble and Kornberg.² They identified polyP of varying sizes in different tissue locations, suggesting this polymer had diverse functions in mammals. Since then, polyP has been implicated in numerous cell signaling pathways such as mitochondrial metabolism, neuronal stimulation, and cell death.³ Further research found that dense granules in platelets are rich in polyP, and patients with bleeding symptoms that were diagnosed with platelet defects reflected lower than usual polyP levels ⁴. Platelet polyP is narrower in size distribution (ranging from 60 to 100 phosphate units), and recent research has shown that it can serve as a procoagulant, prothrombotic, and proinflammatory molecule⁵.

As more evidence supporting the importance of polyP in biological systems emerges, there is a high demand for a method to quantify the polymer in biological fluids. The most important methods are divided into those aiming to visualize and those aiming to quantify polyP. The first approaches to visualize polyP were based on the ability of the molecules to bind cationic dyes like toluidine blue causing a shift in the absorbance of the dye toward shorter wavelengths⁶. Optical

and electron microscopes have also been used to visualize polyP directly in living organisms. Optical microscopy methods involve staining polyP with different dyes, such as toluidine blue or DAPI (fluorescence) and visualizing the polymer in situ⁷. In electron microscopy, polyP can be visualized directly in acidocalcisomes in microorganisms⁸ and dense granules in platelets because it is found in granules that contain high concentrations of divalent metal ions. Other techniques that have been used for the quantification of polyPs include NMR⁹, ion chromatography¹⁰, and capillary electrophoresis¹¹. To date, all of these methods to quantify polyP require the extraction and purification of polyP from a complex matrix before quantification^{12,13}. There is evidence that these extraction and purification methods can influence the size and amount of recovered polyP¹⁴, so a method that does not require them is needed.

Silicon photonic microring resonators have been used in our lab to detect a variety of analyte classes¹⁵⁻¹⁷. They consist of an array of sensors that are sensitive to changes in the local refractive index; therefore, they can be used for molecular recognition monitoring. In this platform, light coming from a tunable laser is confined in an optical waveguide and measured by a detector. Because of constructive interference, specific wavelengths are supported and trapped in the microrings depending on the refractive index of the surface. When analytes bind the surface of the rings, the resonant wavelength changes and this resonant shift is measured by the instrument and reported as the sensor signal. By measuring these shifts over time, different binding events can be visualized at the sensor surface in real time. The sensor is based on light from a tunable wavelength laser that enters a linear waveguide and couples to adjacent microrings at specific wavelengths. The coupling wavelength, or resonant wavelength, λ , is described by the following equation:

$$m\lambda = 2\pi r n_{eff}$$

where n_{eff} is the effective refractive index in the surface of the microring. Therefore, any event that occurs on the surface manifests as a change in the effective refractive index, and consequently as a shift in λ . By measuring this shift over time, we can obtain a sensorgram that enables the identification of different binding stages in an experiment¹⁸.

In this chapter, I present a method to quantify polyP directly in biological samples. The method consists of online capturing of polyP molecules to the rings through strong binding to a cationic polymer and posterior recognition using a polyP binding domain. This method allows for

fast quantification of both short and long molecules of polyP directly from different biological matrices, including serum and platelet releasates, without prior extraction or purification.

2. Methodology

Materials

Polyphosphate P700 (long chain, 200-1300 phosphate units), Polyphosphate P100 (medium chain, 45-160 phosphate units), narrowly fractionated Polyphosphates mode 76 (61-104) and mode 1100 (970-1370), and biotinylated Polyphosphate binding domain (biot-PPXbd) were donated from the laboratory of Prof. James H. Morrissey, at the University of Michigan. Polyethyleneimine was purchased from Sigma Aldrich. Chemicals used for the preparation of the buffers (**Table 5-1**) were from Sigma-Aldrich, ThermoFisher, and VWR.

Silicon Photonic Microring Resonator instrumentation

All measurements of polyP were made on the Maverick M1 optical scanning instrumentation and silicon photonic microring resonator sensors, Genalyte, Inc. Configuration and operation of the detection platform have been described in previous publications.^{18,19} The chip that contains the microring sensors consist of a silicon-on-insulator chip of 4mmx6mm carrying 128 individually addressable microrings of 30 um diameter. Also, there are eight covered microrings that serve as thermal and fluidic leakage control. Cleaned silicon chips were introduced in the instrument inside a microfluidic system formed by a two-channel microfluidic Mylar gasket sandwiched between a chip holder and a Teflon cartridge top. The Teflon cartridge is connected to tubing that can deliver the fluids to the sensor at the desired flow rate.

Surface functionalization

Before functionalization, sensor chips were washed with acetone to remove the photoresist coating. The silica chip surface was also treated with Piranha solution for further cleaning and 100 mM NaOH for one minute to increase the negative charges on the surface. Then, the sensor substrates were rinsed with water and dried with nitrogen. Freshly cleaned chips were functionalized online and offline with polytethylenimine (PEI) in coating buffer (**Table 5-1**). When functionalized offline, 200 nL droplets of 5.4 µg/ml PEI in coating buffer were incubated

on top of the rings in a humidity chamber. Online functionalization consisted of flowing the solution of 5.4 µg/ml PEI in coating buffer over the surface for 15 min.

Sample preparation

A polyP stock was made in MiliQ water at 1 M, and then was dissolved in polyP buffer (**Table 5-1**) to generate standards for the calibration curve in a volume of 400 µL. For the standard preparation in serum, the stock polyP was added to a mixture of 4:1 serum:5X polyP buffer. Polyacrylamide Gel Electrophoresis corroborated the size range of the fragments. 100 µM of polyP dilutions in water were loaded in 5% TBE polyacrylamide gels and run for 45 min at 150V. For visualizing the PolyP fragments, gels were stained with 0.05% toluidine blue in a 5% glycerol, 25% methanol solution for thirty minutes.

Platelet releasate sample preparation

Platelet releasates were kindly donated by Dr. Stephanie A. Smith from the Morrissey lab. The platelets were suspended in Tyrode's solution (137 mM NaCl, 2.7 mM KCl, 12 mM NaHCO₃, 1 mM MgCl₂, 5.5 mM glucose, 0.35% bovine serum albumin, pH 7.35) and activated with TRAP (Thrombin Receptor Activating Peptide). Then, the platelets were centrifuged and the supernatant with the platelet content was frozen at -80C for further analysis. 10 mM EDTA was added to some of the platelet releasates to stabilize the polyP content. When making the calibration curve for the effect of the platelet releasate matrix, the polyP content was already in the sample was digested by adding 10 ug/ml of ScPPX and incubating the sample overnight at 37C. 10 mM EDTA was added after digestion to inactivate the enzyme, and the samples were stored at -80C until further use for the calibration.

Polyphosphate detection

For all steps, the solution flow rate was set to 30 µL/min. Recipes for the different buffers are listed in **Table 5-1**. First, coating buffer was flown across the chip (5 min) followed by 15 min of 5 µg/ml of PEI in coating buffer. After the functionalization of the chip, washing buffer containing 0.5% BSA was flown for two minutes. Then, the polyP buffer containing the polyP and the serum (in some of the cases) was flown over for 15 min. To selectively detect the polyP, 2µg/ml of biot-PPXbd dissolved in the washing buffer + BSA was flown over the surface for 12 min followed by

1 µg/ml SA-HRP also dissolved in washing buffer + BSA. The final step consisted of the enzymatic conversion of 4-chloro-1-naphthol to the insoluble 4-chloro-1-naphton that precipitates on the sensor surface causing a substantial refractive index change and a large corresponding resonance shift.

Analysis of the microring signal

The microring signal was analyzed using OriginPro 2017 software. The sensorgram was obtained by plotting the refractive index shift as a function of time. In the sensorgrams, the responses of 64 (corresponding to one of the fluidic channels) were averaged. The data was also corrected for the thermal drift. The net shift of the signal for the different concentrations of polyP was calculated after the enzymatic signal enhancement from the oxidation of the chloronaphthol. The calibration curve was constructed by plotting the net shift as a function of polyP concentration in monophosphate units and then fit to a logistic four-parameter equation ($Y = (A - B) / [1 + (x/C)^D] + B$). A is the shift measured for the highest concentration of target, B is the shift measured for the lowest concentration of target, C is the concentration producing 50% of the maximum response, and D is the slope at the inflection point of the sigmoid curve. Unknown concentrations were then determined using this calibration curve. The limits of blank and limits of detection were calculated as described by Shrivastava²⁰. The limit of Blank (LoD) was calculated by the following equation: $LOD = \text{mean}_{\text{blank}} + 3(\text{SD}_{\text{blank}})$. The limit of quantitation was calculated by the next expression $LOQ = \text{mean}_{\text{blank}} + 10(\text{SD}_{\text{blank}})$.

Malachite green assay

PolyP standards were also measured by quantifying inorganic phosphate after *Saccharomyces cerevisiae* exopolyphosphatase (ScPPX) digestion²¹. Briefly, 100 µL of polyP standard were mixed with 20 µL of ScPPX1 buffer (50 mM Tris, 5 mM MgCl₂ pH 7.4), 0.2 µL ScPPX1 (10 µg/ml) and 79.8 µL of MiliQ water. The samples with the enzyme were then incubated overnight at 37°C for digestion of the polyP. The digested phosphate was then quantified by measuring the absorption at 620 nm in a commercial malachite green phosphate assay kit (Sigma-Aldrich).

3. Results and discussion

The goal of this project was to develop a strategy to detect and quantify polyP in buffer and biological matrices using the silicon photonic microring resonator platform. The sensor array was cleaned and assembled into a fluidic cartridge and loaded into the Maverick detection system. The strategy consisted of the capture of the polyP molecules by the rings onto the highly cationic polymer bound to the sensor surface. After that, polyP could be selectively quantified due to the binding of a polyP binding domain, PPXbd²². Finally, an enzymatic amplification step caused the deposition of a precipitate onto the surface helping to increase the signal and to lower the LOD. The schematic of the assay is shown in **Figure 5-1**. One of the main advantages of using the ring resonators as a readout instead of other colorimetric and fluorescent techniques is the ability to see the binding events in real-time. We can determine and optimize the best conditions for each step and predict the outcome of the signal.

3.1. Optimization of polyphosphate detection in buffer and serum

The first step optimized in this assay was the functionalization of the surface to capture the polyP molecules. Cationic polymers, particularly low molecular weight branched polyethyleneimine (PEI), have been shown to have a strong affinity for polyP²³. Hence, we decided to use this polymer to capture the polyP molecules onto the ring surface. The functionalization of the surface can be performed by physisorption or covalent attachment of the receptor molecules. Previous work in our group proved the strong physisorption of cationic polymers to the silica surface of the rings²⁴. Given the simplicity, reduction in reagent cost and time, we chose to use the physisorption technique for the adsorption of the PEI to the surface. The physisorption could be carried out *offline* (spotting the polymer solution over the microarray sensor outside of the instrument) or *online* (flowing the PEI over the surface before the measurement of polyP). After comparing the time of surface functionalization and final quantification signal, we realized that online functionalization of the polymer gave a significant capture of the polyP molecules and overnight functionalization of the cationic polymer was not needed (**Figure 5-2**). Indeed, by monitoring the derivatization step with the PEI, we could ensure that all the rings were covered equally during the functionalization, and the functionalization step was reproducible in each run.

Following the immobilization of the microrings with PEI, the sample containing the polyP molecules was flown over the surface. These polyP standards were diluted in a high ionic strength buffer containing a high amount of LiCl (500 mM). These harsh conditions were selected to disrupt the weak interactions of polyP or PEI with other charged molecules in the sample but still not harsh enough to disrupt the strong interaction of polyP with PEI²³.

For the selective recognition of polyP, we used a polyP binding domain, PPXbd, as described previously²². Also, it contained a site-specific biotinylation site that helped to incorporate a secondary signal amplification via binding of streptavidin-horseradish and a final 4-chloro-1-naphthol (4CN) turnover. This reaction product is insoluble in aqueous buffer and precipitates onto the rings giving a high increase of the signal¹⁷.

After optimization of the different steps, we made calibration curves using standard solutions of polyP (between 10 nM and 5 μ M in monophosphate concentration) of different chain size (mode 76 and 1100). These modes correspond to fractions of polyP with narrow size distribution (mode 76 between 61-104 monomers of phosphate; and mode 1100 for 970-1370 phosphate monomers). We made the calibration with these two size of polymers because these sizes are very similar to the polyP found in platelets and bacteria, respectively (two of the possible applications of this assay). The concentrations of the standards were referenced by a phosphate malachite green assay kit, and the size distribution was observed by PAGE stained with toluidine blue (**Figure 5-3**). The different concentrations of monophosphate were related to the magnitude of the resonance wavelength shift from the 4CN step. The calibration curve for the different concentrations of the different fragments in high ionic strength buffer can be observed in **Figure 5-4**. This curve can be fitted to a logistic curve, and from that curve, the limit of detection and limit of quantification can be determined. A difference in LOD and LOQ is observed for the different fragments—both values are smaller for shorter length polyP. This effect might be due to the poorer mass transfer of the larger polymers to the surface of the sensor arrays.

To probe the efficacy of the assay, we estimated the polyP content from two dilutions for each mode 76 and 1100 in the ranges of their respective curves. The measured resonance wavelength shifts for the spiked samples were interpolated to the respective calibration curve. The agreement between the spiked samples and the previous calibrations curves (**Table 5-2**) show the

robustness of our method to measure polyP. The LOD of commercial phosphate malachite green assays is at 1 μ M phosphate units, and with our assay we showed robust measurements at nM levels.

Because of our interest in direct detection in biological matrices, we proceeded to the detection of polyP in serum. Pooled human serum (Sigma Aldrich) was spiked with known concentrations of polyP. In the serum detection, apart from the LiCl present in the hybridization buffer, we incorporated a rinsing step with a high concentration of urea to clean the surface from other proteins without affecting the binding of the polyP-PEI. The high molarity urea rinse was not necessary when the polyP was diluted in the buffer, but it was necessary for the binding of polyP in the complex matrix (**Figure 5-5**). Serum contains a high amount of proteins (usually in the range 60-80 mg/ml) that can cover the surface hampering the recognition of the PPXbd. The urea step is meant to denature those proteins in the serum and contribute to cleaning the surface from the unwanted interactions, and in consequence, facilitate the PPXbd binding in the next step.

Fig 5-6 corresponds to the calibration curve in human serum. The blank in serum was much lower than the blank in the buffer. The low signal blank might be due to the proteins from the serum that may help to reduce the nonspecific interactions of the PPXbd or the SA-HRP with the surface. Also, the low signal obtained with the blank showed that there was no interference with other charged polymers in the biological matrix.

3.2. Quantification of polyphosphate in platelet releasates

As proof of concept, we measured the endogenous content of polyP in platelet releasates. After extraction of the dense granules, the polyP content was determined to be 0.74 ± 0.08 nmol/ 10^8 platelets by measuring with Phosphorous NMR spectroscopy. Other groups have also determined the content of platelets after extraction of polyP using silicon columns and posterior fluorescence quantitation with DAPI¹². With our assay being able to detect polyP in complex matrices we wanted to check the levels of polyP directly in these samples without the need for extraction.

To measure the PolyP properly in these samples, we had to make calibration curves to account for the matrix effects of the platelet releasates. To make the calibration curves in this

matrix, we first digested the polyP using ScPPX, and then we spiked known concentrations of the standards. Because platelet polyP size is centered around 70 monomers¹¹, we used the narrow fragment mode 76 to construct the calibration curves (**Figure 5-7**). The blank in this case is not as low as in the serum curve. This might be due to the lower amount of proteins in serum. Further optimization might include adding BSA to the solution during the polyP binding step.

Then, we utilized that calibration curve to measure the concentration of four platelet releasates activated with (Thrombin receptor Activating Peptide) TRAP. The concentration of various samples are calculated in **Table 5-3** based on the calibration curve. From these results, we can observe that the amount of polyP is very similar in the different releasates and consistent with previous reports¹¹. In summary, our procedure is robust to perform the quantification of polyP without extraction, and thus avoiding lengthy and biased extraction steps.

4. Conclusions and future directions

A quantitative analysis method for polyP directly from complex biological samples has been established using a microring resonator platform. The sensor substrate was functionalized with a cationic polymer that bound the polyP molecules with high affinity. Then, selective recognition was achieved by a PPXbd recognition step, followed by signal amplification allowing for quantification of low analyte concentrations. This strategy is an improvement compared to other methods in the ability to detect very low levels without the need for previous extraction and purification from complex samples. As a proof of concept of the detection capability, we measured polyP in biological matrices without a significant signal reduction compared to buffer conditions. We have also been able to show how endogenous polyP from platelet releasates can be analyzed using this technology. Future directions of this assay will be to combine the sensitive microring detection with a separation technique to distinguish polyP size in complex samples.

FIGURES

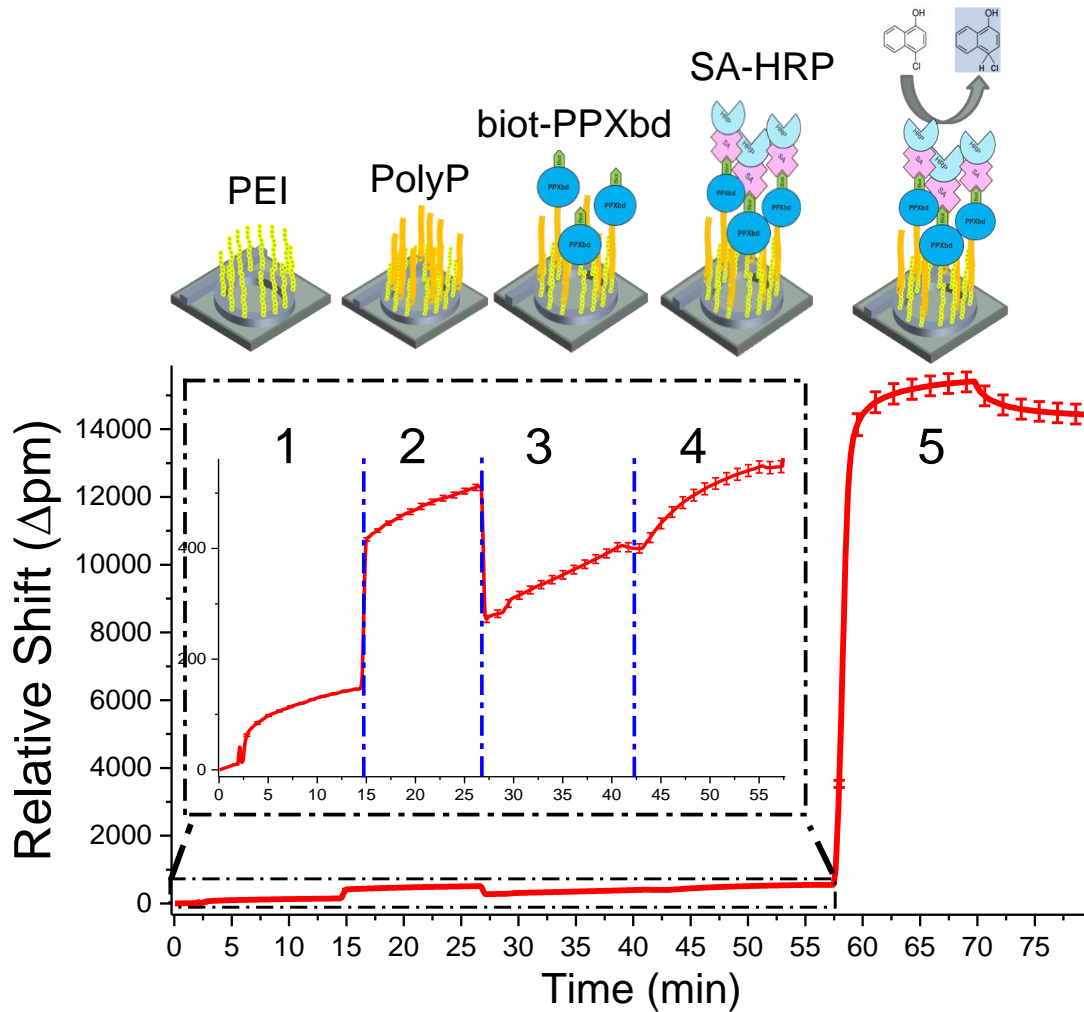


Figure 5-1. Sensorgram of the binding events for the HRP-enhanced polyP detection: 1. PEI *online* functionalization. 2. PolyP binding in high salt concentration (500 mM LiCl). (Optional Urea rinse). 3. Biot-PPXbd binding. 4. SA-HRP binding. 5. 4CN enzymatic turnover.

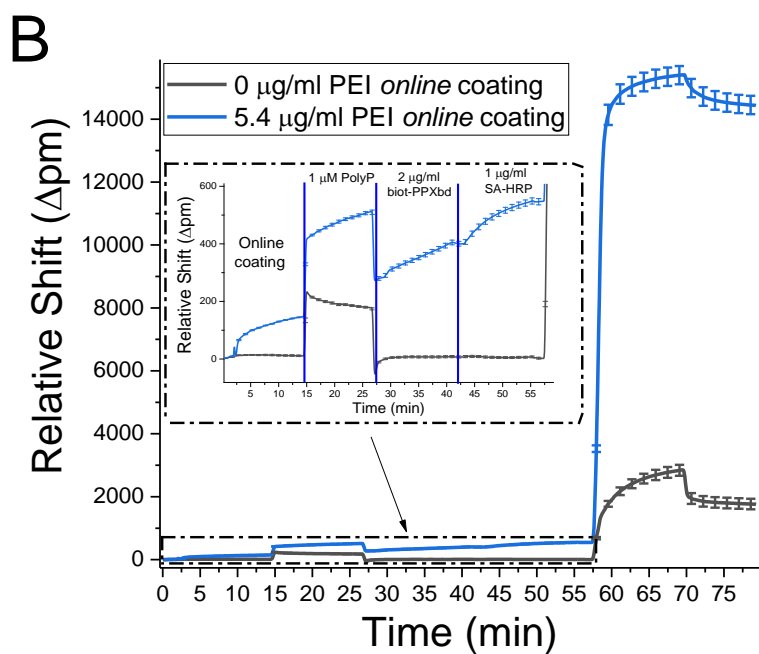
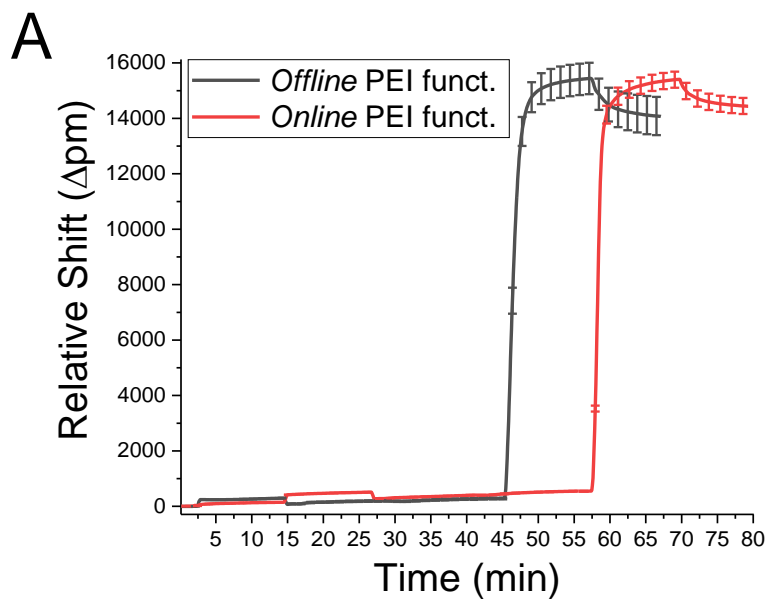


Figure 5-2. Detection of 1 μM polyP under different surface functionalization conditions: A) Comparison *offline* overnight surface functionalization and online functionalization with 5.4 $\mu\text{g/ml}$ PEI in coating buffer in both cases B) Comparison *online* surface functionalization with 5.4 $\mu\text{g/ml}$ PEI in coating buffer and without PEI.

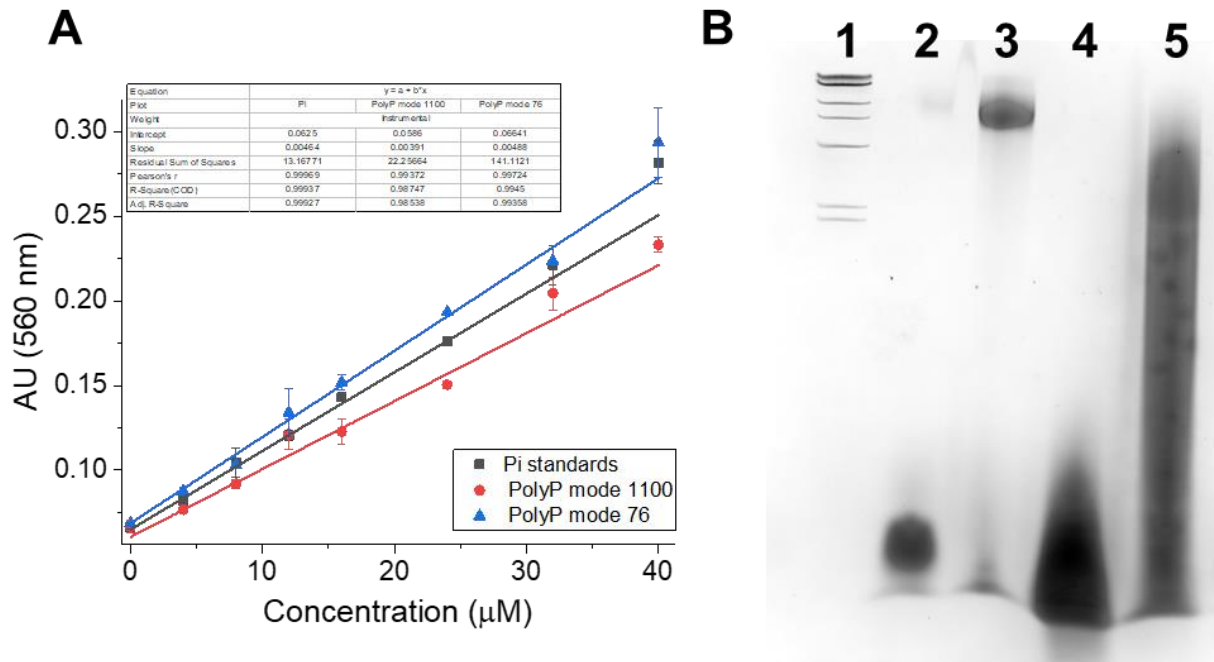


Figure 5-3. (A) Standard concentration measurements checked by malachite green assay after polyP digestion by ScPPX. (B) PAGE of different modes of polyP: lane 1 1Kb DNA ladder, lane 2 mode 76 (500 uM), lane 3 lane 4 (mode 1100), lane 5 (mode 100), lane 6 (mode 700).*

* Mode 76, and 1100 correspond to narrow dispersed polyP fragments while mode 100 and 700 correspond to polydispersed fragments.

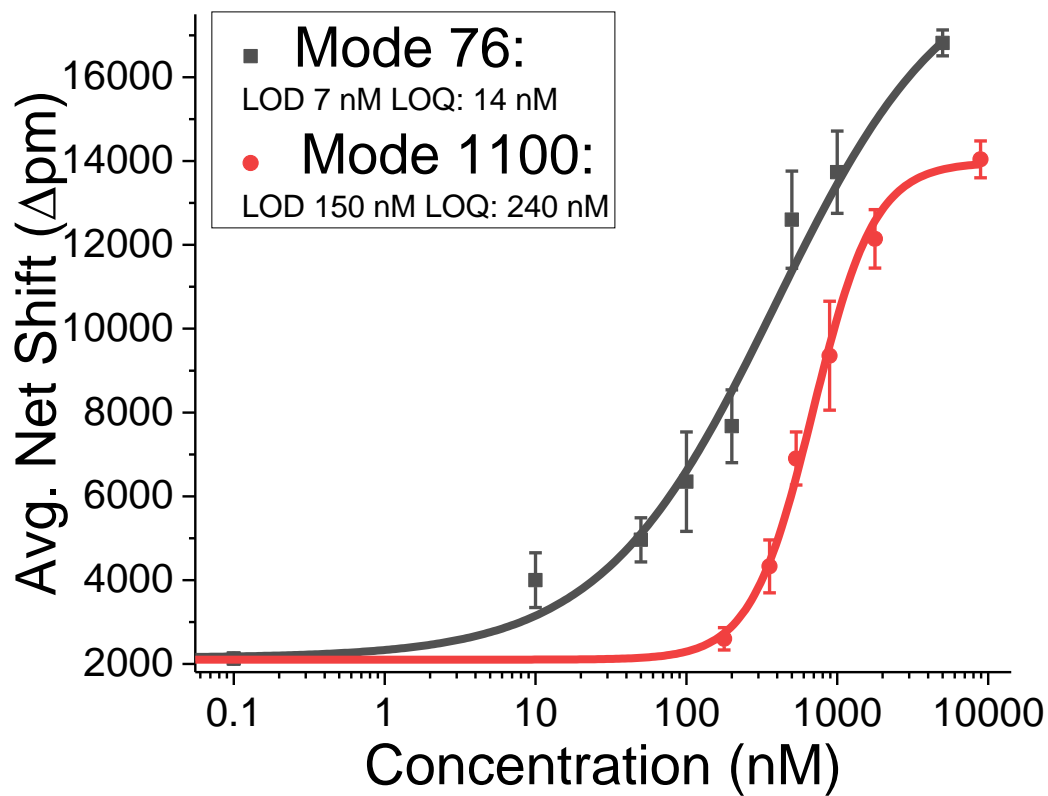


Figure 5-4. Standard curves of polyP mode 76 and 1100 in buffer. The standard deviation of the measurements was calculated in based to the $n > 30$ technical rings replicates.

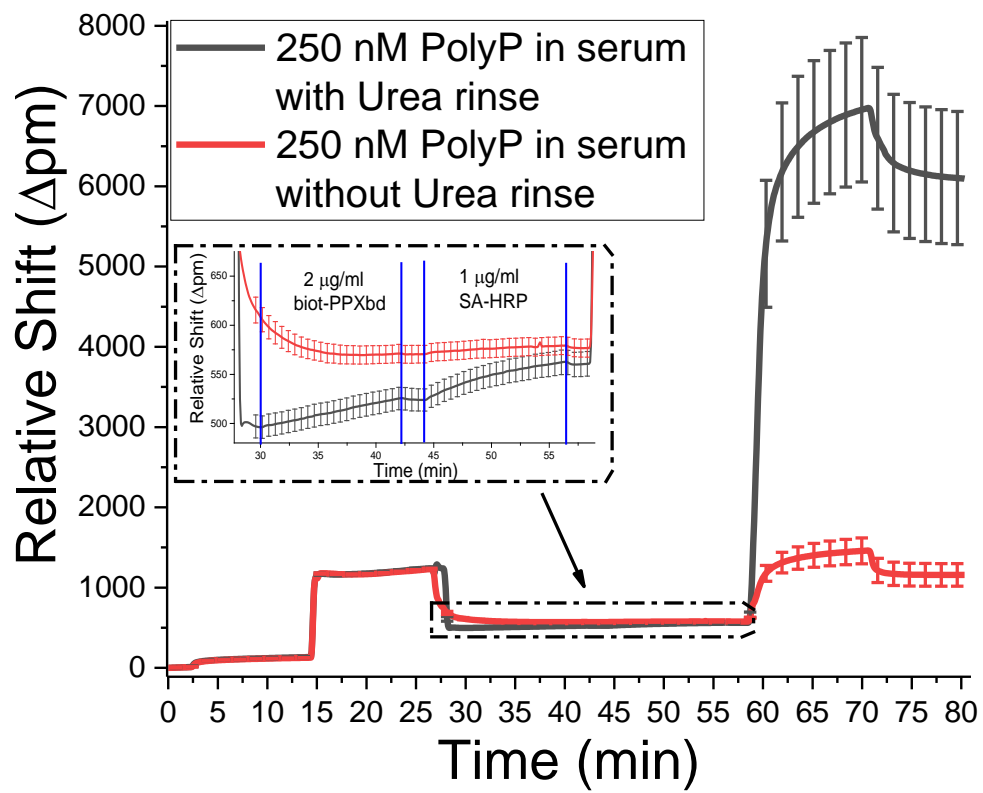


Figure 5-5. Comparison of polyP measurement in serum A) with 1M urea rinse and B) without urea rinse.

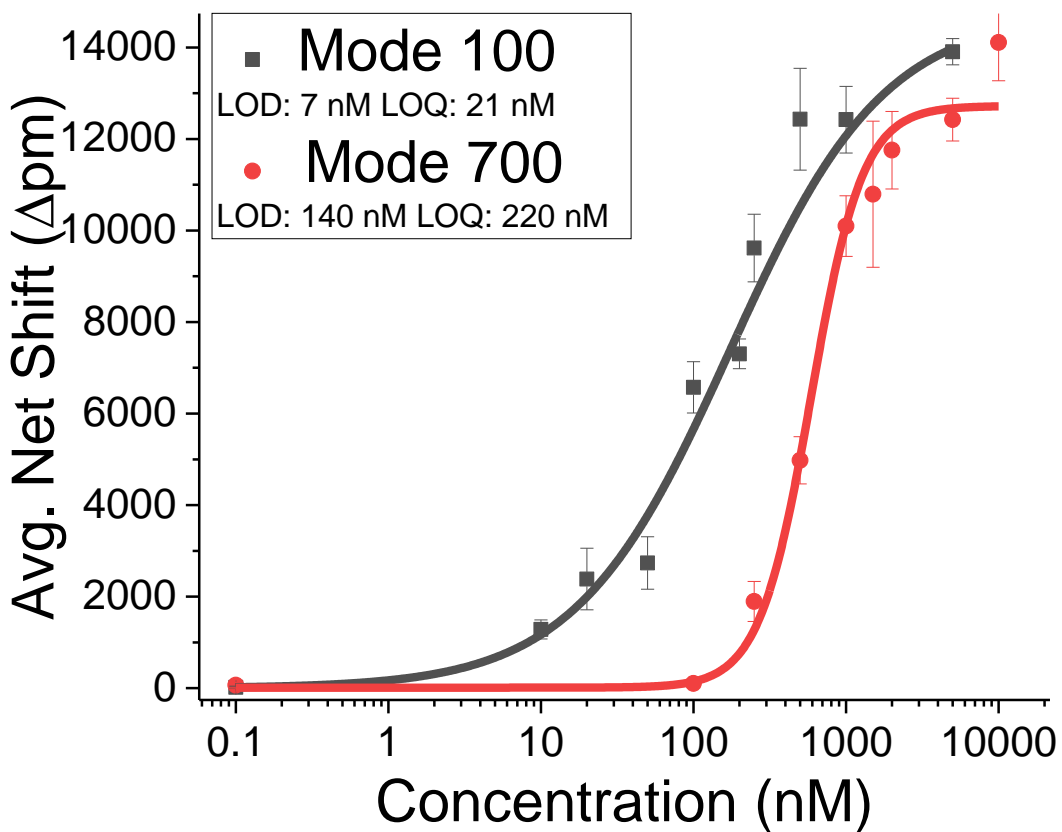


Figure 5-6. Calibration curves of polyP mode 100 and 700 in serum. (Standard deviation was calculated from the n>30 technical ring replicates).

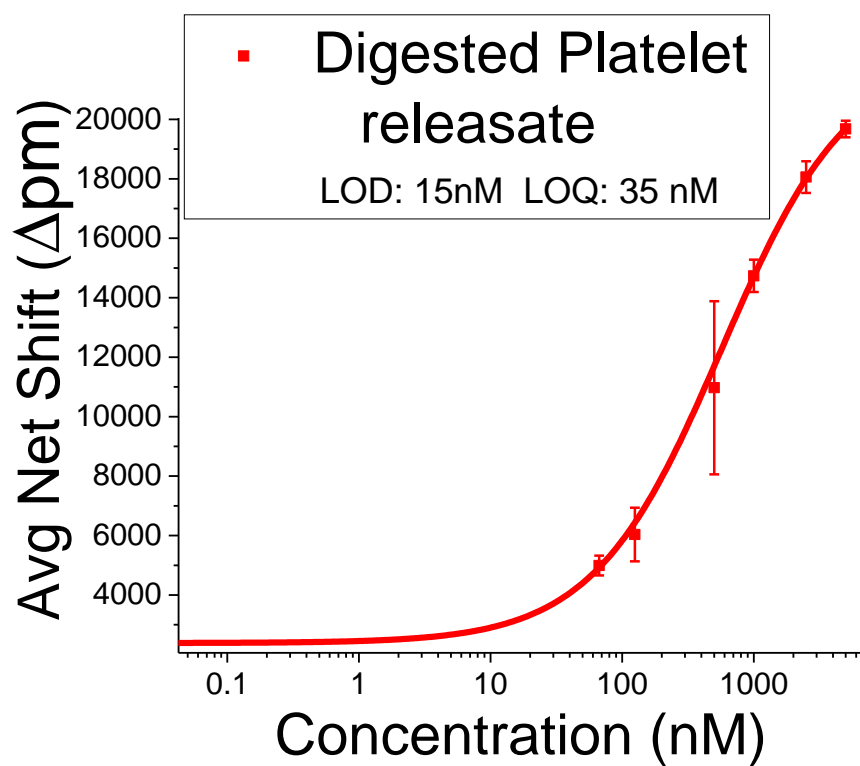


Figure 5-7. A) Calibration curve of polyP mode 76 in platelet releasate matrix after polyP digestion by ScPPX. B) Ring signal for the measurement of two different platelet releasates.

TABLES

Table 5-1. Buffer recipes.

Buffer	Composition
Coating Buffer	50 mM Tris pH 7.4, 100 mM NaCl, 0.05% NaN ₃
1X PolyP buffer	50 mM MES pH 6, 500 mM LiCl, 10 mM EDTA, 0.05% Tween 20
Wash and protein diluent buffer	20 mM HEPES pH 7.0, 100 mM NaCl, 0.5% BSA, 0.05% Tween 20
Urea wash buffer	20 mM HEPES pH 7.0, 500 mM LiCl, 7.4, 1M Urea, 0.05% Tween20, 0.05% NaN ₃

Table 5-2. Analysis of spiked polyP mode 76 and 1100 in buffer using the microring resonators.

Spiked concentrations (nM)		Measured Concentrations (nM)	Recovery (%)
Mode 76	350 nM	366 ± 50 nM	104.57
	150 nM	142 ± 40 nM	94.66
Mode 1100	650 nM	522 ± 50 nM	80.30
	350 nM	280 ± 50 nM	80

Table 5-3. PolyP content from platelet releasates.

Platelet count (x10 ¹¹ /mL)	Average Net Shift (Δpm)	Concentration (nM)	ng/10 ¹¹ platelets
1.7	10622 ± 398	504 ± 41	29.46 ± 2.59
1.2	9567 ± 452	392 ± 30	32.47 ± 1.67
0.83	7883 ± 887	196 ± 53	23.47 ± 4.57

BIBLIOGRAPHY

- (1) Kornberg, A.; Rao, N. N.; Ault-Riché, D. *INORGANIC POLYPHOSPHATE: A MOLECULE OF MANY FUNCTIONS*; 1999.
- (2) Kumble, K. D.; Kornberg, A. Inorganic Polyphosphate in Mammalian Cells and Tissues. *J. Biol. Chem.* **1995**, *270* (11), 5818–5822.
- (3) Angelova, P. R.; Baev, A. Y.; Berezhnov, A. V; Abramov, A. Y. Role of Inorganic Polyphosphate in Mammalian Cells: From Signal Transduction and Mitochondrial Metabolism to Cell Death. *40 Biochem. Soc. Trans.* **2016**, *44*, 40-45.
- (4) HERNÁNDEZ-RUIZ, L.; SÁEZ-BENITO, A.; PUJOL-MOIX, N.; RODRÍGUEZ-MARTORELL, J.; RUIZ, F. A. Platelet Inorganic Polyphosphate Decreases in Patients with Delta Storage Pool Disease. *J. Thromb. Haemost.* **2009**, *7* (2), 361–363.
- (5) Morrissey, J. H.; Choi, S. H.; Smith, S. A. Polyphosphate: An Ancient Molecule That Links Platelets, Coagulation, and Inflammation. *Blood*, **2012**, *119*(25), 5972-5979.
- (6) Clark, J. E.; Wood, H. G. Preparation of Standards and Determination of Sizes of Long-Chain Polyphosphates by Gel Electrophoresis. *Anal. Biochem.* **1987**, *161* (2), 280–290.
- (7) Gomes, F. M.; Ramos, I. B.; Wendt, C.; Girard-Dias, W.; De Souza, W.; Machado, E. A.; Miranda, K. New Insights into the in Situ Microscopic Visualization and Quantification of Inorganic Polyphosphate Stores by 4',6-Diamidino-2-Phenylindole (DAPI)-Staining. *Eur. J. Histochem.* **2013**, *57* (4), 34.
- (8) Jensen, T.] ~. *Electron Microscopy of Polyphosphate Bodies in a Blue-Green Alga, Nostoc Pruniforme*; 1968; Vol. 62.
- (9) MARTIN, F.; CANET, D.; ROLIN, D.; MARCHAL, J. P.; LARHER, F. Phosphorus-31 Nuclear Magnetic Resonance Study of Polyphosphate Metabolism in Intact

- Ectomycorrhizal Fungi. *Plant and Soil*. Springer pp 469–476.
- (10) Kaufmann, A.; Maden, K.; Leisser, W.; Matera, M.; Gude, T. Analysis of Polyphosphates in Fish and Shrimps Tissues by Two Different Ion Chromatography Methods: Implications on False-Negative and -Positive Findings. *Food Addit. Contam.* **2005**, *22* (11), 1073–1082.
 - (11) Ruiz, F. A.; Lea, C. R.; Oldfield, E.; Docampo, R. Human Platelet Dense Granules Contain Polyphosphate and Are Similar to Acidocalcisomes of Bacteria and Unicellular Eukaryotes. *J. Biol. Chem.* **2004**, *279* (43), 44250–44257.
 - (12) Schlagenhauf, A.; Pohl, S.; Haidl, H.; Leschnik, B.; Gallistl, S.; Muntean, W. Non-Enzymatic Quantification of Polyphosphate Levels in Platelet Lysates and Releasates. *J. Pharm. Biomed. Anal.* **2016**, *131*, 1–5.
 - (13) Mukherjee, C.; Mukherjee, C.; Ray, K. An Improved Method for Extraction and Quantification of Polyphosphate Granules from Microbial Cells. *Protoc. Exch.* **2015**.
 - (14) Bru, S.; Jimenez, J.; Canadell, D.; Arino, J.; Clotet, J. Improvement of Biochemical Methods of PolyP Quantification. *Microb. Cell* **2017**, *4* (1), 6–15.
 - (15) Wade, J. H.; Alsop, A. T.; Vertin, N. R.; Yang, H.; Johnson, M. D.; Bailey, R. C. Rapid, Multiplexed Phosphoprotein Profiling Using Silicon Photonic Sensor Arrays. *ACS Cent. Sci.*, **2015**, *1*(7), 374-382.
 - (16) Graybill, R. M.; Cardenosa-Rubio, M. C.; Yang, H.; Johnson, M. D.; Bailey, R. C. Multiplexed MicroRNA Expression Profiling by Combined Asymmetric PCR and Label-Free Detection Using Silicon Photonic Sensor Arrays. *Anal. Methods* **2018**, *10* (14), 1618-1623.
 - (17) Valera, E.; Shia, W. W.; Bailey, R. C. Development and Validation of an Immunosensor for Monocyte Chemotactic Protein 1 Using a Silicon Photonic Microring Resonator Biosensing Platform. *Clin. Biochem.* **2016**, *49*(1-2), 121-126.
 - (18) Washburn, A. L.; Gunn, L. C.; Bailey, R. C. Label-Free Quantitation of a Cancer Biomarker in Complex Media Using Silicon Photonic Microring Resonators. *Anal. Chem.* **2009**, *81*

- (22), 9499–9506.
- (19) Iqbal, M.; Gleeson, M. A.; Spaugh, B.; Tybor, F.; Gunn, W. G.; Hochberg, M.; Baehr-Jones, T.; Bailey, R. C.; Gunn, L. C. Label-Free Biosensor Arrays Based on Silicon Ring Resonators and High-Speed Optical Scanning Instrumentation. *IEEE J. Sel. Top. Quantum Electron.* **2010**, *16* (3), 654–661.
- (20) Shrivastava, A.; Gupta, V. Methods for the Determination of Limit of Detection and Limit of Quantitation of the Analytical Methods. *Chronicles Young Sci.* **2011**, *2* (1), 21.
- (21) Moudřiková, S.; Sadowsky, A.; Metzger, S.; Nedbal, L.; Mettler-Altmann, T.; Mojzeš, P. Quantification of Polyphosphate in Microalgae by Raman Microscopy and by a Reference Enzymatic Assay. *Anal. Chem.*, **2017**, *89*(22), 12006-12013.
- (22) Bolesch, D. G.; Keasling, J. D. Polyphosphate Binding and Chain Length Recognition Of *Escherichia Coli* Exopolyphosphatase. *J. Biol. Chem.* **2000**, *275* (43), 33814–33819.
- (23) Smith, S. A.; Choi, S. H.; Collins, J. N. R.; Travers, R. J.; Cooley, B. C.; Morrissey, J. H. Inhibition of Polyphosphate as a Novel Strategy for Preventing Thrombosis and Inflammation. *Blood* **2012**, *120* (26), 5103–5110.
- (24) Luchansky, M. S.; Washburn, A. L.; Martin, T. A.; Iqbal, M.; Gunn, L. C.; Bailey, R. C. Characterization of the Evanescent Field Profile and Bound Mass Sensitivity of a Label-Free Silicon Photonic Microring Resonator Biosensing Platform. *Biosens. Bioelectron.* **2010**, *26* (4), 1283–1291.

CHAPTER VI

Conclusions and preliminary results of future directions

Acknowledgments

I am very grateful to those senior fellow graduate students, now doctors, who helped me in the development of these projects. Dr. Richard Graybill in the development of asymmetric PCR-MRR for the detection of non coding transcripts. Dr. James Wade for his insights about the PDX GBM cell lines and statistical analysis. Dr. Heather Robinson for helping me initializing the project of polyP detection using microrings.

I would also like to acknowledge the work of undergraduate students and fellow graduate students for their contributions to these projects still underway in the lab. Specifically, I would like to thank Marina Sarcinella and Beau S. Schweitzer for their help in the project of polyP.

In addition, I would like to acknowledge the Kennedy Lab and especially the former graduate student Claire Ouimet for letting us use the capillary electrophoresis instrument. I would also like to thank the Morrissey Lab for the donation of the polyphosphate standards, binding-domains and all the advice and help that they gave us.

1. Introduction

In the previous chapters, I have presented two different projects: (1) multiplexed RNA detection with microring resonator arrays (Chapters 2-4) and (2) detection of polyphosphates using the microring resonators (Chapter 5). Both of these projects relying on the advantages and capabilities of the microring resonator platform. Compared to other technologies, the main advantages are the exquisite sensitivity, multiplexity, and label-free detection.

2. Multiplexed RNA Detection with Microring Resonator Arrays

For the detection of miRNA and lncRNA panels, it was crucial to have a multiplexable technology that could measure with high precision the expression of the transcripts. Combining amplification with aPCR, we achieved lower sample input requirements, higher dynamic ranges and reduced time assays compared to previous strategies using microring resonators^{1,2}.

In the detection of miRNAs, we have proved the reliability of this technology and made the first dynamic profile of a panel of eight miRNAs in more than twenty samples. This dynamic profile demonstrated the potential of this technology to carry out quantitative and multiplexed measurements with little sample input and reduce the time of the assays. In the clinical interpretation of the results, we have employed heatmaps and principal component analysis to interpret the signatures. However, future efforts can be directed to expand the number of samples and targets and work in developing more robust networks of the involved miRNAs in the disease progression. Furthermore, given the capability of the microrings to measure proteins, we could combine the detection of proteins and RNA transcripts to better the correlation of the altered pathways in the course of the disease or treatment³.

In the detection of lncRNAs, we were able to quantify longer transcripts by means by optimizing the primers and visualizing the secondary structure of the regions to be amplified. In previous attempts in the Bailey lab, the hybridization of longer transcripts (mRNAs and tmRNAs) was complicated, and different strategies such as chemical fragmentation⁴ or the use of chaperones⁵ were required to quantify these transcripts.

From the optimization of the assay itself, further progress can be made by more automation of the assay, decreasing the reaction volume and time to the results. From automation and reaction volume reduction, two different strategies could be engineered.

The first strategy could consist of the integration of microfluidic thermal cycling with the microring resonator chip⁶. By using microfluidics, we could make the sample mixture flow in different temperature zones to perform the amplification reaction and later, flow over the chips to hybridize onto the rings. However, some of the limitations of using this strategy will be the optimization in the hybridization conditions (in the PCR reaction we can not use the high stringency hybridization buffer for the reduction of nonspecific interactions) and the stability of the microfluidic device at high temperatures and sealing of the device to the microring to avoid leakage of the material.

The second strategy would be to employ isothermal amplification to avoid using such high temperatures and the need for thermal cycles. Isothermal amplification could be performed onto the microring surface or outside the instrument and later use the instrument to measure the number of transcripts. Previous studies have promoted the strategy of combining isothermal amplification with microring resonators^{7,8}. Some of the limitations of using this strategy will be to devise a new method to quantify our results because the C(t) comparison method will no longer be adequate. Besides, some of the isothermal amplification strategies require very complexed primer designs and difficult multiplexity (such as Loop-Mediated Isothermal Amplification, LAMP) and others require an initial denaturation step (such as Strand Displacement Amplification) or expensive enzymes (Helicase-dependent amplification, HDA or Recombinant-Polymerase Amplification, RPA). However, although the price of the enzymes might be higher, the number of reactions will be reduced and so that could be an alternative if we design a new method to quantify the amplification results.

3. Polyphosphate analysis with microrings

New roles of polyP in micro and higher organisms have drawn much attention to this molecule, and more sensitive and innovative methods are needed to overcome these challenges. Current methods are based in polyP extraction and quantification with DAPI fluorescence measurements or polyP extraction, digestion to monophosphates and quantification with malachite

green. However, all the methodologies require extraction, and this step can confound the results by reduced extraction yield or by contamination with other electronegative polymers.

Chapter 5 outlines the results obtained in the quantification of polyP using microring resonator. This investigation introduces a new methodology to overcome previous limitations in the detection of polyphosphate. The invented protocol was able to quantify different standards in buffer and biological matrices without the need for extraction. In addition, we were able to reach lower limits of detection than conventional malachite green assays. Proof of concept of the assay was performed by measuring endogenous platelet polyP content. This suggests that this assay could be used in determining the polyP content of this type of samples or in other diverse samples.

In the next section, we show preliminary results in size separation of polyP. We have designed two strategies for polyP separation using capillary electrophoresis: (a) using an electrolyte for indirect UV detection and (b) using the affinity of the recombinant polyphosphate binding domain of *Escherichia coli* for polyP, and migration change of the domain when bound at different size polyP. Furthermore, combining together microrings and capillary electrophoresis, we could create a system that is able to size characterize and quantify polyP with high precision.

4. Size characterization of Polyphosphates using capillary electrophoresis

Polyphosphate (PolyP) is a ubiquitous molecule found in all organisms. Its size can vary from a few to thousands monomers. It has been shown that different sizes can exert different roles in coagulation and there is an interest in being able to characterize the size of PolyP in complex samples. Current analytical protocols to characterize polyP size do not provide enough resolution at large size or are cumbersome and require lengthy staining protocols. Herein, we present two strategies to determine polyP size using capillary electrophoresis, CE. One of the drawbacks of CE analysis is the lack of UV absorbance and fluorescence of polyP; and thus, the inability to observe the migration using the two common detectors in CE (UV absorbance or LIF). Therefore, we designed two strategies to detect the molecules indirectly. The first strategy employs a sieving matrix for the resolution of the polymers and indirect UV absorption by adding an electrolyte that absorbs UV light. In the second strategy, we utilize the affinity of a recombinant polyphosphate binding domain of *Escherichia coli* as a means to observe the migration of the polymer. The

migration of the domain changes when it is bound at different size PolyP, and this conjugate can be observed by the UV absorbance of the protein. Future directions of this project will include the hyphenation of CE to the microrings as they do not require labels; and as we proved in chapter V, they can quantify PolyP directly in complex samples.

4.1. Introduction.

Polyphosphate polymers in different organisms and cell types can range from 10 to hundreds of monomers. It can be found in platelets with a size of 60-100n compared to the long size found in microorganisms⁹. Diverse groups have developed strategies to identify the length of the polymer to understand the importance of the size of the polymer.

The first reported methodology was the one already described by Clark and Wood¹⁰. The technique consisted of a PAGE (Polyacrylamide Gel Electrophoresis) separation to resolve a mixture of polyphosphates, and posterior staining with the cationic dye toluidine blue O. Recent investigations have improved this methodology by employing other more sensitive dyes such as DAPI (a fluorescent molecule)¹¹. In addition to slab gel electrophoresis, other researchers have used capillary electrophoresis and ion chromatography to increase the resolution of polyphosphate size. Ion chromatography has been one of the most common methods for the separation and identification for different size polyphosphate molecules¹². However, polyphosphates have a strong affinity for the ion exchangers; therefore, they need to be eluted with very harsh eluents. Secondly, other work has tried with capillary electrophoresis, but polyP suffers from poor UV absorbance and lack of fluorescence. Researchers have tried to circumvent this problem by indirect UV absorption detection^{13,14}. However, these separations focused on small polymer sizes and did not separate polymers higher than 70 phosphate units.

In this project, we aimed to distinguish between a more diverse range of sizes, bacterial polyP (1000n) and platelet polyP (70n), both of them having different roles in coagulation. To achieve this objective, we planned to use capillary electrophoresis to separate polyP. The reasons why we decided to use this instrument were based on the feasibility of this technology to separate charged polymers (including polyP with high resolution^{13,15,16}) and the capability of this separation to be incorporated to the microrings (research in progress in our lab). Compared to previous analysis of polyP using CE, we aimed to separate longer molecules and so the separation parameters and

strategies would differ to the ones already utilized. The suggested strategies are shown in **Figure 6-1**, and described in the following paragraphs:

- (1) Separating the polyP fragments by capillary gel electrophoresis using indirect UV detection (**Figure 6-1A**). Following the work of Lee and Whitesides, capillaries are filled with a sieving matrix and polyP is detected by indirect detection a UV chromophore, terephthalate or pyromellitic acid, PMA. When detecting long polyP molecules, a sieving matrix is needed to have resolution of the peaks. The sieving matrix will cause the longer peaks to migrate slower than the smaller ones. The anionic chromophore is added to the running buffer generating a baseline in the electropherogram. When the sample zones containing PolyP migrate through the detection window, they can be observed by a decrease in UV absorbance.
- (2) Using affinity capillary electrophoresis in free solution to observe the differential mobility of a polyP binding domain (PPXbd) when bound to different size polyP molecules. When the domains are bound to the different size polymers, they will undergo a change in electrophoretic mobility. In this occasion, the sieving matrix is not needed because the PPXbd+PolyP conjugate will have different size and shape with different length polymers. Also, because we are using these peptide molecules, we can detect them by UV absorbance at 280 nm. These experiments can be carried out with fused silica capillaries and move the complexes with the electroosmotic flow, EOF (**top Figure 6-1B**). However, because of protein adsorption to the walls of the capillary, EOF can give low reproducibility. Other option will be to use coated capillaries to suppress EOF and protein adsorption and move the conjugates with electrophoretic flow (**bottom Figure 6-1B**).

4.2. Experimental methodology

Materials

Polyphosphate preparations of different mean polymer lengths and the PPXbd were donated from Dr. Jim Morrissey group. Buffer components for capillary electrophoresis were purchased from MilliporeSigma (Burlington, MA) and ThermoFisher (Waltham, MA). UltraTrol LN was purchased from (Target Discovery, Palo Alto, CA). PVA coated capillaries were purchased from Agilent (Santa Clara, CA).

Capillary electrophoresis

The instrument used was a Beckman Coulter P/ACE MDQ Capillary Electrophoresis system. The capillary gel electrophoresis separations were carried out in fused silica capillaries with 360 μm outer diameter and 50 μm inner diameter. The total length of the capillary was 30 cm and 10 cm to the detection window. The free solution separations were carried out in PVA-coated capillaries with 360 μm outer diameter and 50 μm inner diameter. The total length of both types of capillaries was 30 cm, and 10 cm to the detection window. The detection system was UV absorption at 260 nm or 280 nm and a laser-induced fluorescence (LIF) detection system with excitation at 488 nm and emission at 520 nm. The electropherograms were obtained with 32 Karat software and analyzed with Origin® 2017 (OriginLab Corporation).

For the gel electrophoresis separations of the DNA ladder and polyP fragments the capillary was conditioned with 1M sodium hydroxide, water, and UltraTrol LN (EOF suppressor) (Target Discovery; Palo Alto, CA) for 3 min each following by the dextran sieving matrix (25-75 mM Tris pH 8.5, 7-20% w/v 1.5-2.8 MDa dextran, 10% w/v glycerol) at 40 psi for 10 min. Samples were injected electrokinetically at 10kV for 5s and electrophoresed at 333 V/cm. The capillaries were regenerated and reconditioned for repeated runs to avoid shifts in migration.

For the free solution electrophoresis separations of the polyP and the PPXbd, the capillary was rinsed with 1M sodium hydroxide, ultrapure water and then rinsed with the separation buffer (25 mM Tris-Cl/250 mM glycine pH 8.5 and 30 mg/ml polyethylene glycol) at 40 psi for 5 min. Samples were injected by pressure at 2 psi for 5s and electrophoresed at 166 V/cm. After each run, the capillary was rinsed with water and NaOH by pressure at 40 psi for 10 min.

Polyacrylamide gel electrophoresis

The narrowly dispersed polyP fragments were resolved by PAGE using 5% Polyacrylamide TBE gels from Bio-Rad (Hercules, CA) with 1X TBE as running buffer. 15 μL of 500 μM polyP samples (in monophosphate units) were mixed with 2.5 μL of Gel Loading Dye, Purple (6X), no SDS (New England Biolabs, Inc) and loaded into the lanes. Electrophoresis was performed at 150V for 20 min. Gels were stained with 0.05% toluidine blue in 25% methanol/5% glycerol and rinsed in 25% methanol/5% glycerol for 2 h.

The combination of polyP and PPXbd were mixed in a ratio of 1 μ g protein:100 μ M polyP. They were conjugated at room temperature for 15 min. These conjugates were resolved by PAGE using 4-20% Mini-Protean TGX Precast Gels from Bio-Rad (Hercules, CA) with Tris-Glycine as running buffer. 15 μ L of the sample was mixed with 15 μ L of Native Sample Buffer from Bio-Rad (Hercules, CA) and loaded into the lanes. Electrophoresis was performed at 150 V for 45 min. Gels were stained with Bio-Safe™ Coomassie Stain from Bio-Rad (Hercules, CA) for 1h and rinsed in miliQ water for 1h.

4.3. Results

Capillary gel electrophoresis combined with indirect UV detection

A previous study by Smith et al. has proven that DNA ladders can be used to size polyphosphate in polyacrylamide electrophoresis¹⁷. The first strategy was to replicate this study, instead using capillary gel electrophoresis to see if the DNA ladder could also be employed to estimate polyP polymer lengths. Based on literature and previous experience in the Kennedy lab¹⁸, we decided to use a dextran sieving matrix to separate the fragments. Dextran has been characterized for having low viscosity and can be easily replaceable after each run by rinsing with water. It also has poor UV absorbance, and therefore it was suitable for our direct and indirect UV absorption detection¹⁹.

The initial step was the generation of a sieving matrix that gave us enough resolution to separate a Φ X174 DNA-Hae III Digest (New England, Biolabs Inc.). For the separation of the DNA ladder, the best results were obtained with capillaries filled with solutions of 10% w/v dextran, 12% sorbitol w/v or higher in running buffer 25 mM Tris pH 8.5. In each run, we preconditioned the capillary with sodium hydroxide and UltraTrol (EOF suppressor), and then we filled them with the sieving matrix by positive pressure (40 psi for 10 min). The trace in **Figure 6-2A** illustrates the separation of the 50 μ g/ml Φ X174 DNA-Hae III Digest (NEB) at three different voltages. The detection of the peaks was done by direct UV absorption at 260 nm. The peaks were identified by comparing to the bands in gel agarose electrophoresis. By plotting the $1/R_f$ versus log 10 of DNA bp we could fit the points to linear regression at different voltages. (**Figure 6-2B**). The idea will be then to obtain the migration times, R_f , for the polyP fragments and use the regression lines made for the DNA standards to characterize the size of polyP.

For the next step, we had to measure the migration time of different size polyP fragments. We used four different polyP fragments previously characterized¹⁷ that can be visualized in **Figure 6-3**. Contrary to DNA detection, we needed to incorporate UV indirect detection because polyP does not have UV absorbance or fluorescence properties^{13,14}. For the detection of phosphates and condensed phosphates, the main electrolytes for indirect photometric detection have been phthalates, ATP and other ribonucleotides and pyromellitic acid (PMA)²⁰. For all the experiments, we preconditioned the capillary as we did for the separation of the DNA ladder with NaOH and UltraTrol and then, introduced the dextran sieving matrix. However, on this occasion, we added the electrolyte for indirect UV detection: 3 mM terephthalate¹³ or 5 mM PMA¹⁵.

Preliminary results with terephthalate as UV background electrolyte are shown in **Figure 6-4**. It is seen that there is only one peak in the electropherogram when the sieving matrix is 10% (**Figure 6-4A**). The poorer resolution might be attributed to the low amount of entangled polymer. Then, we decided to increase the concentration of dextran to see if we observed more negative absorbance peaks for the fragments. **Figure 6-4B** illustrated the electropherogram when the sieving matrix was increased to 15% dextran. In this occasion, we were able to observe more than one negative peak when the four fragments were mixed to a final concentration of 250 μM . For comparison, we also performed separations without injection to observe the electropherogram with the terephthalate electrolyte (**Green trace-Figure 6-4B**) and 250 μM of the largest fragment (mode 1100) to determine which one was the peak for the largest fragment.

Parallel to the investigations using terephthalate as indirect UV detection electrolyte; we also carried out separations using PMA. Similarly to the previous results, only one peak was observed when the sieving matrix was 10% w/v dextran (**Green trace-Figure 6-5A**). Therefore, we also increased the concentration of the dextran up to 15-20% for better resolution. In **Figure 6-5B**, four significant dips of the intensity can be observed. Also, these peaks change to longer migration times when more sieving matrix concentration is used. Therefore, it might indicate that 15-20% w/v might provide enough sieving effect to resolve long polyP chains. From the electropherogram in **Figure 6-5B**, it was determined that the best resolution was given by the 20% w/v dextran in 50 mM Tris. Then, we opted to resolve each peak separately (**Figure 6-6**), but the results were inconclusive because the baseline given by the electrolyte was irreproducible. In consequence, it was hard to identify the negative peaks. Future experiments that would help us

identify the peaks will consist of the separation of polyP standards labeled with a fluorophore. By using fluorescently labeled fragments, we will be able to correlate the positive fluorescence intensity peaks to the negative absorbance dips in UV, and then use this information to estimate the size in unknown samples.

The conclusion from this section is that 10% w/v dextran matrix was enough to resolve the DNA ladder, but no sieving effect was observed in the separation of polyP. Therefore, we had to increase the concentration of dextran up to 15% w/v in order to observe more than one dip in the intensity. These results imply that the DNA ladder comparison used in PAGE electrophoresis by Smith et al. is not adequate in capillary gel electrophoresis to identify polyP size. However, we can still use characterized polyP standards to determine the mobility of unknown fragments in optimized matrices and create correlations that enable us to determine the size of polyP polymers. Some of the limitations in this strategy are due to the irreproducibility of the baseline given by the background electrolyte. Future experiments to resolve this problem will consist in the use of fluorescence labeled fragments to optimize the separation conditions and identify the peaks using Laser Induced Fluorescence (LIF) detection.

Capillary affinity electrophoresis using a PolyPhosphate binding domain

A previous study by Saito et al. employed the polyphosphate binding domain of *Escherichia Coli* Exopolyphosphatase, PPXbd, to visualize polyP localization in standard gel electrophoresis and *Saccharomyces cerevisiae* cultures²¹. The second strategy to characterize polyP size consisted of using the affinity and UV absorbance of a PPXbd (proteins absorb at 280 nm) as a means to visualize the polymer. We hypothesized that the binding of the polyP molecules to the PPXbd would change the mobility of the protein, and the migration time would increase when longer molecules are bound. Some advantages compared to the previous strategy are that direct absorbance detection is more sensitive than indirect detection and the identification of the peaks will be more straightforward.

To test this hypothesis, we ran a native polyacrylamide slab gel (**Figure 6-6**). From this gel, we could deduce two things: 1) the electrical field did not disrupt the interaction of the PPXbd with the polyP; 2) the mobility of the protein slowed down when longer polymer sizes were present.

The fact that the separation in a slab gel was possible meant that it could be translated to capillary electrophoresis. From previous experiments (data not shown), we realized that capillary gel electrophoresis was very complicated when resolving native proteins because of their size and not enough charges to move by the electrophoretic flow. For that reason, it was determined that free solution capillary electrophoresis would be a better option.

The first experiments were done in a fused silica capillary preconditioned with NaOH and rinsed with 25 mM Tris-Gly pH 8.3 running buffer containing 30 mg/ml Polyethylene glycol (PEG) to avoid protein adsorption to the capillary. With this capillary pre-conditioning, the electroosmotic flow (EOF) produced by the charged capillary walls will be the main force in the migration of the protein+polyP conjugates (**top Figure 6-1B**). These results (**Figure 6-8**) seemed promising, the longer polyP+PPXbd eluted later compared to the shorter polyP+PPXbd conjugate and the PPXbd alone. However, these results were not very reproducible, possibly because inconsistencies of the EOF or some protein adsorption to the walls. Future experiments will be carried out using a Polyvinyl alcohol (PVA)-coated capillary to circumvent this problem. This coating would also suppress the EOF, and thus, the conjugates will be only move by electrophoretic flow (**Bottom Figure 6-1B**). In case we are not able to resolve the peaks, an alternative will be to introduce a low amount of dextran or other polymers in order to create some sieving effect without constraining the mobility of the conjugates too much.

4.4. Conclusions

Polyphosphate size characterization is fundamental to understand how the length of the polymer exert different biological roles; for example, bacterial polyP containing thousands of phosphates can be more procoagulant than small polyP coming from platelets. Separation of polyP using analytical instrumentation such as capillary electrophoresis and ion chromatography has been realized; however, the polyP size resolution did not go past fifty phosphate units. The techniques to separate longer polyP molecules higher than hundreds of phosphates are still based in slab gel electrophoresis, requiring many steps and lengthy staining procedures. In this section, we have shown the preliminary results of two strategies based on capillary electrophoresis to separate large polyP polymers. The results are promising and show that the separation of long molecules can be made using both strategies. Future directions in this project will move towards

the hyphenation of capillary electrophoresis with microring resonator and use this combination in the separation and sensitive quantitation of polyP.

FIGURES

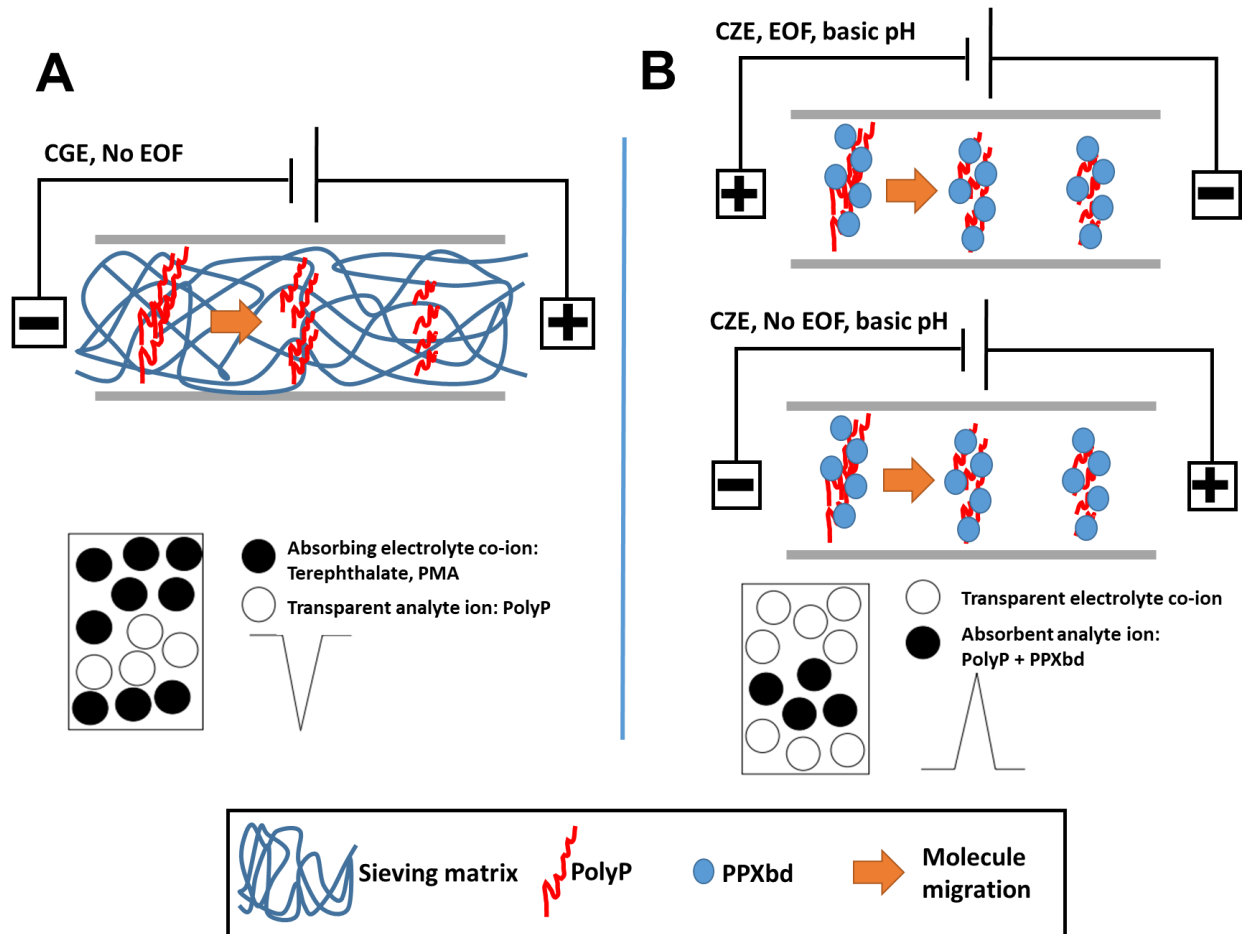


Figure 6-1. CE strategies to resolve polyP size. (A) Approach using a sieving matrix and indirect UV detection to resolve polyP. (B) Approach in free solution using a PPXbd as a probe with and without EOF as migration force.

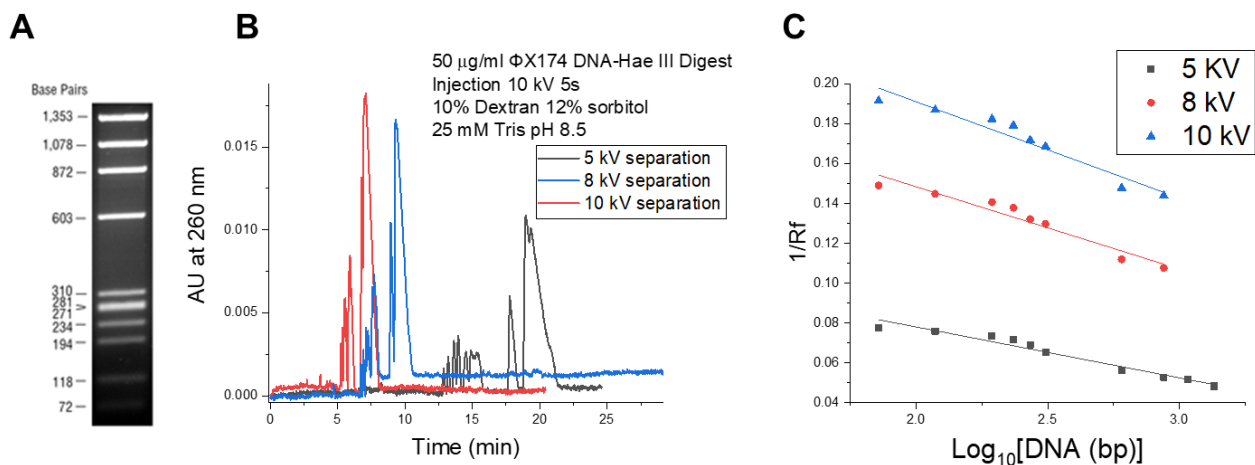


Figure 6-2. (A) ϕX174 DNA-HaeIII Digest visualized by ethidium bromide staining. 1.7% agarose gel (B) Electropherogram of 100 bp DNA ladder (C) Relationship between DNA length and migration time on 10% dextran 12% sorbitol Tris 25 mM pH 8.4 CGE.

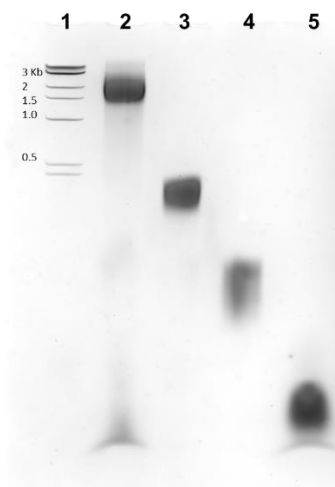


Figure 6-3. Size-fractionated PolyP preparations resolved on 5% polyacrylamide gels. Lane 2: 61-104 Pi; Lane 3: 217-459 Pi; Lane 4: 570-852 Pi and Lane 5: 970-1370 Pi.

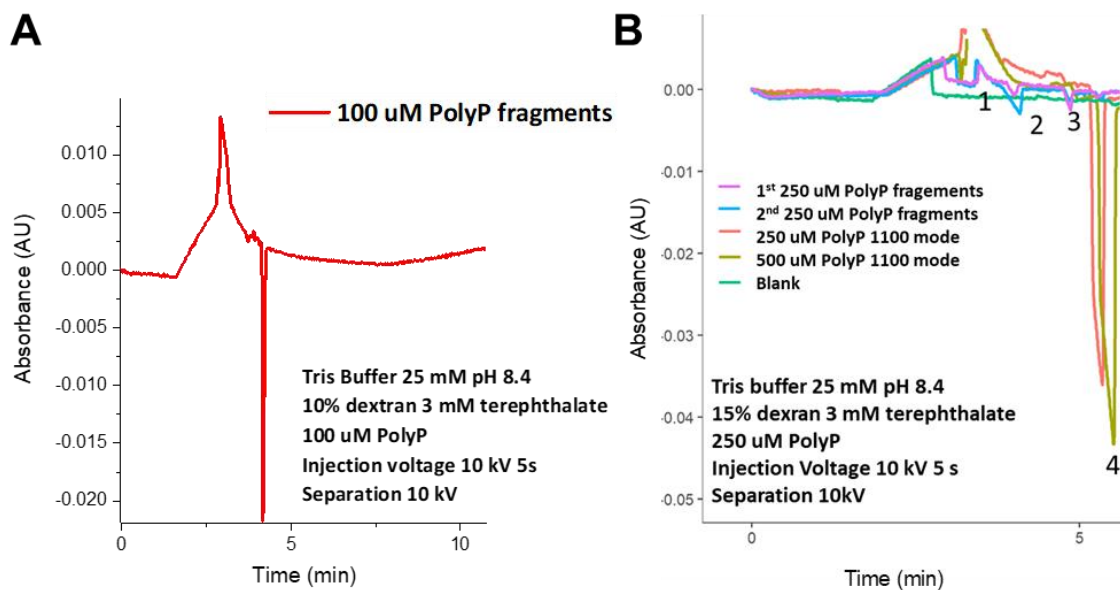


Figure 6-4. Electropherograms for polyP fragments (mode 76, mode 353, mode 708 and mode 1100). (A) 100 μ M polyP fragment mixture separated using a 10% dextran matrix. (B) 250 μ M polyP fragments separated in 15% dextran matrix.

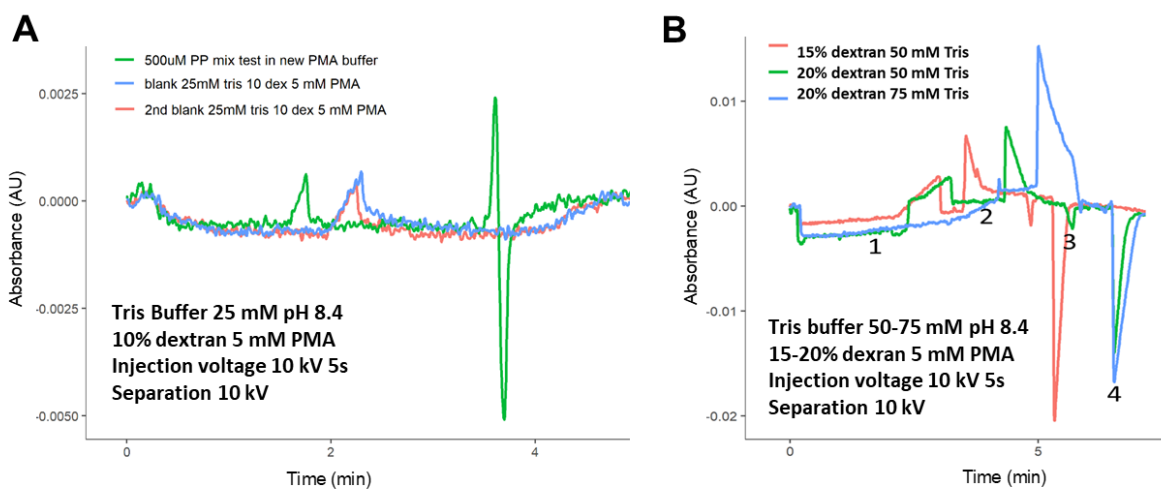


Figure 6-5. Electropherograms for polyP fragments (mode 76, mode 353, mode 708 and mode 1100). (A) Blanks and 500 μ M polyP fragment mixture separated using a 10% w/v dextran in 25 mM Tris 5 mM PMA. (B) 250 μ M polyP fragments separated in 15-20% dextran matrix in Tris 50-75 mM Tris and 5 mM PMA.

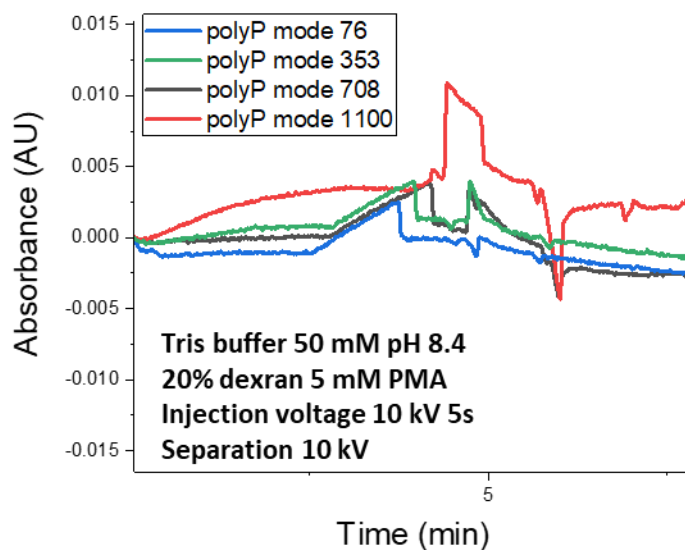


Figure 6-6. Electropherograms for 250 μM polyP fragments (mode 76, mode 353, mode 708 and mode 1100) using a 20% w/v dextran matrix and 5 mM PMA in 50 mM Tris buffer.

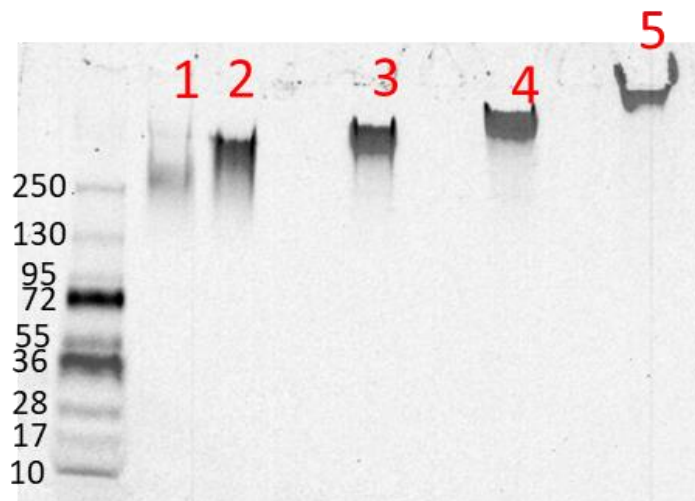


Figure 6-7. PAGE analysis of lane 1: 1 $\mu\text{g/ml}$ PPXbd; lane 2: 1 $\mu\text{g/ml}$ PPXbd conjugated with 100 μM PolyP mode 76; lane 3: 1 $\mu\text{g/ml}$ PPXbd conjugated with 100 μM PolyP mode 353; lane 4: 1 $\mu\text{g/ml}$ PPXbd conjugated with 100 μM PolyP mode 708; lane 5: 1 $\mu\text{g/ml}$ PPXbd conjugated with 100 μM PolyP mode 1100.

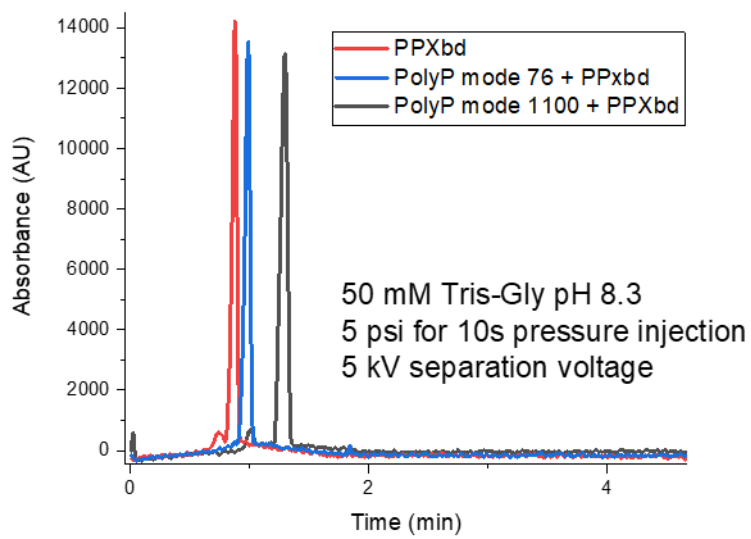


Figure 6-8. Free solution electropherograms for 20 $\mu\text{g/ml}$ purified PPXbd, 100 μM polyP fragments + 20 $\mu\text{g/ml}$ PPXbd (mode 76 and mode 1100) using 50 mM Tris –glycine as running buffer with addition of 30 mg/ml PEG.

BIBLIOGRAPHY

- (1) Cardenosa-Rubio, M. C.; Graybill, R. M.; Bailey, R. C. Combining Asymmetric PCR-Based Enzymatic Amplification with Silicon Photonic Microring Resonators for the Detection of LncRNAs from Low Input Human RNA Samples. *Analyst* **2018**, *143* (5).
- (2) Graybill, R. M.; Cardenosa-Rubio, M. C.; Yang, H.; Johnson Cd, M. D.; Bailey, R. C. Multiplexed MicroRNA Expression Profiling by Combined Asymmetric PCR and Label-Free Detection Using Silicon Photonic Sensor Arrays. *Anal. Methods*, **2018**, *10*, 1618-1623.
- (3) Vidal, M.; Cusick, M. E.; Barabási, A.-L. Interactome Networks and Human Disease. *Cell* **2011**, *144* (6), 986–998.
- (4) Scheler, O.; Kindt, J. T.; Qavi, A. J.; Kaplinski, L.; Glynn, B.; Barry, T.; Kurg, A.; Bailey, R. C. Label-Free, Multiplexed Detection of Bacterial TmRNA Using Silicon Photonic Microring Resonators. *Biosens. Bioelectron.*, **2012**, *36*(1), 56-61.
- (5) Kindt, J. T.; Bailey, R. C. Chaperone Probes and Bead-Based Enhancement To Improve the Direct Detection of mRNA Using Silicon Photonic Sensor Arrays. *Anal. Chem.*, **2012**, *84*(18), 8067-8074.
- (6) Ahrberg, C. D.; Manz, A.; Geun Chung, B. Polymerase Chain Reaction in Microfluidic Devices. *Lab Chip*, **2016**, *16*(20), 3866-3884.
- (7) Shin, Y.; Soo, R. A.; Yoon, J.; Promoda Perera, A.; Yoon, Y. J.; Park, M. K. Rapid and Label-Free Amplification and Detection Assay for Genotyping of Cancer Biomarker. *Biosens. Bioelectron.* **2015**, *68*, 107-114.
- (8) Koo, B.; Jin, C. E.; Lee, T. Y.; Lee, J. H.; Park, M. K.; Sung, H.; Park, S. Y.; Lee, H. J.; Kim, S. M.; Kim, J. Y.; et al. An Isothermal, Label-Free, and Rapid One-Step RNA Amplification/Detection Assay for Diagnosis of Respiratory Viral Infections. *Biosens.*

Bioelectron. **2017**, *90*, 187-194. .

- (9) Morrissey, J. H.; Choi, S. H.; Smith, S. A. Polyphosphate: An Ancient Molecule That Links Platelets, Coagulation, and Inflammation. *Blood*, **2012**, *119*(25), 5972-5979.
- (10) Clark, J. E.; Wood, H. G. Preparation of Standards and Determination of Sizes of Long-Chain Polyphosphates by Gel Electrophoresis. *Anal. Biochem.* **1987**, *161* (2), 280–290.
- (11) Smith, S. A.; Morrissey, J. H. Sensitive Fluorescence Detection of Polyphosphate in Polyacrylamide Gels Using 4',6-Diamidino-2-Phenylindol. *Electrophoresis* **2007**, *28* (19), 3461–3465.
- (12) Baluyot, E. S.; Hartford, C. Comparison of Polyphosphate Analysis by Ion Chromatography and by Modified End-Group Titration. *J. Chromatogr. A* **1996**, *739* (1–2), 217–222.
- (13) Lee, A.; Whitesides, G. M. Analysis of Inorganic Polyphosphates by Capillary Gel Electrophoresis. *Anal. Chem.* **2010**, *82* (16), 6838–6846.
- (14) Wang, T.; Li, S. F. Y. Separation of Polyphosphates and Polycarboxylates by Capillary Electrophoresis in a Carrier Electrolyte Containing Adenosine 5'-Triphosphate and Cetyltrimethylammonium Bromide with Indirect UV Detection. *J. Chromatogr. A* **1996**, *723* (1), 197–205.
- (15) Wang, T.; Li, S. F. . Separation of Synthetic Inorganic Polymers of Condensed Phosphates by Capillary Gel Electrophoresis with Indirect Photometric Detection. *J. Chromatogr. A* **1998**, *802* (1), 159–165.
- (16) Kaufmann, A.; Maden, K.; Leisser, W.; Matera, M.; Gude, T. Analysis of Polyphosphates in Fish and Shrimps Tissues by Two Different Ion Chromatography Methods: Implications on False-Negative and -Positive Findings. *Food Addit. Contam.* **2005**, *22* (11), 1073–1082.
- (17) Smith, S. A.; Wang, Y.; Morrissey, J. H. DNA Ladders Can Be Used to Size Polyphosphate Resolved by Polyacrylamide Gel Electrophoresis. *Electrophoresis* **2018**, *39* (19), 2454–2459.

- (18) Ouimet, C. M.; Shao, H.; Rauch, J. N.; Dawod, M.; Nordhues, B.; Dickey, C. A.; Gestwicki, J. E.; Kennedy, R. T. Protein Cross-Linking Capillary Electrophoresis for Protein–Protein Interaction Analysis. *Anal. Chem.* **2016**, 88 (16), 8272–8278.
- (19) Chung, M.; Kim, D.; Herr, A. E. Polymer Sieving Matrices in Microanalytical Electrophoresis. *Analyst* **2014**, 139 (22), 5635–5654.
- (20) Shamsi, S. A. Indirect Detection Methods in Capillary Electrophoresis. In *Encyclopedia of Analytical Chemistry*; John Wiley & Sons, Ltd: Chichester, UK, 2006.
- (21) Saito, K.; Ohtomo, R.; Kuga-Uetake, Y.; Aono, T.; Saito, M. Direct Labeling of Polyphosphate at the Ultrastructural Level in *Saccharomyces Cerevisiae* by Using the Affinity of the Polyphosphate Binding Domain of *Escherichia Coli* Exopolyphosphatase. *Appl. Environ. Microbiol.* **2005**, 71 (10), 5692–5701.